Science Immunology | Science Translational Medicine | Science Signaling

IMMUNOLOGY

[SPECIAL EDITION]

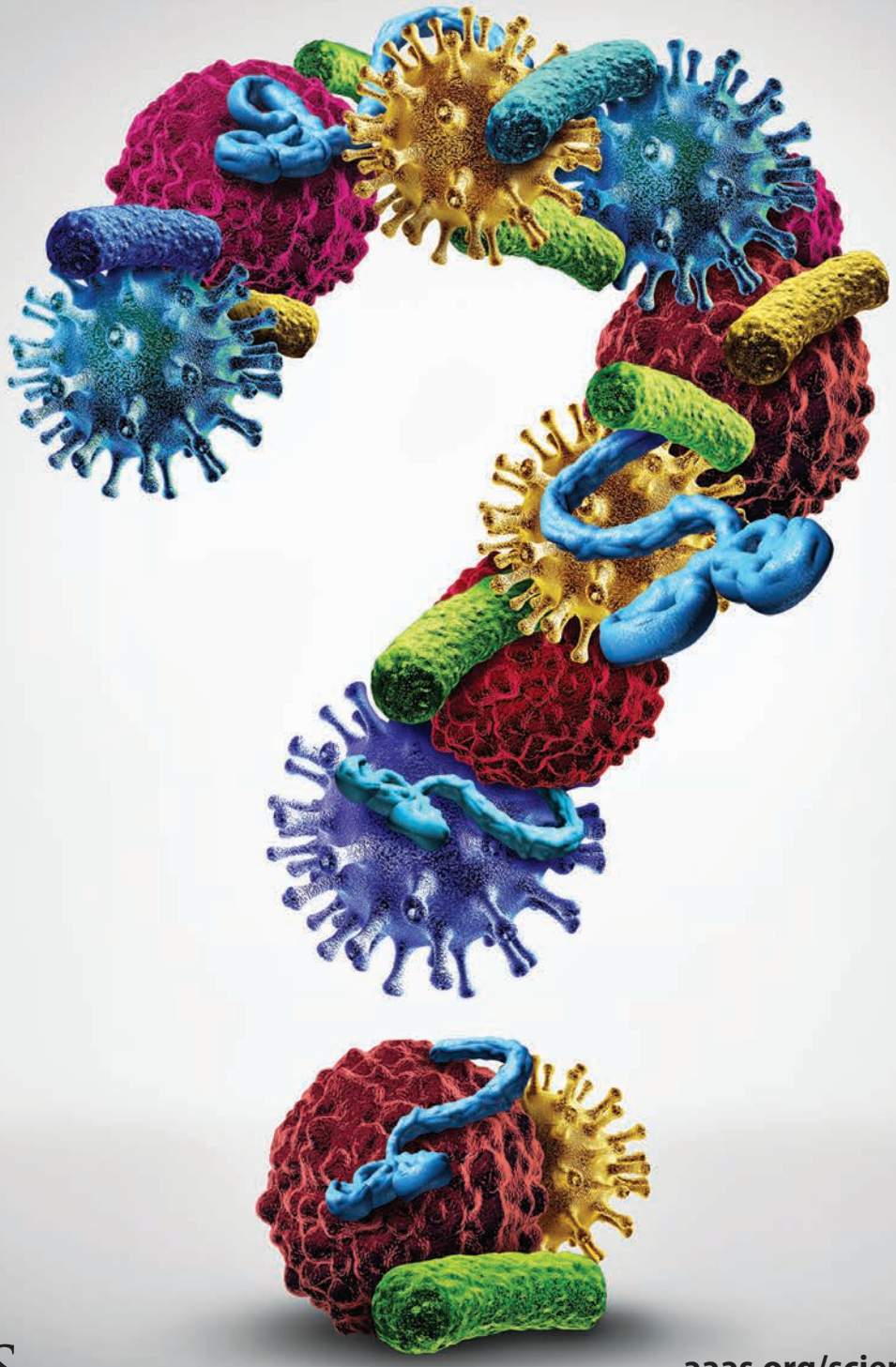

AAAS

aaas.org/science-journals

SAPPHIRE
NORTH AMERICA

WE ARE YOUR

FOR IMMUNOLOGY

THOUSANDS OF PRODUCTS

Antibodies · Immunoassays · Proteins · Small Molecules

FROM TRUSTED SUPPLIERS

AdipoGen® LIFE SCIENCES

Cayman CHEMICAL

innovative tools around dendritic cells DENDRITICS

Diaclone

EXBIO Antibodies

www.sapphire-usa.com

Mimic True Activity

MEGACD40L® Protein for Immune Response Activation

High-Activity, High-Purity Protein for Co-Stimulating Activation of an Immune Response

MEGACD40L protein is an optimized, oligomeric construct which mimics *in vivo* membrane-assisted CD40L aggregation and stimulation without the need for enhancers. Enzo's expertise in the production of challenging protein complexes, such as MEGACD40L protein, results in a product you can rely on for the duration of your study.

- Engages with immune cell receptors and acts as a potent and sustained immunostimulator
- Improved stability and enhanced activity, when compared to CD40L, alone or with enhancers
- High purity and low endotoxin to eliminate experimental artifacts
- Guarantees reliable results through consistent lot-to-lot performance
- Widely cited in peer reviewed publications

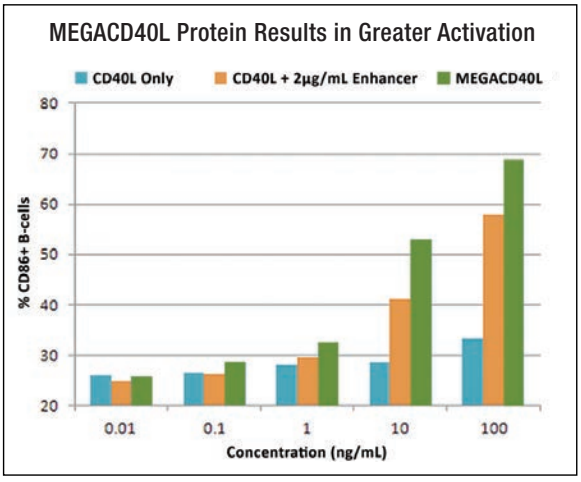

Autoimmunity | Cancer Immunotherapy | Endocrinology | Vaccine Development

SPECIAL EDITION: Immunology

Select research published in *Science Immunology*, *Science Signaling*, and *Science Translational Medicine*

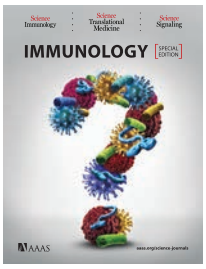

This booklet features articles from three journals in the *Science* family of journals: *Science Immunology*, *Science Signaling*, and *Science Translational Medicine*. The content covers molecular details of the signaling processes that occur in cells of both the innate and adaptive immune systems (T cells, B cells, NK cells, macrophages, dendritic cells), how inflammation is regulated, insights into pathophysiological processes and diseases associated with the immune system, and how to re-educate the immune system or modify immune function for therapeutic benefit.

Image: freshidea/AdobeStock.com

IN THIS BOOKLET

Learn more and submit your research today: aaas.org/science-journals

Science Immunology

RESEARCH ARTICLE

ASTHMA

Myosin light chains 9 and 12 are functional ligands for CD69 that regulate airway inflammation

Koji Hayashizaki,[1]* Motoko Y. Kimura,[1]* Koji Tokoyoda,[1,2]* Hiroyuki Hosokawa,[1] Kenta Shinoda,[1] Kiyoshi Hirahara,[1] Tomomi Ichikawa,[1] Atsushi Onodera,[1] Asami Hanazawa,[1,2] Chiaki Iwamura,[1] Jungo Kakuta,[3] Kenzo Muramoto,[3] Shinichiro Motohashi,[4] Damon J. Tumes,[1,5] Tomohisa Iinuma,[6] Heizaburo Yamamoto,[6] Yuzuru Ikehara,[7] Yoshitaka Okamoto,[6] Toshinori Nakayama[1,8†]

Recent decades have witnessed a rapid worldwide increase in chronic inflammatory disorders such as asthma. CD4$^+$ T helper 2 cells play critical roles in the pathogenesis of allergic airway inflammation, and CD69 expression on activated CD4 T cells is required to induce allergic inflammation in tissues. However, how CD69 mechanistically controls allergic inflammation remains poorly defined. In lymphoid tissues, CD69 regulates cellular retention through inhibition of S1P1 expression and requires no specific ligands to function. In contrast, we show herein that myosin light chain (Myl) 9 and Myl12 are new functional ligands for CD69. Blockade of CD69-Myl9/12 interaction ameliorates allergic airway inflammation in ovalbumin-induced and house dust mite–induced mouse models of asthma. Within the inflamed mouse airways, we found that the expression of Myl9/12 was increased and that platelet-derived Myl9/12 localized to the luminal surface of blood vessels and formed intravascular net-like structures. Analysis of nasal polyps of eosinophilic chronic rhinosinusitis patients revealed that Myl9/12 expression was increased in inflammatory lesions and was distributed within net-like structures in the intravascular space. In addition, we detected Myl9/12 in perivascular spaces where many CD69$^+$ cells were positioned within Myl9/12 structures. Thus, CD69-Myl9/12 interaction is a key event in the recruitment of activated CD69$^+$ T cells to inflamed tissues and could be a therapeutic target for intractable airway inflammatory diseases.

INTRODUCTION

CD69 is a type II transmembrane glycoprotein with C-type lectin domains that is expressed on activated leukocytes, especially on T cells (*1*, *2*). CD69 expression is rapidly induced upon T cell receptor (TCR) stimulation (*3*) and is therefore used as a marker for early activation of T cells. CD69 is also expressed on developing T cells undergoing selection in the thymus (*2*). Furthermore, several recent studies have shown that CD69 plays important roles in establishing tissue inflammation by promoting cell recruitment and retention in various sites (*4*–*8*). CD69 regulates cellular retention within lymphoid tissues by inhibiting S1P1 expression through direct interaction (*4*), whereas it remains unknown whether there are any specific ligands for CD69 in peripheral tissues.

We have previously reported that CD69 expression on effector CD4 T cells (*5*, *8*) and neutrophils (*6*) is crucial for the establishment of tissue inflammatory responses. For example, CD69-deficient antigen-specific CD4 T cells failed to migrate into and be retained in the lung, resulting in reduced airway inflammatory responses after antigenic airway challenge (*5*). CD69-deficient mice are resistant to dextran sulfate sodium (DSS)–induced colitis, and this is due to the inability of CD4 T cells to infiltrate the colon mucosa after DSS treatment (*8*). Furthermore, CD69-deficient CD4 T cells failed to generate memory CD4 T cells and to induce secondary antibody responses because of their inability to relocate into and persist in the bone marrow (BM), where antigen-specific resting memory CD4 T cells are maintained (*7*, *9*). These inflammatory responses were efficiently prevented by in vivo treatment with blocking anti-CD69 antibodies (*5*, *7*, *8*), suggesting that CD69 may function through specific interactions with one or more ligands expressed in inflamed sites. However, such ligands have not yet been determined.

Accumulation of CD69-expressing leukocytes was observed in a number of human chronic inflammatory disorders, such as asthma (*10*) and eosinophilic pneumonia (*11*). CD69 expression on eosinophils is induced by cytokine stimulation, including interleukin-3 (IL-3), IL-5, granulocyte-macrophage colony-stimulating factor, and interferon-γ (*10*, *11*), suggesting that cytokines in the inflammatory environment may induce CD69 expression on effector leukocytes and promote their retention within inflammatory tissues. Accumulation of effector leukocytes in tissues promotes efficient immune response but also may result in exacerbation of inflammatory disorders. The mechanism by which CD69-expressing effector leukocytes are retained at sites of inflammation remains unknown.

An example of chronic inflammatory disorders in humans is chronic rhinosinusitis (CRS), which is categorized as an upper respiratory inflammatory disorder with tissue remodeling of the sinuses and distinct cytokine production profiles by infiltrating inflammatory cells (*12*–*14*). CRS with nasal polyps often shows T helper 2 (T_H2)–type inflammation, and the nasal polyps include infiltration of large numbers of eosinophils [eosinophilic CRS (ECRS)], lymphocytes, and plasma cells (*12*, *13*, *15*–*17*). ECRS patients usually undergo surgical resection and topical or systemic administration of steroids, which improve their symptoms; however, the recurrence rate remains very high (*16*, *18*). In addition, approximately one-third of ECRS patients suffer from asthma, indicating

[1]Department of Immunology, Graduate School of Medicine, Chiba University, 1-8-1 Inohana, Chuo-ku, Chiba 260-8670, Japan. [2]Deutsches Rheuma-Forschungszentrum Berlin, Charitéplatz 1, 10117 Berlin, Germany. [3]KAN Research Institute Inc., 6-8-2 Minatojima-minamimachi, Chuo-ku, Kobe, Hyogo 650-0047, Japan. [4]Department of Medical Immunology, Graduate School of Medicine, Chiba University, Chuo-ku, Chiba 260-8670, Japan. [5]South Australian Health and Medical Research Institute, North Terrace, Adelaide SA 5000, Australia. [6]Department of Otorhinolaryngology, Graduate School of Medicine, Chiba University, Chuo-ku, Chiba 260-8670, Japan. [7]Department of Molecular and Tumor Pathology, Graduate School of Medicine, Chiba University, Chuo-ku, Chiba 260-8670, Japan. [8]Japan Agency for Medical Research and Development (AMED)–Core Research for Evolutionary Medical Science and Technology (CREST), AMED, 1-8-1 Inohana, Chuo-ku, Chiba 260-8670, Japan.
*These authors contributed equally to this work.
†Corresponding author. Email: tnakayama@faculty.chiba-u.jp

some similarities in the pathogenesis of inflammation between ECRS and asthma (*16*). Our recent study showed that infiltrating cells in nasal polyps from ECRS patients highly express CD69 (*19*), implying that CD69 expression on effector leukocytes may play roles in the pathogenesis of ECRS.

We herein identified myosin light chain (Myl) 9, Myl12a, and Myl12b (Myl9/12) as new functional ligands for CD69 in inflamed lungs. Upon airway inflammation, Myl9/12 proteins were predominantly detected on the luminal surface of blood vessels and also as net-like structures inside the vessels. Myl9/12 proteins appeared to be derived from activated platelets in the clots. Blockade of the interaction between CD69 and Myl9/12 by specific antibodies resulted in reduced leukocyte infiltration and ameliorated airway inflammation, indicating that Myl9/12 protein detected on the luminal surface of blood vessels and net-like structures in the clots may play an important role as a platform for CD69-expressing effector leukocytes to be recruited into and maintained in inflamed tissues. A similar localization of Myl9/12 was observed in the polyps of ECRS, a human chronic upper airway inflammatory disease. This study identifies a new mechanism by which effector lymphocytes are recruited and retained in inflamed tissues through CD69-Myl9/12 interaction.

RESULTS

Identification of Myl9/12 as functional ligands for CD69

To identify potential CD69 ligands, we decided to use BM cells because previous studies within our laboratory found that BM cells constitutively express CD69-interacting molecules (*7*). Affinity purification, using an anti–glutathione *S*-transferase (GST) antibody with a mixture of BM extracts and recombinant GST–His–CD69 extracellular domain (GST-His-CD69EC) protein, identified an associated 19-kDa protein (Fig. 1A, black arrowhead), which was identified as Myl9 by mass spectrometry (fig. S1A). To determine whether the Myl9 molecule interacts with CD69, we performed co-immunoprecipitation (IP) assays (fig. S1B, lanes 1 and 2) and enzyme-linked immunosorbent assays (ELISAs) (Fig. 1B) and observed a direct interaction between Myl9 and CD69EC molecules. Because the CD69 molecule is known to be highly glycosylated (*1*), we next examined the impacts of the glycosylation of CD69 on interaction with Myl9. A stronger interaction of Myl9 with CD69EC was detected when N-linked glycans were removed by *N*-glycosidase F (PNGase F) treatment (fig. S1B, lanes 3 and 4, and Fig. 1B, right).

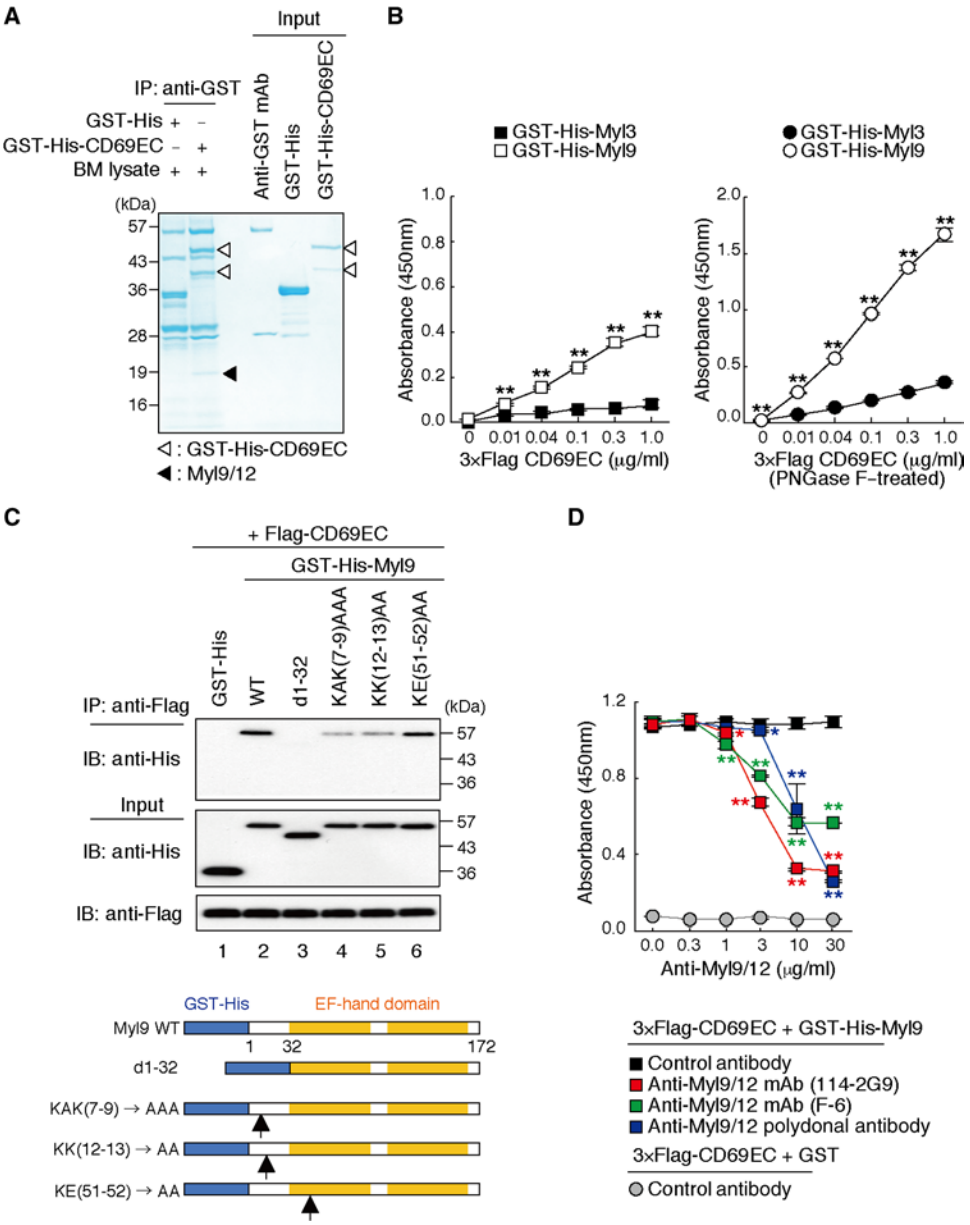

Fig. 1. Identification of Myl9/12 as interacting proteins for CD69. (**A**) BM extracts from C57BL/6 mice mixed with recombinant GST-His-CD69EC proteins were subjected to affinity purification using anti-GST antibody, followed by SDS-PAGE and Coomassie brilliant blue staining. Black arrowhead indicates CD69EC-interacting proteins (Myl9/12), and white arrowheads indicate recombinant CD69EC protein. Input was subjected to SDS-PAGE in parallel. (**B**) ELISAs were used to detect interactions between GST-His-Myl9 protein and 3×Flag CD69EC protein with or without PNGase F treatment. (Left) $^{**}P = 0.00039$, $^{**}P = 0.0000015$, $^{**}P = 0.000003$, $^{**}P = 0.0000015$, and $^{**}P = 0.000018$ (*t* test; $n = 3$). (Right) $^{**}P = 0.000001$, $^{**}P = 0.0000001$, $^{**}P = 0.0000001$, $^{**}P = 0.00000006$, and $^{**}P = 0.000004$ (*t* test; $n = 3$). (**C**) PNGase F–treated 3×Flag-CD69EC proteins were mixed with GST-His-Myl9 WT or mutant proteins. The mixture was subjected to co-IP with anti-Flag antibody, followed by IB with anti-His antibody. Input was also subjected to IB in parallel. Schematic representations of the GST-His-Myl9 WT and mutants are shown (bottom). (**D**) ELISA was used to detect interaction between PNGase F–treated 3×Flag CD69EC protein and GST-His-Myl9 in the presence of anti-Myl9/12 antibodies. Red: $^{*}P = 0.015$, $^{**}P = 0.000018$, $^{**}P = 0.000000099$, and $^{**}P = 0.00000003$ (*t* test; $n = 3$). Green: $^{**}P = 0.0015$, $^{**}P = 0.000023$, $^{**}P = 0.0000045$, and $^{**}P = 0.000000075$ (*t* test; $n = 3$). Blue: $^{*}P = 0.024$, $^{**}P = 0.0045$, and $^{**}P = 0.000000026$ (*t* test; $n = 3$). Data are representative of at least three (A, B, D) or two (C) independent experiments.

These data demonstrate that Myl9 specifically interacts with CD69 and that this interaction is partially dependent on the glycosylation status of CD69.

We next examined which regions of Myl9 protein were interacting with CD69 by co-IP assays with the recombinant Myl9 mutant proteins, and we found that positive charges at the N-terminal regions (positions 7 to 13) of Myl9 were required for sufficient interaction with CD69EC (Fig. 1C). Therefore, we generated polyclonal and monoclonal anti-Myl9 antibodies specific for the N-terminal region of Myl9 (positions 1 to 27), with the aim of specifically inhibiting the interaction between Myl9 and CD69. The Myl9 amino acid sequence has high homology to Myl12a (94%) and Myl12b (94%) (fig. S1C), and CD69EC proteins were able to interact with Myl9, Myl12a, and Myl12b proteins in vitro (fig. S1D). As we expected, both monoclonal and polyclonal antibodies bound to Myl9, Myl12a, and Myl12b (fig. S1E); therefore, we refer to these antibodies as anti-Myl9/12 antibody. Both monoclonal and polyclonal anti-Myl9/12 antibodies efficiently inhibited the interaction between Myl9 and CD69 (Fig. 1D), as did the anti-CD69 antibody (fig. S1F). Next, we performed in vitro adhesion assays with in vitro activated CD69-expressing wild-type (WT) CD4 T cells and CD69-deficient CD4 T cells (fig. S1G). WT activated CD4 T cells adhered to plate-coated Myl9 at significantly higher levels compared with CD69-deficient activated CD4 T cells, indicating that CD69 on activated CD4 T cells may functionally interact with Myl9 in vitro. These results indicate that CD69 interacts with Myl9/12 through their N-terminal regions and that the generated antibodies efficiently inhibit the interaction of CD69 with Myl9/12.

Allergic airway inflammation ameliorated by administration of anti-Myl9/12 antibody

To examine the impact of inhibiting CD69-Myl9/12 interaction on the induction and exacerbation of in vivo inflammatory responses, we injected anti-Myl9/12 antibody into mice with ovalbumin (OVA)–induced allergic airway inflammation (Fig. 2A). Injection of either monoclonal (Fig. 2) or polyclonal (fig. S2) anti-Myl9/12 antibodies 1 day before and after the first OVA inhalation significantly attenuated airway inflammation. We detected reduced lung tissue mononuclear cell infiltration and mucin secretion (Fig. 2B), reduced *Muc5ac* mRNA expression (fig. S2B), and reduced accumulation of leukocytes in bronchoalveolar lavage (BAL) fluid (Fig. 2C). In addition, T_H2-associated cytokines were undetectable in BAL fluid (Fig. 2D),

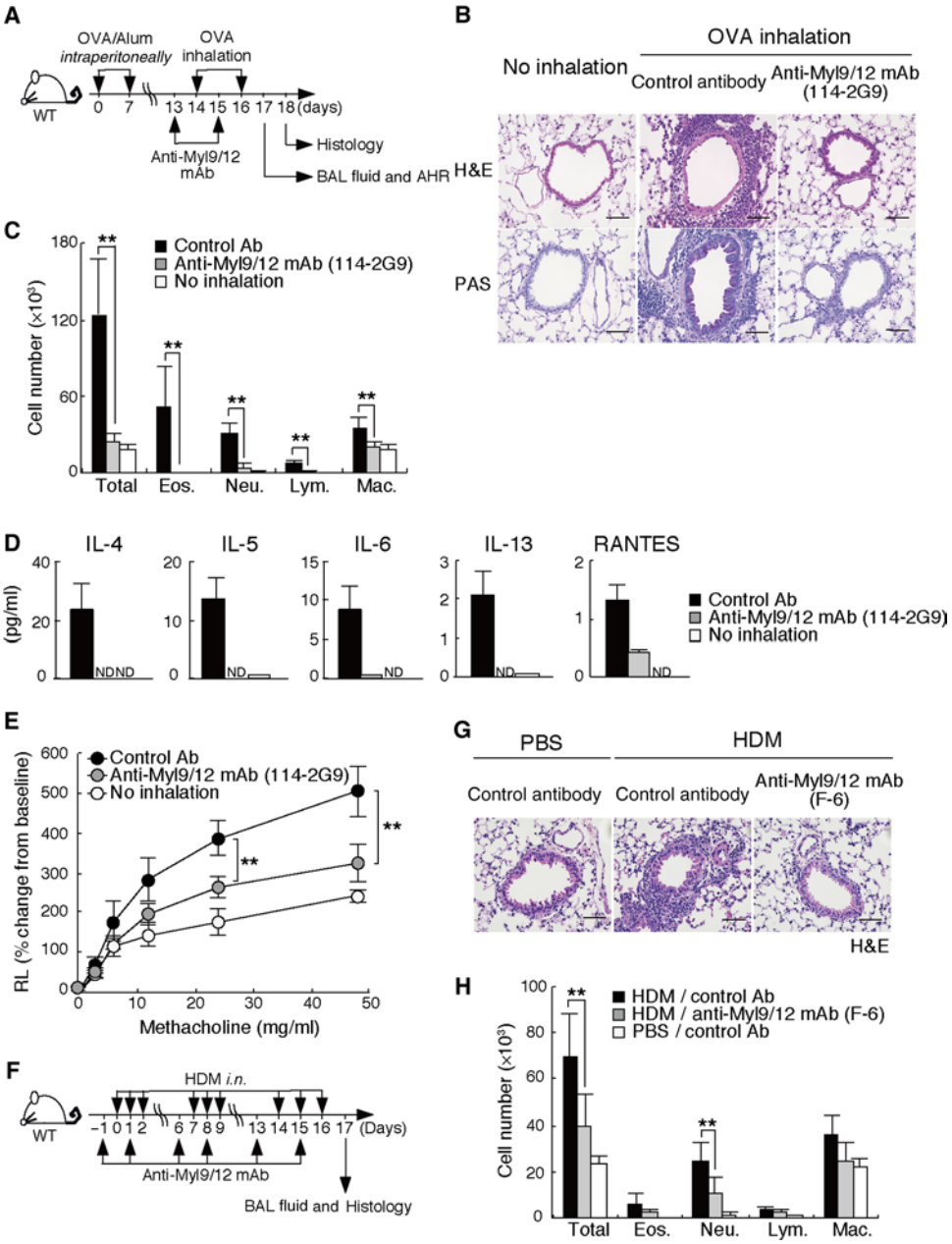

Fig. 2. Attenuation of allergic airway inflammation by administration of anti-Myl9/12 antibody. (**A**) Schematic outline of the OVA-induced allergic airway inflammation model. (**B**) Leukocyte infiltration and mucus hyperproduction in the lung, as assessed by H&E staining (top; scale bars, 50 μm) and PAS staining (bottom; scale bars, 50 μm). (**C**) Absolute numbers of eosinophils (Eos.), neutrophils (Neu.), lymphocytes (Lym.), and macrophages (Mac.) in BAL fluid shown with the SEM (***P* = 0.0009, ***P* = 0.0084, ***P* = 0.0002, ***P* = 0.0002, and ***P* = 0.003, *t* test; *n* = 5). (**D**) Cytokines in BAL fluid shown with the SEM. (**E**) Methacholine-induced AHR shown with the SEM (**P* = 0.032 and **P* = 0.043, *t* test; *n* = 5). RL, lung resistance; ND, not detected. (**F**) Schematic outline of HDM-induced airway inflammation model. i.n., intranasally. (**G**) Leukocyte infiltration in the lung, as assessed by H&E staining (scale bars, 50 μm). (**H**) Absolute numbers of eosinophils (Eos.), neutrophils (Neu.), lymphocytes (Lym.), and macrophages (Mac.) in BAL fluid shown with the SEM (***P* = 0.009 and ***P* = 0.0092, *t* test; *n* = 7). All data are representative of more than three (A to E) or two (F to H) independent experiments. At least five mice per group were analyzed.

and methacholine-induced airway hyperresponsiveness (AHR) was significantly attenuated (Fig. 2E) after anti-Myl9/12 antibody treatment. The inhibition of OVA-induced allergic airway inflammation by anti-Myl9/12 antibody treatment was observed to the same extent as that by anti-CD69 antibody treatment (fig. S2C). To further examine the impact of anti-Myl9/12 antibody treatment on airway inflammation induced by a naturally occurring allergen, we next used house dust mite (HDM) for sensitization and challenge at the mucosal surface of the airway (Fig. 2F). Anti-Myl9/12 antibody treatment significantly ameliorated HDM-induced airway inflammation (Fig. 2, G and H). These results indicate that blockade of the interaction between Myl9/12 and CD69 by anti-Myl9/12 antibody inhibits not only OVA-induced allergic airway inflammation but also HDM-induced airway inflammation.

Increased Myl9/12 expression on the luminal surface of blood vessels in the lungs during airway inflammation

To elucidate the cellular mechanisms by which Myl9/12 regulates airway inflammation, we next examined whether Myl9/12 protein expression was induced during OVA-induced allergic airway inflammation and where the protein was located in the inflamed lung. Total amounts of Myl9/12 protein in the whole lung were increased upon airway inflammation (Fig. 3A), and immunohistological analysis revealed that Myl9/12 protein was predominantly located around the luminal surface of blood vessels but not on bronchi in the inflamed lung (Fig. 3B). Blood vessels that had Myl9/12 present on more than 10% of their surface were classified as Myl9/12-positive vessels. More than 60% of blood vessels in inflamed lung tissue were Myl9/12-positive, whereas the lung from control mice (no OVA inhalation) had a limited number of Myl9/12-positive vessels (Fig. 3C). Because anti-Myl9/12 antibody treatment efficiently prevented OVA-induced airway inflammation (Fig. 2), we next used goat antirabbit immunoglobulin G (IgG) secondary antibody to detect the in vivo localization of the anti-Myl9/12 antibody that we administered to mice with allergic airway inflammation. The anti-Myl9/12 antibodies were mainly detected on the luminal surface of blood vessels (fig. S3A). These results indicate that Myl9/12 protein becomes detectable on the luminal surface of blood vessels in the lungs upon OVA-induced allergic airway inflammation.

Platelet-dependent formation of Myl9/12 net-like structures during airway inflammation

Myl9/12 are proteins typically considered to be restricted to the cytosol under normal conditions. Therefore, it was essential to determine how Myl9/12 protein was relocated to the luminal surface of blood vessels during airway inflammation. We first examined Myl9/12 expression in vascular endothelial cells. Although expression of Myl9/12 on lung endothelial cells was detected by flow cytometry, no obvious increase was detected upon inflammation (fig. S3B), and *Myl9/12* mRNA expression in sorted $CD45^{-}TER119^{-}PECAM\text{-}1^{+}$ lung endothelial cells was not changed (fig. S3C). Myl9 is known to form a complex with nonmuscle myosin IIa (Myh9) (*20*), which is highly expressed in megakaryocytes and platelets (*21*, *22*), and Myl9 can be detected in granules released from platelets upon activation (*23*). Platelets are readily activated in the intravascular space in inflamed lungs; therefore, we hypothesized that activated platelets in inflamed lungs release platelet activation mediators including Myl9, resulting in Myl9 protein attachment to the luminal surface of blood vessels. We first confirmed that Myl9/12 protein was highly expressed in megakaryocytes (Fig. 4A) and platelets (Fig. 4B). In vitro thrombin stimulation resulted in the relocation of Myl9/12 to the edge of platelets within 10 min and its disappearance from platelets in 2 hours (fig. S4A), followed by abundant My9/12 protein detected in the culture supernatant 2 hours after stimulation (Fig. 4C). We next examined mRNA expression levels of *Myl9*, *Myl12a*, and *Myl12b* in platelets and endothelial cells with specific primers. mRNA expression levels of *Myl9*, *Myl12a*, and *Myl12b* were high in platelets but very low in lung endothelial cells (Fig. 4D). *Myl9* mRNA expression in platelets was extremely high, suggesting that the major molecule detected by anti-Myl9/12 antibody in the lung is Myl9.

We further examined at which location on the luminal surface of blood vessels in inflamed lungs was Myl9/12 protein detected by immunohistological analysis. Myl9/12 protein was detected on the luminal surface of blood vessels but was not merged with platelet endothelial cell adhesion molecule–1 (PECAM-1) staining of vascular endothelial cells (Fig. 4E), indicating that Myl9/12 protein attaches to the luminal surface of blood vessels but is not expressed in vascular endothelial cells. Furthermore, with immunohistological analysis using thicker (20 μm) lung sections, we found that some of the blood vessels in the inflamed lungs contained clots (thrombus) consisting of $TER119^{+}$ red blood cells, $CD41^{+}$ platelets, and Myl9/12, forming net-like structures (Fig. 4, F and G, and movie S1). We further addressed the impact of platelet depletion on inflammation-induced Myl9/12 expression by injecting anti–glycoprotein 1b, alpha polypeptide (GP1bα) antibody (Fig. 4H), which efficiently depleted platelets in the peripheral blood (*24*) and lungs (fig. S4B). The levels of Myl9/12 protein attached to the luminal surface of blood vessels in the lungs of mice treated with anti-GPIbα antibody were reduced (Fig. 4I). The total amounts of Myl9/12 protein in the lung were also reduced (Fig. 4J). Together, we conclude that

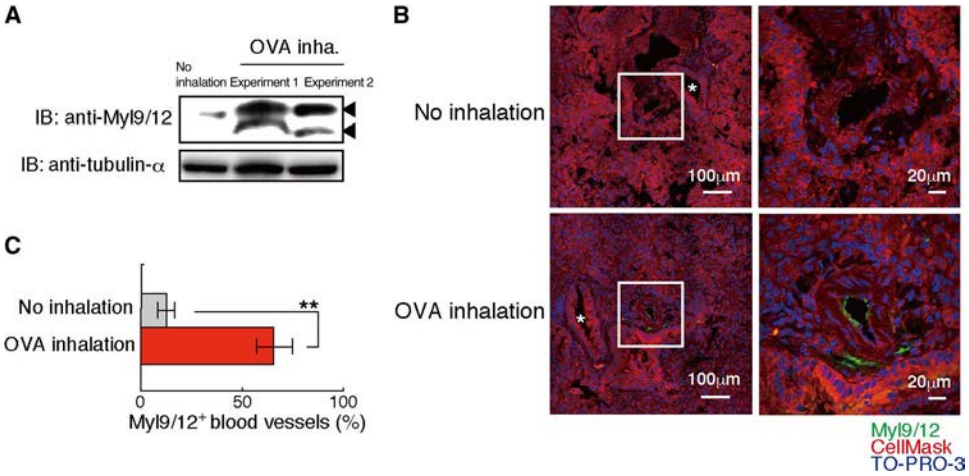

Fig. 3. Increased Myl9/12 expression on the luminal surface of blood vessels in the lungs during airway inflammation. (**A**) Myl9/12 expression in the lung with or without OVA inhalation, as detected by IB. (**B**) Immunohistological analysis of lung sections with or without OVA inhalation, stained as indicated. White square indicates blood vessels, and asterisk indicates bronchi. (**C**) Frequencies of Myl9/12-positive blood vessels in the lung (**P = 0.00074, t test; n = 3). Data are representative of at least three (A to C) independent experiments. At least three mice per group were analyzed in all experiments.

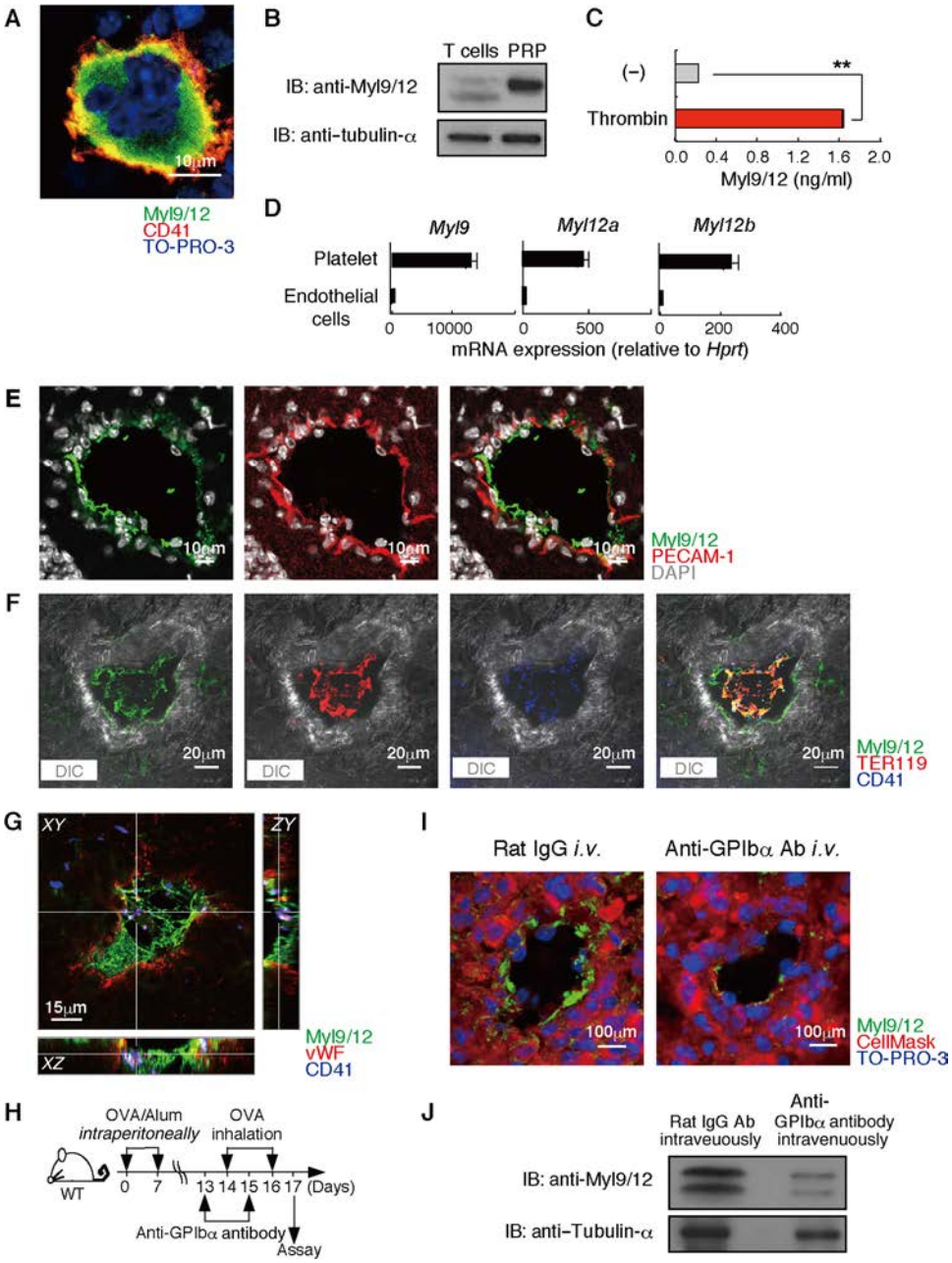

Fig. 4. Platelet-dependent formation of Myl9/12 net-like structures during airway inflammation. (**A**) Immunohistological analysis of megakaryocytes in a BM section, stained as indicated. (**B**) IB of Myl9/12 protein expression in purified PRP and splenic T cells. (**C**) ELISA to detect Myl9/12 protein in the supernatant from the culture where platelets were stimulated with or without thrombin for 2 hours in vitro (**P = 0.000068, t test; n = 3). (**D**) mRNA expression of *Myl9*, *Myl12a*, and *Myl12b* in platelets and sorted lung endothelial cells. Gene expression levels were normalized to those of *Hprt*. (**E** and **F**) Immunohistological analysis of lung sections after OVA inhalation, stained as indicated and merged with differential interference contrast (DIC) as indicated. (**G**) Three-dimensional image from immunohistological analysis using 20 μm lung sections of mice with OVA inhalation, stained as indicated. (**H**) Schematic outline of the allergic airway inflammation model with anti-GPIbα antibody treatment. (**I**) Immunohistological analysis of lung sections after OVA inhalation with anti-GPIbα antibody treatment, stained as indicated. (**J**) Myl9/12 expression in the lung after OVA inhalation with anti-GPIbα antibody treatment. Data are representative of at least three (A to F) or two (H to J) independent experiments. At least three mice per group were analyzed in all experiments.

Myl9/12 molecules are predominantly detected on the luminal surface of blood vessels, form net-like structures in the thrombus in the inflamed lungs, and are likely to be derived from platelets.

Detection of CD69$^+$ antigen-specific CD4 T cells in the lung vasculature during airway inflammation

Considering that Myl9/12 protein expression was detected mainly on the luminal surface of blood vessels (Fig. 3) and that anti-Myl9/12 and anti-CD69 antibodies significantly ameliorated airway inflammation (Fig. 2), it is likely that antigen-specific CD69-expressing T cells in the lung are recruited into tissues by interacting with Myl9/12. Consequently, using an intravascular staining method, we examined whether there were any CD69$^+$CD4 T cells in the lung vasculature during airway inflammation (*25*). We injected OVA-specific (KJ1$^+$) CD4 T cells into host mice, induced airway inflammation, and examined whether there were any CD69$^+$ KJ1$^+$CD4 T cells in the lung vasculature (fig. S5A). No detectable CD69-expressing KJ1$^+$ cells were observed in the peripheral blood, whereas about 1% of injected KJ1$^+$ cells expressed CD69 in the lung vasculature before OVA inhalation (fig. S5, B and C). The frequency of CD69-expressing KJ1$^+$ cells in the peripheral blood was not increased, whereas that in the lung vasculature increased substantially and significantly 12 and 24 hours after OVA inhalation (fig. S5, B and C). The absolute number of CD69$^+$KJ1$^+$ cells in the lung vasculature was also increased upon OVA inhalation (fig. S5C, right). Increased numbers of CD69$^+$KJ1$^+$ cells were detected in the lung parenchyma even at 12 hours after OVA inhalation (fig. S5D). This result could indicate that CD69$^+$KJ1$^+$CD4$^+$ T cells in the lung vasculature rapidly migrate into the lung parenchyma. In addition, CD69$^+$ TCRβ$^+$ T cells were detected, by immunohistochemistry, inside the blood vessels 24 hours after OVA inhalation (fig. S5E). These results indicate that antigen-specific T cells in the lung vasculature express CD69 upon airway antigen challenge and that the expression of CD69 may be important for these T cells to be recruited into the lung parenchyma.

Effects of anti-Myl9/12 and antihuman CD69 antibodies on human CD69-mediated allergic airway inflammation

To further address the feasibility of using anti-CD69 and anti-Myl9/12 antibodies for the treatment of patients, we established a mouse model of human CD69-mediated airway inflammation (fig. S6A). We generated mouse CD69-deficient OVA-specific effector T_H2 cells with or without

human CD69 expression (fig. S6B) and confirmed that human CD69-expressing T_H2 cells efficiently induced airway inflammation in BALB/c host mice. The amino acid sequences of the N-terminal regions of human Myl9/12 and murine Myl9/12 are almost identical, and human CD69 was confirmed to interact with mouse Myl9 almost as efficiently as mouse CD69 (fig. S6C). Both antihuman CD69 and anti-Myl9/12 antibodies significantly attenuated inflammatory responses (fig. S6, D and E), indicating that blockade of the interaction between human CD69 and Myl9/12 inhibits human CD69-mediated airway inflammation. CD69 expression is known to be induced on many activated leukocytes (*3*, *26*); therefore, any CD69-expressing leukocytes could interact with Myl9/12 and be targets of anti-Myl9/12 and anti-CD69 antibody treatments. However, experiments using the OVA-induced asthma model described herein show that the blockade of the interaction between Myl9/12 and CD69 on T_H2 cells was sufficient to attenuate airway inflammation. Thus, CD69 on T_H2 cells appeared to be the major target of the antibody treatment that prevents airway inflammation in this model.

Myl9/12 expression in the polyps of ECRS patients

CRS is a common allergic inflammatory disease of the upper respiratory tract (*27*, *28*), and recent reports have suggested the relationship between the pathogenesis of CRS and abnormal coagulation cascade (*29*). Therefore, we examined the expression of Myl9/12 in human chronic airway inflammatory lesions such as nasal polyps of ECRS patients (*30*, *31*). Nasal mucosa obtained from nonatopic healthy donors was included as a steady-state control tissue. Myl9/12 expression was significantly increased in nasal polyps from ECRS patients, compared to control nasal mucosa, and was primarily localized in the blood vessels (Fig. 5A). With a more detailed immunohistological analysis using thicker (20 μm) sections of the polyps, we found that the luminal surface of most blood vessels contained Myl9/12 and that some of them formed net-like structures together with von Willebrand factor (vWF) (Fig. 5B). In addition, a substantial proportion of the CD69-expressing cells appeared to directly interact with the Myl9/12 protein attached on the surface of blood vessels in ECRS polyps (Fig. 5C). About 65% (64.3 ± 5.4%) of the CD3-expressing cells that were in contact with Myl9/12-positive blood vessels were CD69-expressing T cells (fig. S7, A and B). Furthermore, Myl9/12 was also distributed on the vascular walls and in perivascular spaces where many CD69-expressing cells appeared to be entangled in Myl9/12 molecules (Fig. 5D). These results demonstrate that Myl9/12 expression is significantly increased and is distributed not only in the intravascular space but also on the vascular walls and in the perivascular stromal tissue of the nasal polyps of ECRS patients. Colocalization of CD69-expressing cells and Myl9/12 protein may suggest that CD69-Myl9/12 interaction contributes to the long-term feature of inflammation in ECRS polyps.

DISCUSSION

We herein identify a previously unknown mechanism that regulates airway inflammation. We show that Myl9/12 proteins are previously unknown functional ligands for CD69 and define CD69-Myl9/12 interaction as a key step in the pathogenesis of airway inflammation.

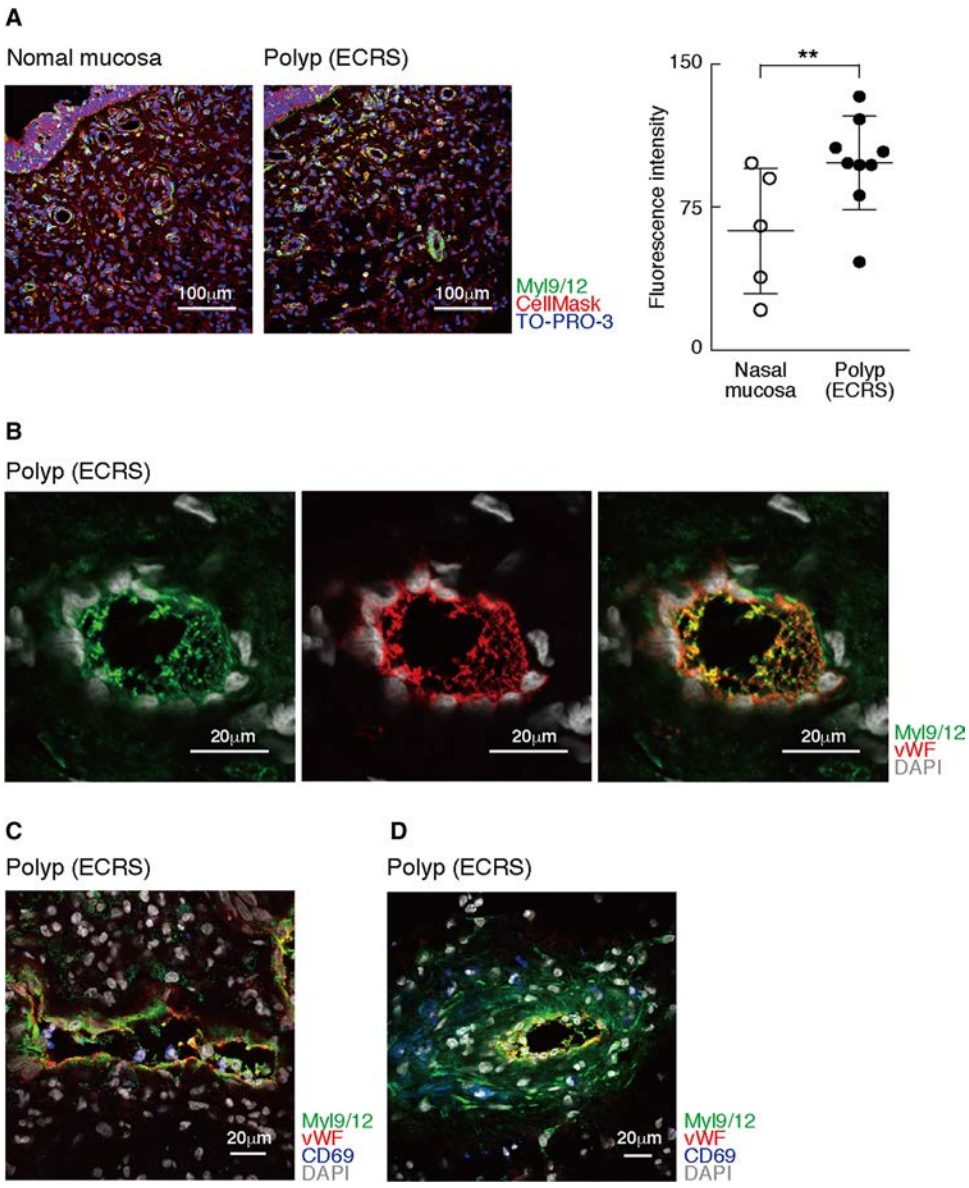

Fig. 5. Myl9/12 expression on polyps from human ECRS patients. (**A**) Immunohistological analysis of polyps from patients with ECRS (right) and noninflamed nasal mucosa as controls (left), stained as indicated. Fluorescence intensity of Myl9/12 staining is shown (right). Five normal mucosae and nine polyps from ECRS patients were analyzed (**P = 0.000039, t test; n = 5 and n = 9). (**B** to **D**) Immunohistological analysis of polyps from ECRS patients, stained as indicated. At least four polyps from ECRS patients were analyzed.

Within inflamed lungs, Myl9/12 attach to the luminal surface of blood vessels and form net-like structures inside the vessels. Blockade of the interaction between Myl9/12 and CD69 by specific antibodies ameliorates lung inflammation, suggesting that the Myl9/12 protein accumulated in inflammatory vessels may play an important role as a platform for the recruitment of CD69-expressing leukocytes into inflammatory tissues.

Leukocyte recruitment into inflammatory tissues is the first step of immune response (*32*, *33*). Innate immune cells, such as monocytes, neutrophils, and eosinophils, are recruited into inflammatory tissues through inflammatory vessels (where they are activated), whereas antigen-specific T cells are thought to be activated in draining lymph nodes and then recruited into inflammatory tissues (*34*). Previous studies have reported that migration of activated leukocytes into inflammatory sites is mediated by inflammatory chemokines and that recruitment of the cells into inflammatory tissues is mediated by the interaction of PSGL-1 (P-selectin glycoprotein ligand–1) with P-selectin (*35*, *36*). Here, we propose a new mechanism, named the "CD69-Myl9/12 system," that directs the recruitment of activated T cells into inflammatory tissues. In the CD69-Myl9/12 system, Myl9/12-containing net-like structures are created in inflammatory vessels, which play an important role as a platform for the recruitment of CD69-expressing leukocytes into inflammatory tissues. T cells that are activated in the lymph nodes proliferate, down-regulate CD69 expression, and then leave the lymph nodes to migrate into inflammatory sites in an S1pr1-dependent manner (*37*). However, our study revealed that about 10% of antigen-specific CD4 T cells in the lung vasculature express CD69 upon airway antigen stimulation (OVA inhalation). This supports the idea that the CD69-Myl9/12 system is important for the migration and recruitment of $CD69^+$ T cells into the inflamed lung. However, it is not known how CD69 expression is induced on antigen-specific CD4 T cells in the lung vasculature after antigen challenge via the airway. One possibility is that the Myl9/12 net-like structures may include antigen-presenting cells that directly instruct antigen-specific CD4 T cells to express CD69 on their surface. Another possibility is that the cytokine-rich inflammatory environment, induced after antigen challenge via the airway, activates CD4 T cells to express CD69. Various cytokines, including those that can stimulate T cells [such as IL-1β, IL-2, IL-4, IL-6, IL-9, IL-25, IL-33, and thymic stromal lymphopoietin (TSLP)], were detected in the lungs of allergic asthma models and in human patients (*38*–*41*). Further detailed analyses are required to answer this question.

Recent studies have reported a crucial relationship between abnormal coagulation and allergic airway inflammatory diseases such as asthma (*42*). Platelet abnormalities in patients with allergy have been particularly noticed (*43*, *44*). Although there is accumulating evidence of the importance of platelets in airway inflammation (*42*), how platelets are involved in the process of airway inflammation appears to be complex and not well defined. The CD69-Myl9/12 system that we herein identified may be a reason why coagulation abnormalities are often associated with allergic airway inflammation. Further studies are required to clarify the nature of the stimuli required for the extracellular deposition of Myl9/12 protein and the molecules involved in the generation of the Myl9/12 nets.

Several humanized antibodies are now undergoing trials for the treatment of asthma patients, and some encouraging results have been obtained (*45*–*48*). We reported that anti-CD69 antibody could be a possible candidate for antibody-based immunotherapy in asthma (*5*) and colitis (*8*). In the current study, we found that anti-Myl9/12 antibodies inhibited allergic airway inflammation as efficiently as anti-human and antimouse CD69 antibodies did, and the expression of Myl9/12 was selectively detected in inflamed vessels. Therefore, Myl9/12 could be a new therapeutic target for chronic airway inflammatory disorders for which effective treatments have not been established.

In conclusion, the present study identifies Myl9/12 as previously unknown functional ligands for CD69 that regulate airway inflammation and proposes a mechanism called the CD69-Myl9/12 system, which is necessary for the recruitment of antigen-specific CD69-expressing CD4 T cells into inflammatory tissues because it interacts with Myl9/12 protein in net-like structures within the blood vessels. Because Myl9/12 are derived from activated platelets that play an essential role in the blood coagulation system (*49*), the CD69-Myl9/12 system may also play a critical role in a range of other inflammatory diseases where tissue damage and blood coagulation occur. Thus, blocking the interaction between Myl9/12 and CD69 could be a new therapeutic target not only for airway inflammatory disorders but also for other inflammatory diseases.

MATERIALS AND METHODS

Study design

To elucidate the mechanism that CD69 expression on activated leukocytes contributes to inflammation, we first identified CD69 ligands by IP with recombinant CD69 protein, followed by mass spectrometry analysis, and then made specific functional antibodies against the identified CD69 ligands (anti-Myl9/12 antibodies). Using the specific antibodies, we (i) assessed the impacts of the administration of anti-Myl9/12 antibodies on airway inflammation in a mouse model and (ii) identified where and how Myl9/12 are located on blood vessels in inflamed tissues, including human polyps from ECRS patients. Differential counts of inflammatory cells in BAL fluid (Fig. 2, C and H) and Myl9/12-positive–expressing vessels (Fig. 3C) were performed double-blinded by at least two independent researchers. Statistical significance was determined as $P < 0.05$ by two-tailed t test for all experiments.

Mice

C57BL/6 and BALB/c mice were purchased from CLEA Co. (Tokyo, Japan). CD69-deficient mice were created in our laboratory (*6*) and were backcrossed onto both C57BL/6 and BALB/c genetic backgrounds more than 15 times. All mice, including OVA-specific αβTCR transgenic (DO11.10) mice (*50*), were maintained under specific pathogen-free conditions and were used at 6 to 16 weeks of age. All animal experiments were approved by the Chiba University Review Board for Animal Care.

Purification of recombinant proteins

Recombinant GST-His-CD69EC, GST-His-Myl9, Myl9 mutants, Myl12a, Myl12b, and Myl3 proteins were expressed in the BL21 (DE3) or Rosetta (DE3) strains (Novagen) transformed with pET42b-based constructs and induced by isopropyl-D-thiogalactopyranoside (1 mM) for 4 hours. GST-His-CD69EC protein was further processed for purification and refolding as previously described (*51*). GST-His-Myl9, Myl9 mutants, Myl12a, Myl12b, and Myl3 proteins were solubilized in a suspension buffer [50 mM tris-HCl (pH 8.0), 300 mM NaCl, and 10 mM imidazole] and further lysed by sonication with a Misonix sonicator (Microson). The recombinant proteins were purified with Ni-NTA Agarose (Qiagen) according to the manufacturer's protocol. Recombinant 3×Flag-CD69EC proteins were expressed in FreeStyle 293-F cells transfected with p3×Flag-CMV9-mCD69EC plasmid, and the proteins were purified using an anti-Flag M2 affinity column (A2220; Sigma). After elution with 0.1 M

glycine-HCl (pH 3.5), purified proteins were concentrated and the buffer was exchanged for phosphate-buffered saline (PBS) with Amicon Ultra-4 (Merck Millipore). Protein purity was defined by SDS–polyacrylamide gel electrophoresis (PAGE), followed by staining with SimplyBlue SafeStain (Invitrogen).

Identification of CD69-interacting proteins

Adult femurs and tibias were lysed with the following protease inhibitor–containing lysis buffer [50 mM tris-HCl (pH 8.0), 150 mM NaCl, 10% glycerol, 0.05% NaN_3, 1% Triton X-100, 1 mM phenylmethylsulfonyl fluoride, and Protease Inhibitor Cocktail (Roche)]. The cell lysates were subjected to a preclearing process with Protein G Sepharose (GE Healthcare) at 4°C for 1 hour and then mixed with GST-His-CD69EC or GST-His (10 μg each) overnight at 4°C. The mixtures were subjected to IP with an anti-GST antibody (013-21851; Wako) at 4°C for 3 hours, and then the immunocomplexes were precipitated with Protein G Sepharose beads at 4°C for 1 hour. Immunoprecipitates were washed with lysis buffer and eluted from the beads by SDS-containing gel loading buffer. The eluted samples were separated in 15% polyacrylamide gels (ATTO), and the specific band was identified by liquid chromatography–tandem mass spectrometry analysis.

Generation of antibodies against Myl9/12

To generate rabbit polyclonal antibody against Myl9/12, we used as an immunogen a fusion protein of N-terminal peptides of Myl9 (residues 1 to 27) and keyhole limpet hemocyanin. Serum was further purified by an affinity column with N-terminal peptides of Myl9 that was originally used as an immunogen (MBL). Murine monoclonal antibody (mAb) against Myl9/12 (114-2G9, KAN Research Institute Inc.) and rabbit mAb against Myl9/12 (F-6, Abwiz bio Inc.) were made by immunization with N-terminal peptides of Myl9 (residues 1 to 27).

IP and immunoblotting

GST-fusion recombinant proteins (Myl9, Myl12a, Myl12b, and Myl3) were mixed with 3×Flag-CD69EC overnight and then subjected to IP with an anti-Flag antibody (M2; Sigma-Aldrich) coupled with Dynabeads (Life Technologies) at 4°C for 3 hours. Binding proteins were eluted from the beads by 3×Flag peptides (Sigma-Aldrich) and then subjected to SDS-PAGE and immunoblotting (IB), as described previously (*52*). As indicated, recombinant affinity-purified 3×Flag-CD69EC proteins were treated with PNGase F (NEB P0704) according to the manufacturer's protocol and used for further assays. For detection of Myl9/12 protein expression, cell or tissue lysates were prepared using radioimmunoprecipitation assay buffer and then used for IB. The antibodies used for IB were anti-GST biotin (Rockland), anti–Penta·His Biotin (Qiagen), anti-Flag (M2; Sigma-Aldrich), anti-Myl9/12, anti–tubulin-α (NeoMarkers), streptavidin–horseradish peroxidase (HRP; Jackson Laboratory), antirabbit IgG-HRP, and antimouse IgG-HRP (GE Healthcare).

Enzyme-linked immunosorbent assay

Purified GST-His-Myl9 or GST-His-Myl3 was directly added to a plate for coating or was added to a glutathione-coated plate (Thermo Pierce). After blocking of the coated plates with Block Ace (DS Pharma), PNGase F–treated or nontreated affinity-purified 3×Flag-CD69EC proteins were added and incubated at room temperature for 1 hour. The binding of CD69 to Myl9 was detected by HRP-conjugated anti-Flag antibody (Sigma) and tetramethylbenzidine (TMB) solution (Bio-Rad Laboratories). For detection of soluble Myl9 protein, anti-Myl9 mAb (Abcam) was directly coated on a plate. After blocking, culture supernatants were added and then reacted with biotinylated anti-Myl9/12 (F-6) mAb. Binding of Myl9 was detected by HRP-conjugated streptavidin (Jackson Laboratory).

Measurement of airway hyperreactivity and airway inflammation

OVA-induced allergic airway inflammation was induced as previously described (*5*, *53*). In brief, BALB/c mice were immunized with OVA in aluminum hydroxide gel (alum) on days 0 and 7, followed by aerosolized OVA inhalation on days 14 and 16. As indicated, polyclonal and monoclonal (114-2G9) anti-Myl9/12 or isotype control antibodies (100 μg) were intraperitoneally injected on days 13 and 15. For platelet depletion, anti-GPIbα antibody (emfret ANALYTICS) was intravenously injected (4 μg/g) on days 13 and 15. BAL, AHR assessment, and immunohistological analysis were performed at 24 hours after the last OVA challenge. The absolute number of infiltrating cells in BAL fluid was obtained using percentages of cells and total cell number of BAL fluid recovered. To measure cytokine production in BAL fluid, we first removed mononuclear cells by centrifugation and measured specific cytokine production by BD Cytometric Bead Array (BD Pharmingen). AHR was assessed by methacholine (Sigma-Aldrich)–induced airflow obstruction at 24 hours after the last antigen challenge using a computer-controlled small animal ventilator (SCIREQ). For histological analysis of asthmatic lungs, the mice were killed at 48 hours after the last OVA challenge, and hematoxylin and eosin (H&E) or periodic acid–Schiff (PAS) staining was performed (*5*).

For HDM-induced allergic airway inflammation, 3-day consecutive intranasal administrations with HDM (50 μg) were performed in BALB/c mice for 3 weeks. Monoclonal anti-Myl9/12 (F-6) or isotype control antibodies (100 μg) were intraperitoneally injected 1 day before HDM administration and on the second day of HDM administration in each session. BAL and immunohistological analysis were performed at 24 hours after the last HDM administration. HDM were provided by Torii Pharmaceutical Co., Ltd. (Tokyo, Japan).

Immunofluorescent staining and confocal microscopy

For immunofluorescent staining, cryostat sections of lungs were fixed in 4% paraformaldehyde and then stained and mounted with fluorescent mounting medium (DakoCytomation). For BM analysis, adult femurs were fixed in 4% paraformaldehyde and equilibrated in 30% sucrose/PBS. Histological analyses were carried out with a confocal laser microscope (LSM710; Carl Zeiss). Polyclonal antibodies against PECAM-1 (Santa Cruz Biotechnology) and vWF (Abcam), and mAbs against Myl9/12 (F-6), CD41 (MWReg30; BD Pharmingen), TER119 (BD Pharmingen), and human CD69 (FN50; BD Pharmingen) were used. For secondary antibodies, Alexa Fluor 488–labeled antirabbit antibodies, Alexa Fluor 555–labeled antigoat antibodies, Alexa Fluor 647–labeled antimouse IgG antibodies, and Alexa Fluor 546–labeled antisheep IgG antibodies (Invitrogen) were used. For nuclear and cytoplasmic staining, 4′,6-diamidino-2-phenylindole (DAPI), TO-PRO-3, and CellMask Orange (Invitrogen) were used. For quantitative analysis, fluorescence intensity was measured with a digital microscope (BZ-X710; Keyence). Data sets were rendered and analyzed with ImageJ and Imaris software (Bitplane).

Quantitative reverse transcription polymerase chain reaction

Total RNA was isolated with TRIzol reagent (Invitrogen), and cDNA synthesis was performed using Superscript II (Invitrogen) with oligo(dT) primers. Quantitative reverse transcription polymerase chain reaction

was performed with a TaqMan Universal PCR Master Mix (Applied Biosystems). The primers for TaqMan probes for the detection of *Myl9*, *Myl12a*, *Myl12b*, *Mac5ac*, and *Hprt* were purchased from Applied Biosystems. Gene expression levels were normalized to those of *Hprt* in the same sample.

Preparation of platelet-rich plasma

Platelet-rich plasma (PRP) was prepared from peripheral blood as previously described (*24*). Platelets were activated by thrombin (1 U/ml) together with $CaCl_2$ (1 mM) in Tyrode buffer [134 mM NaCl, 2.9 mM KCl, 0.34 mM Na_2PO_4, 12 mM $NaHCO_3$, 20 mM Hepes, 1 mM $MgCl_2$, 5 mM glucose, and 0.5 mg/ml bovine serum albumin (pH 6.5)] at 37°C for the indicated times, fixed in 4% paraformaldehyde on a slide glass, permeabilized (0.3% Triton X-100 and 5% fetal calf serum in PBS), and then stained with the described antibodies.

Preparation of nasal polyp section from ECRS patients

Nasal polyp tissues were obtained from ECRS patients during endoscopic sinus surgery, as previously described (*30*). Nasal mucosa obtained from patients with deviation of the nasal septum was used as control. For histological analysis, cryostat sections of nasal polyp tissues were fixed in 4% paraformaldehyde, stained, and mounted with fluorescent mounting medium (DakoCytomation). All patients signed an informed consent form, and the study was approved by the ethics committee of the Chiba University Graduate School of Medicine.

SUPPLEMENTARY MATERIALS

immunology.sciencemag.org/cgi/content/full/1/3/eaaf9154/DC1

Materials and Methods

Fig. S1. Identification of Myl9/12 as interacting proteins for CD69.

Fig. S2. Impacts of polyclonal anti-Myl9/12 antibodies on OVA-induced airway inflammation.

Fig. S3. Myl9/12 expression in the lung.

Fig. S4. Myl9/12 protein expression in platelets.

Fig. S5. Detection of $CD69^+$ antigen-specific CD4 T cells in the lung vasculature during airway inflammation.

Fig. S6. Effects of anti-Myl9/12 and antihuman CD69 antibodies on human CD69-mediated allergic airway inflammation.

Fig. S7. Distribution of $CD69^+$ T cells and Myl9/12 expression in polyps of ECRS patients.

Fig. S8. Unmodified images and isotype control staining in immunohistochemistry.

Movie S1. Myl9/12 form net-like structures in blood vessels of the inflamed lung.

REFERENCES AND NOTES

1. S. F. Ziegler, F. Ramsdell, K. A. Hjerrild, R. J. Armitage, K. H. Grabstein, K. B. Hennen, T. Farrah, W. C. Fanslow, E. M. Shevach, M. R. Alderson, Molecular characterization of the early activation antigen CD69: A type II membrane glycoprotein related to a family of natural killer cell activation antigens. *Eur. J. Immunol.* **23**, 1643–1648 (1993).
2. I. Yamashita, T. Nagata, T. Tada, T. Nakayama, Cd69 cell-surface expression identifies developing thymocytes which audition for T cell antigen receptor-mediated positive selection. *Int. Immunol.* **5**, 1139–1150 (1993).
3. S. F. Ziegler, F. Ramsdell, M. R. Alderson, The activation antigen CD69. *Stem Cells* **12**, 456–465 (1994).
4. S. R. Schwab, J. G. Cyster, Finding a way out: Lymphocyte egress from lymphoid organs. *Nat. Immunol.* **8**, 1295–1301 (2007).
5. T. Miki-Hosokawa, A. Hasegawa, C. Iwamura, K. Shinoda, S. Tofukuji, Y. Watanabe, H. Hosokawa, S. Motohashi, K. Hashimoto, M. Shirai, M. Yamashita, T. Nakayama, CD69 controls the pathogenesis of allergic airway inflammation. *J. Immunol.* **183**, 8203–8215 (2009).
6. K. Murata, M. Inami, A. Hasegawa, S. Kubo, M. Kimura, M. Yamashita, H. Hosokawa, T. Nagao, K. Suzuki, K. Hashimoto, H. Shinkai, H. Koseki, M. Taniguchi, S. F. Ziegler, T. Nakayama, CD69-null mice protected from arthritis induced with anti-type II collagen antibodies. *Int. Immunol.* **15**, 987–992 (2003).
7. K. Shinoda, K. Tokoyoda, A. Hanazawa, K. Hayashizaki, S. Zehentmeier, H. Hosokawa, C. Iwamura, H. Koseki, D. J. Tumes, A. Radbruch, T. Nakayama, Type II membrane protein CD69 regulates the formation of resting T-helper memory. *Proc. Natl. Acad. Sci. U.S.A.* **109**, 7409–7414 (2012).
8. A. Hasegawa, C. Iwamura, M. Kitajima, K. Hashimoto, K.-i. Otsuyama, H. Ogino, T. Nakayama, M. Shirai, Crucial role for CD69 in the pathogenesis of dextran sulphate sodium–induced colitis. *PLOS One* **8**, e65494 (2013).
9. K. Tokoyoda, S. Zehentmeier, A. N. Hegazy, I. Albrecht, J. R. Grün, M. Löhning, A. Radbruch, Professional memory $CD4^+$ T lymphocytes preferentially reside and rest in the bone marrow. *Immunity* **30**, 721–730 (2009).
10. A. Hartnell, D. S. Robinson, A. B. Kay, A. J. Wardlaw, Cd69 is expressed by human eosinophils activated in vivo in asthma and in vitro by cytokines. *Immunology* **80**, 281–286 (1993).
11. K. Nishikawa, T. Morii, H. Ako, K. Hamada, S. Saito, N. Narita, In vivo expression of CD69 on lung eosinophils in eosinophilic pneumonia: CD69 as a possible activation marker for eosinophils. *J. Allergy Clin. Immunol.* **90**, 169–174 (1992).
12. D. L. Hamilos, Chronic rhinosinusitis: Epidemiology and medical management. *J. Allergy Clin. Immunol.* **128**, 693–707 (2011).
13. N. Van Bruaene, C. A. Pérez-Novo, T. M. Basinski, T. Van Zele, G. Holtappels, N. De Ruyck, C. Schmidt-Weber, C. Akdis, P. Van Cauwenberge, C. Bachert, P. Gevaert, T-cell regulation in chronic paranasal sinus disease. *J. Allergy Clin. Immunol.* **121**, 1435–1441 (2008).
14. N. Zhang, T. Van Zele, C. Perez-Novo, N. Van Bruaene, G. Holtappels, N. DeRuyck, P. Van Cauwenberge, C. Bachert, Different types of T-effector cells orchestrate mucosal inflammation in chronic sinus disease. *J. Allergy Clin. Immunol.* **122**, 961–968 (2008).
15. P.-P. Cao, H.-B. Li, B.-F. Wang, S.-B. Wang, X.-J. You, Y.-H. Cui, D.-Y. Wang, M. Desrosiers, Z. Liu, Distinct immunopathologic characteristics of various types of chronic rhinosinusitis in adult Chinese. *J. Allergy Clin. Immunol.* **124**, 478–484 (2009).
16. T. Nakayama, M. Yoshikawa, D. Asaka, T. Okushi, Y. Matsuwaki, N. Otori, T. Hama, H. Moriyama, Mucosal eosinophilia and recurrence of nasal polyps—New classification of chronic rhinosinusitis. *Rhinology* **49**, 392–396 (2011).
17. Y. Sakuma, J. Ishitoya, M. Komatsu, O. Shiono, M. Hirama, Y. Yamashita, T. Kaneko, S. Morita, M. Tsukuda, New clinical diagnostic criteria for eosinophilic chronic rhinosinusitis. *Auris Nasus Larynx* **38**, 583–588 (2011).
18. W. J. Fokkens, V. J. Lund, J. Mullol, C. Bachert, I. Alobid, F. Baroody, N. Cohen, A. Cervin, R. Douglas, P. Gevaert, C. Georgalas, H. Goossens, R. Harvey, P. Hellings, C. Hopkins, N. Jones, G. Joos, L. Kalogjera, B. Kern, M. Kowalski, D. Price, H. Riechelmann, R. Schlosser, B. Senior, M. Thomas, E. Toskala, R. Voegels, D. Y. Wang, P. J. Wormald, EPOS 2012: European position paper on rhinosinusitis and nasal polyps 2012. A summary for otorhinolaryngologists. *Rhinology* **50**, 1–12 (2012).
19. K. Shinoda, K. Hirahara, T. Iinuma, T. Ichikawa, A. S. Suzuki, K. Sugaya, D. J. Tumes, H. Yamamoto, T. Hara, S. Tani-ichi, K. Ikuta, Y. Okamoto, T. Nakayama, $Thy1^+IL\text{-}7^+$ lymphatic endothelial cells in iBALT provide a survival niche for memory T-helper cells in allergic airway inflammation. *Proc. Natl. Acad. Sci. U.S.A.* **113**, E2842–E2851 (2016).
20. M. Vicente-Manzanares, X. Ma, R. S. Adelstein, A. R. Horwitz, Non-muscle myosin II takes centre stage in cell adhesion and migration. *Nat. Rev. Mol. Cell Biol.* **10**, 778–790 (2009).
21. L. Gilles, D. Bluteau, S. Boukour, Y. Chang, Y. Zhang, T. Robert, P. Dessen, N. Debili, O. A. Bernard, W. Vainchenker, H. Raslova, MAL/SRF complex is involved in platelet formation and megakaryocyte migration by regulating MYL9 (MLC2) and MMP9. *Blood* **114**, 4221–4232 (2009).
22. M. Seri, R. Cusano, S. Gangarossa, G. Caridi, D. Bordo, C. Lo Nigro, G. M. Ghiggeri, R. Ravazzolo, M. Savino, M. Del Vecchio, M. d'Apolito, A. Iolascon, L. L. Zelante, A. Savoia, C. L. Balduini, P. Noris, U. Magrini, S. Belletti, K. E. Heath, M. Babcock, M. J. Glucksman, E. Aliprandis, N. Bizzaro, R. J. Desnick, J. A. Martignetti, Mutations in *MYH9* result in the May-Hegglin anomaly, and Fechtner and Sebastian syndromes. The May-Heggllin/Fechtner Syndrome Consortium. *Nat. Genet.* **26**, 103–105 (2000).
23. B. A. Garcia, D. M. Smalley, H. Cho, J. Shabanowitz, K. Ley, D. F. Hunt, The platelet microparticle proteome. *J. Proteome Res.* **4**, 1516–1521 (2005).
24. B. D. Elzey, J. Tian, R. J. Jensen, A. K. Swanson, J. R. Lees, S. R. Lentz, C. S. Stein, B. Nieswandt, Y. Wang, B. L. Davidson, T. L. Ratliff, Platelet-mediated modulation of adaptive immunity: A communication link between innate and adaptive immune compartments. *Immunity* **19**, 9–19 (2003).
25. K. G. Anderson, K. Mayer-Barber, H. Sung, L. Beura, B. R. James, J. J. Taylor, L. Qunaj, T. S. Griffith, V. Vezys, D. L. Barber, D. Masopust, Intravascular staining for discrimination of vascular and tissue leukocytes. *Nat. Protoc.* **9**, 209–222 (2014).
26. R. Testi, D. D'Ambrosio, R. De Maria, A. Santoni, The CD69 receptor: A multipurpose cell-surface trigger for hematopoietic cells. *Immunol. Today* **15**, 479–483 (1994).
27. W. W. Stevens, R. J. Lee, R. P. Schleimer, N. A. Cohen, Chronic rhinosinusitis pathogenesis. *J. Allergy Clin. Immunol.* **136**, 1442–1453 (2015).
28. K. E. Hulse, Immune mechanisms of chronic rhinosinusitis. *Curr. Allergy Asthma Rep.* **16**, 1 (2016).
29. D.-Y. Kim, S. H. Cho, T. Takabayashi, R. P. Schleimer, Chronic rhinosinusitis and the coagulation system. *Allergy Asthma Immunol. Res.* **7**, 421–430 (2015).

30. H. Yamamoto, Y. Okamoto, S. Horiguchi, N. Kunii, S. Yonekura, T. Nakayama, Detection of natural killer T cells in the sinus mucosa from asthmatics with chronic sinusitis. *Allergy* **62**, 1451–1455 (2007).
31. Y. Endo, K. Hirahara, T. Iinuma, K. Shinoda, D. J. Tumes, H. K. Asou, N. Matsugae, K. Obata-Ninomiya, H. Yamamoto, S. Motohashi, K. Oboki, S. Nakae, H. Saito, Y. Okamoto, T. Nakayama, The interleukin-33–p38 kinase axis confers memory T helper 2 cell pathogenicity in the airway. *Immunity* **42**, 294–308 (2015).
32. M. F. Krummel, F. Bartumeus, A. Gérard, T cell migration, search strategies and mechanisms. *Nat. Rev. Immunol.* **16**, 193–201 (2016).
33. J. W. Griffith, C. L. Sokol, A. D. Luster, Chemokines and chemokine receptors: Positioning cells for host defense and immunity. *Annu. Rev. Immunol.* **32**, 659–702 (2014).
34. U. H. von Andrian, T. R. Mempel, Homing and cellular traffic in lymph nodes. *Nat. Rev. Immunol.* **3**, 867–878 (2003).
35. K. Ley, G. S. Kansas, Selectins in T-cell recruitment to non-lymphoid tissues and sites of inflammation. *Nat. Rev. Immunol.* **4**, 325–335 (2004).
36. M. Kelly, J. M. Hwang, P. Kubes, Modulating leukocyte recruitment in inflammation. *J. Allergy Clin. Immunol.* **120**, 3–10 (2007).
37. J. G. Cyster, S. R. Schwab, Sphingosine-1-phosphate and lymphocyte egress from lymphoid organs. *Annu. Rev. Immunol.* **30**, 69–94 (2012).
38. D. F. Choy, K. M. Hart, L. A. Borthwick, A. Shikotra, D. R. Nagarkar, S. Siddiqui, G. Jia, C. M. Ohri, E. Doran, K. M. Vannella, C. A. Butler, B. Hargadon, J. C. Sciurba, R. L. Gieseck, R. W. Thompson, S. White, A. R. Abbas, J. Jackman, L. C. Wu, J. G. Egen, L. G. Heaney, T. R. Ramalingam, J. R. Arron, T. A. Wynn, P. Bradding, T_H2 and T_H17 inflammatory pathways are reciprocally regulated in asthma. *Sci. Transl. Med.* **7**, 301ra129 (2015).
39. N. A. Gandhi, B. L. Bennett, N. M. H. Graham, G. Pirozzi, N. Stahl, G. D. Yancopoulos, Targeting key proximal drivers of type 2 inflammation in disease. *Nat. Rev. Drug Discov.* **15**, 35–50 (2016).
40. H. Hammad, B. N. Lambrecht, Barrier epithelial cells and the control of type 2 immunity. *Immunity* **43**, 29–40 (2015).
41. C. M. Lloyd, S. Saglani, Epithelial cytokines and pulmonary allergic inflammation. *Curr. Opin. Immunol.* **34**, 52–58 (2015).
42. C. Page, S. Pitchford, Platelets and allergic inflammation. *Clin. Exp. Allergy* **44**, 901–913 (2014).
43. E. A. Caspary, J. S. Comaish, Release of serotonin from human platelets in hypersensitivity states. *Nature* **214**, 286–287 (1967).
44. S. C. Pitchford, C. P. Page, Platelet activation in asthma: Integral to the inflammatory response. *Clin. Exp. Allergy* **36**, 399–401 (2006).
45. G. Pelaia, A. Vatrella, R. Maselli, The potential of biologics for the treatment of asthma. *Nat. Rev. Drug Discov.* **11**, 958–972 (2012).
46. M. E. Rothenberg, Humanized anti-IL-5 antibody therapy. *Cell* **165**, 509 (2016).
47. E. H. Bel, S. E. Wenzel, P. J. Thompson, C. M. Prazma, O. N. Keene, S. W. Yancey, H. G. Ortega, I. D. Pavord; SIRIUS Investigators, Oral glucocorticoid-sparing effect of mepolizumab in eosinophilic asthma. *N. Engl. J. Med.* **371**, 1189–1197 (2014).
48. M. Castro, J. Zangrilli, M. E. Wechsler, E. D. Bateman, G. G. Brusselle, P. Bardin, K. Murphy, J. F. Maspero, C. O'Brien, S. Korn, Reslizumab for inadequately controlled asthma with elevated blood eosinophil counts: Results from two multicentre, parallel, double-blind, randomised, placebo-controlled, phase 3 trials. *Lancet Respir. Med.* **3**, 355–366 (2015).
49. J. W. Semple, J. E. Italiano Jr., J. Freedman, Platelets and the immune continuum. *Nat. Rev. Immunol.* **11**, 264–274 (2011).
50. K. M. Murphy, A. B. Heimberger, D. Y. Loh, Induction by antigen of intrathymic apoptosis of $CD4^+CD8^+$TCRlo thymocytes in vivo. *Science* **250**, 1720–1723 (1990).
51. J. North, I. Bakhsh, C. Marden, H. Pittman, E. Addison, C. Navarrete, R. Anderson, M. W. Lowdell, Tumor-primed human natural killer cells lyse NK-resistant tumor targets: Evidence of a two-stage process in resting NK cell activation. *J. Immunol.* **178**, 85–94 (2007).
52. M. Omori, M. Yamashita, M. Inami, M. Ukai-Tadenuma, M. Kimura, Y. Nigo, H. Hosokawa, A. Hasegawa, M. Taniguchi, T. Nakayama, CD8 T cell-specific downregulation of histone hyperacetylation and gene activation of the IL-4 gene locus by ROG, repressor of GATA. *Immunity* **19**, 281–294 (2003).
53. A. Hasegawa, K. Hayashi, H. Kishimoto, M. Yang, S. Tofukuji, K. Suzuki, H. Nakajima, R. M. Hoffman, M. Shirai, T. Nakayama, Color-coded real-time cellular imaging of lung T-lymphocyte accumulation and focus formation in a mouse asthma model. *J. Allergy Clin. Immunol.* **125**, 461–468.e6 (2010).

Acknowledgments: We thank M. Kato, A. Igi, K. Sugaya, A. Suzuki, K. Obata-Ninomiya, H. Kato, T. Ito, K. Katakura, and M. A. McGrath for their expert technical assistance. We thank K. Eto, I. Manabe, Y. Rikitake, A. Singer, Y. Takai, and N. Yamaguchi for helpful discussions. We thank Y. Suwazono for consulting statistical analysis in this study. **Funding:** This work was supported by the Ministry of Education, Culture, Sports, Science, and Technology, Japan; Grants-in Aid for Scientific Research (S) (26221305), Scientific Research (C) (26460569), Young Scientists (A) (22689014), Young Scientists (B) (25860352 and 26860315), and Japan Society for the Promotion of Science Fellows (2502883); Practical Research Project for Allergic Diseases and Immunology from Japan Agency for Medical Research and Development (AMED); the Takeda Science Foundation; the Uehara Memorial Foundation; and the Leibniz Association (International Leibniz Research Cluster "ImmunoMemory"). **Author contributions:** K.Ha., M.Y.K., and K.T. designed and performed the experiments and interpreted the data. H.H., K.S., K.Hi., T.Ic., A.O., A.H., C.I., S.M., D.J.T., and Y.I. performed the experiments, analyzed the data, and provided helpful discussions. T.Ii., H.Y., and Y.O. engaged in human sample experiments. K.Ha., M.Y.K., and T.N. wrote the manuscript. J.K. and K.M. produced mAb. T.N. led the investigation and contributed to the design and interpretation of data. **Competing interests:** J.K. and K.M. are employees of KAN Research Institute Inc. The patent (Japan) is pending. The other authors declare that they have no competing interests.

Submitted 19 April 2016
Accepted 24 August 2016
Published 16 September 2016
10.1126/sciimmunol.aaf9154

Citation: K. Hayashizaki, M. Y. Kimura, K. Tokoyoda, H. Hosokawa, K. Shinoda, K. Hirahara, T. Ichikawa, A. Onodera, A. Hanazawa, C. Iwamura, J. Kakuta, K. Muramoto, S. Motohashi, D. J. Tumes, T. Iinuma, H. Yamamoto, Y. Ikehara, Y. Okamoto, T. Nakayama, Myosin light chains 9 and 12 are functional ligands for CD69 that regulate airway inflammation. *Sci. Immunol.* **1**, eaaf9154 (2016).

INFECTIOUS DISEASE

ZBP1/DAI is an innate sensor of influenza virus triggering the NLRP3 inflammasome and programmed cell death pathways

Teneema Kuriakose *et al.* (Thirumala-Devi Kanneganti)

Citation
Sci. Immunol. 12 Aug 2016:
Vol. 1, Issue 2, eaag2045

10.1126/sciimmunol.aag2045

The interferon (IFN)–inducible protein Z-DNA binding protein 1 [ZBP1; also known as DNA-dependent activator of IFN regulatory factors (DAI) and DLM-1] was identified as a double-stranded DNA sensor, which instigates innate immune responses. However, this classification has been disputed, and whether ZBP1 functions as a pathogen sensor during an infection has remained unknown. We demonstrated ZBP1-mediated sensing of the influenza A virus (IAV) proteins NP and PB1, triggering cell death and inflammatory responses via the receptor-interacting protein kinase 1 (RIPK1)–RIPK3–caspase-8 axis. ZBP1 regulates NLRP3 (nucleotide and oligomerization domain, leucine-rich repeat–containing protein family, pyrin domain containing 3) inflammasome activation as well as induction of apoptosis, necroptosis, and pyroptosis in IAV-infected cells. ZBP1 deficiency protected mice from mortality during IAV infection owing to reduced inflammatory responses and epithelial damage. Overall, these findings indicate that ZBP1 is an innate immune sensor of IAV and highlight its importance in the pathogenesis of IAV infection.

CANCER

Lectin-type oxidized LDL receptor-1 distinguishes population of human polymorphonuclear myeloid-derived suppressor cells in cancer patients

Thomas Condamine *et al.* (Dmitry I. Gabrilovic)

Citation
Sci. Immunol. 05 Aug 2016:
Vol. 1, Issue 2, eaaf8943

10.1126/sciimmunol.aaf8943

Polymorphonuclear myeloid-derived suppressor cells (PMN-MDSCs) are important regulators of immune responses in cancer and have been directly implicated in the promotion of tumor progression. However, the heterogeneity of these cells and the lack of distinct markers hamper the progress in understanding the biology and clinical importance of these cells. Using partial enrichment of PMN-MDSC with gradient centrifugation, we determined that low-density PMN-MDSC and high-density neutrophils from the same cancer patients had a distinct gene profile. The most prominent changes were observed in the expression of genes associated with endoplasmic reticulum (ER) stress. Unexpectedly, low-density lipoprotein (LDL) was one of the most increased regulators, and its receptor oxidized LDL receptor 1 (OLR1) was one of the most overexpressed genes in PMN-MDSC. Lectin-type oxidized LDL receptor-1 (LOX-1) encoded by OLR1 was practically undetectable in neutrophils in peripheral blood of healthy donors, whereas 5 to 15% of total neutrophils in cancer patients and 15 to 50% of neutrophils in tumor tissues were LOX-1$^+$. In contrast to their LOX-1$^-$ counterparts, LOX-1$^+$ neutrophils had gene signature, potent immunosuppressive activity, up-regulation of ER stress, and other biochemical characteristics of PMN-MDSCs. Moreover, induction of ER stress in neutrophils from healthy donors up-regulated LOX-1 expression and converted these cells to suppressive PMN-MDSCs. Thus, we identified a specific marker of human PMN-MDSC associated with ER stress and lipid metabolism, which provides new insights into the biology and potential therapeutic targeting of these cells.

SCIENCE ONE-STOP PUBLISHING

Submit your research to a one-stop shop publisher for your immunology paper. Save time, reduce costs and improve efficiencies when publishing with a trusted peer-review across the *Science* family of journals.

SUBMIT YOUR PAPER
Immunology paper submitted to *Science* family journals.

TRANSFER
If a manuscript is rejected, it can be transferred to a sister *Science* journal of the author's choice.

REDUCE, REUSE, RECYLE
At your request, the recipient journal may use information and reviews gathered during the initial evaluation.

NEW REVIEW
Option for a new review is also possible. The transfer can include documents from the initial submission.

FEEDBACK
After transfer, revise your manuscript to respond to reviewers.

Learn more about publishing in the *Science* family of journals at:
sciencemag.org/authors/contributing-science-family-journals

Science | Science Advances | Science Immunology
Science Signaling | Science Translational Medicine

Science Signaling

IMMUNOLOGY

Distinct microenvironmental cues stimulate divergent TLR4-mediated signaling pathways in macrophages

Anna M. Piccinini,* Lorena Zuliani-Alvarez, Jenny M. P. Lim, Kim S. Midwood†

Macrophages exhibit a phenotypic plasticity that enables them to orchestrate specific immune responses to distinct threats. The microbial product lipopolysaccharide (LPS) and the extracellular matrix glycoprotein tenascin-C are released during bacterial infection and tissue injury, respectively, and both activate Toll-like receptor 4 (TLR4). We found that these two TLR4 ligands stimulated distinct signaling pathways in macrophages, resulting in cells with divergent phenotypes. Although macrophages activated by LPS or tenascin-C displayed some common features, including activation of nuclear factor κB and mitogen-activated protein kinase signaling and cytokine synthesis, each ligand stimulated the production of different subsets of cytokines and generated different phosphoproteomic signatures. Moreover, tenascin-C promoted the generation of macrophages that exhibited increased synthesis and phosphorylation of extracellular matrix components, whereas LPS stimulated the production of macrophages that exhibited an enhanced capacity to degrade the matrix. These data reveal how the activation of one pattern recognition receptor by different microenvironmental cues generates macrophage with distinct phenotypes.

INTRODUCTION

Macrophages are innate immune sentinels that patrol most tissues in the body. These cells detect changes in the microenvironment, including pathogen invasion and tissue damage, and mediate inflammatory processes, in response, that destroy microbial interlopers, remove and repair damaged tissue, and restore homeostasis (*1*). Macrophages are versatile cells that orchestrate both the induction and the resolution of inflammation. They can be driven toward a proinflammatory phenotype or a tissue repair phenotype by specific differentiation protocols in vitro. However, a much larger spectrum of macrophage subsets exists in vivo, enabling a context-dependent response to specific types and locations of threat (*2*). The microenvironment of these cells is therefore key to defining their behavior; both the surrounding cocktail of soluble cues (including cytokines, growth factors, and microbial products) and the network of extracellular matrix molecules specific to the tissue location of the macrophage affect its function (*3*, *4*). Accumulating evidence demonstrates how environmental factors, including heme (*5*), retinoic acid (*6*), and transforming growth factor–β (TGF-β) (*7*), influence the specialization of tissue-resident macrophages. Moreover, studies of the transfer of tissue-resident macrophages to a different tissue showed that the microenvironment can reprogram fully differentiated macrophages (*4*).

Macrophages have pattern recognition receptors (PRRs), including Toll-like receptors (TLRs), nucleotide-binding oligomerization domain (NOD)–like receptors, retinoic acid–inducible gene 1 family members, lectins, and scavenger receptors, which they use to sense changes in the microenvironment (*8*). PRRs detect various threats; although receptor specificity exists, there is also a surprising amount of overlap in ligand recognition. For example, TLRs recognize pathogen-derived molecules, ranging from bacterial lipoproteins to viral nucleic acids, as well as endogenous molecules generated upon tissue damage, including self nucleic acids, phospholipids, small organic molecules, fatty acids, and various proteins and proteoglycans (*9*). This convergence of distinct microenvironmental signals on the same receptor family has raised the question of whether infection and sterile tissue injury are interpreted equivalently by the innate immune system. Although the mechanisms of pathogen-mediated TLR activation, signaling, and downstream inflammatory responses have been extensively investigated, those mediated by cues that indicate sterile tissue damage remain enigmatic.

We sought to undertake a systematic analysis of the signaling pathways and biological outcomes induced by two different stimuli, from infected and damaged microenvironments, respectively, that activate the same PRR. We directly compared two TLR4 activators: the Gram-negative bacterial lipopolysaccharide (LPS) and tenascin-C, an extracellular matrix glycoprotein that is produced specifically upon tissue injury (*10*). The activation of TLR4 by tenascin-C stimulates cytokine synthesis in various cells, including macrophages and fibroblasts (*11*–*13*). Although it is transiently produced upon tissue damage, tenascin-C is persistently found in chronic inflammatory diseases and in tumors (*10*). We previously demonstrated that the C-terminal fibrinogen-like globe (FBG) domain of tenascin-C is responsible for TLR4 activation and that this domain is potently arthritogenic, driving persistent TLR4-mediated disease in models of inflammatory arthritis (*11*). Here, we showed that activation of TLR4 by LPS or FBG generated macrophages with two distinct phenotypes, which displayed different activation markers, secreted different effector molecules, and induced different phosphoproteomic profiles underlying distinct signaling pathways and protein-protein interaction networks and generating macrophages with distinct catabolic and anabolic abilities. Together, our data provide evidence that the innate immune system can interpret the context of an inflammatory cue and orchestrate inflammation accordingly by instructing macrophage behavior.

RESULTS

LPS and the FBG domain of tenascin-C stimulate distinct macrophage activation phenotypes

LPS recognition by TLR4 induces a well-defined macrophage phenotype (*2*). To determine whether the activation of TLR4 by FBG promotes a

Kennedy Institute of Rheumatology, Nuffield Department of Orthopaedics, Rheumatology and Musculoskeletal Sciences, University of Oxford, Headington, Oxford OX3 7FY, U.K.
*Present address: School of Pharmacy, University of Nottingham, Nottingham NG7 2RD, U.K.
†Corresponding author. Email: kim.midwood@kennedy.ox.ac.uk

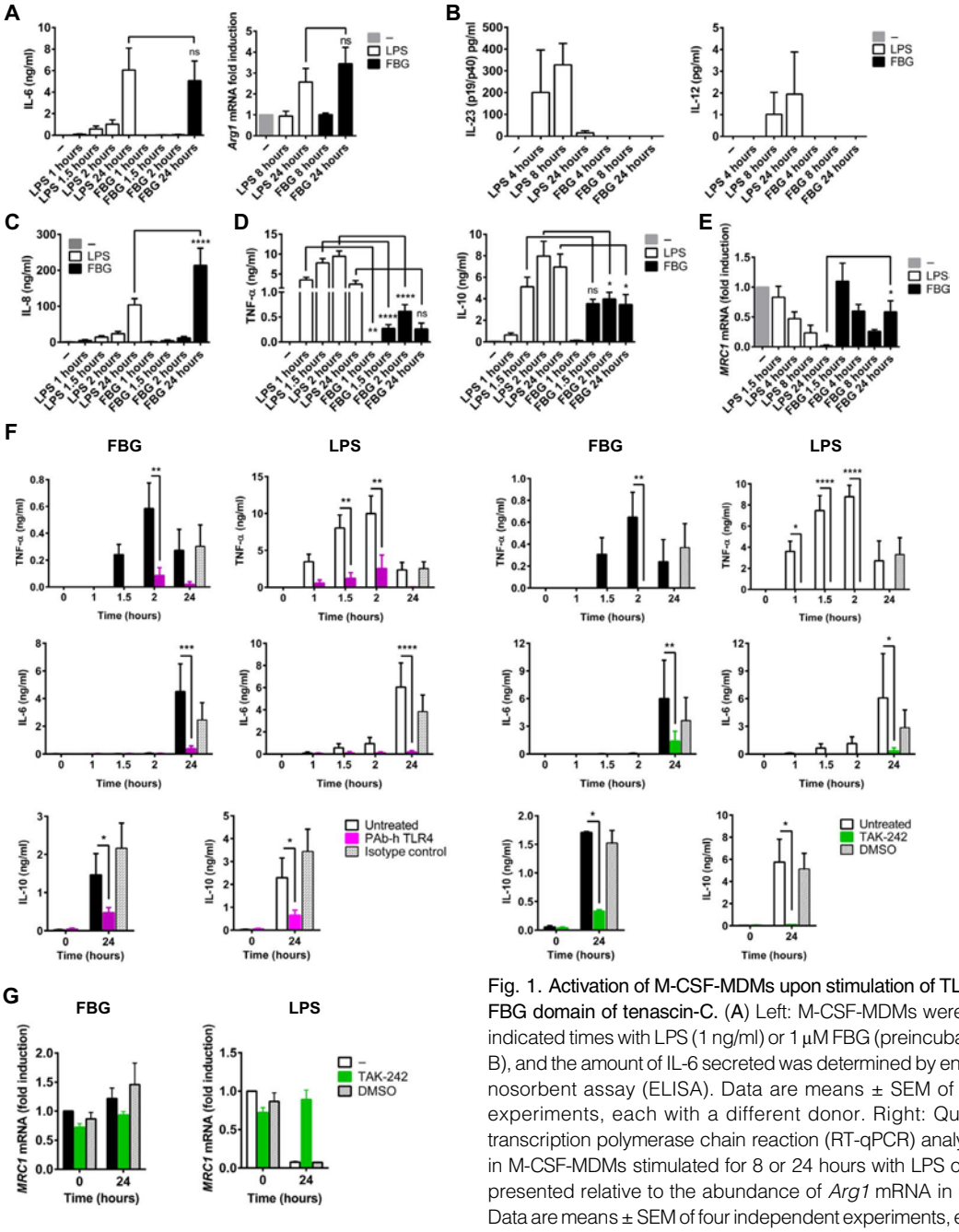

Fig. 1. Activation of M-CSF-MDMs upon stimulation of TLR4 with LPS or the FBG domain of tenascin-C. (**A**) Left: M-CSF-MDMs were stimulated for the indicated times with LPS (1 ng/ml) or 1 μM FBG (preincubated with polymyxin B), and the amount of IL-6 secreted was determined by enzyme-linked immunosorbent assay (ELISA). Data are means ± SEM of nine independent experiments, each with a different donor. Right: Quantitative reverse transcription polymerase chain reaction (RT-qPCR) analysis of *Arg1* mRNA in M-CSF-MDMs stimulated for 8 or 24 hours with LPS or FBG. Results are presented relative to the abundance of *Arg1* mRNA in unstimulated cells. Data are means ± SEM of four independent experiments, each with a different donor. ns, not significant by one-way analysis of variance (ANOVA). (**B** to **D**) M-CSF-MDMs were stimulated for the indicated times with LPS or FBG as described in (A) before the amounts of IL-23 and IL-12 (B), IL-8 (C), and TNF-α and IL-10 (D) secreted were determined by ELISA. Data are means ± SEM of five to nine independent experiments, each with a different donor. $^{*}P < 0.05$, $^{**}P < 0.01$, $^{****}P < 0.0001$ by one-way ANOVA. (**E**) RT-qPCR analysis of *MRC1* mRNA in M-CSF-MDMs stimulated for the indicated times with LPS or FBG. Results are presented relative to the abundance of *MRC1* mRNA in unstimulated cells. Data are means ± SEM of four independent experiments, each with a different donor. $^{*}P < 0.05$ by one-way ANOVA. (**F**) M-CSF-MDMs were stimulated for the indicated times with LPS or FBG in the presence or absence of polyclonal anti-human TLR4 antibody (pAb-h TLR4) or isotype control (left) or 3 μM TAK-242 or dimethyl sulfoxide (DMSO) (right). The amounts of TNF-α, IL-6, and IL-10 secreted were determined by ELISA. Data are means ± SEM of three to five (left) or three or four (right) independent experiments, each with a different donor. $^{*}P < 0.05$, $^{**}P < 0.01$, $^{***}P < 0.001$, $^{****}P < 0.0001$ by two-way ANOVA. (**G**) RT-qPCR analysis of *MRC1* mRNA in M-CSF-MDMs stimulated for 24 hours with LPS or FBG in the presence or absence of 3 μM TAK-242 or DMSO. Results are presented relative to the *MRC1* mRNA abundance of unstimulated cells. Data are means ± SEM of three independent experiments, each with a different donor.

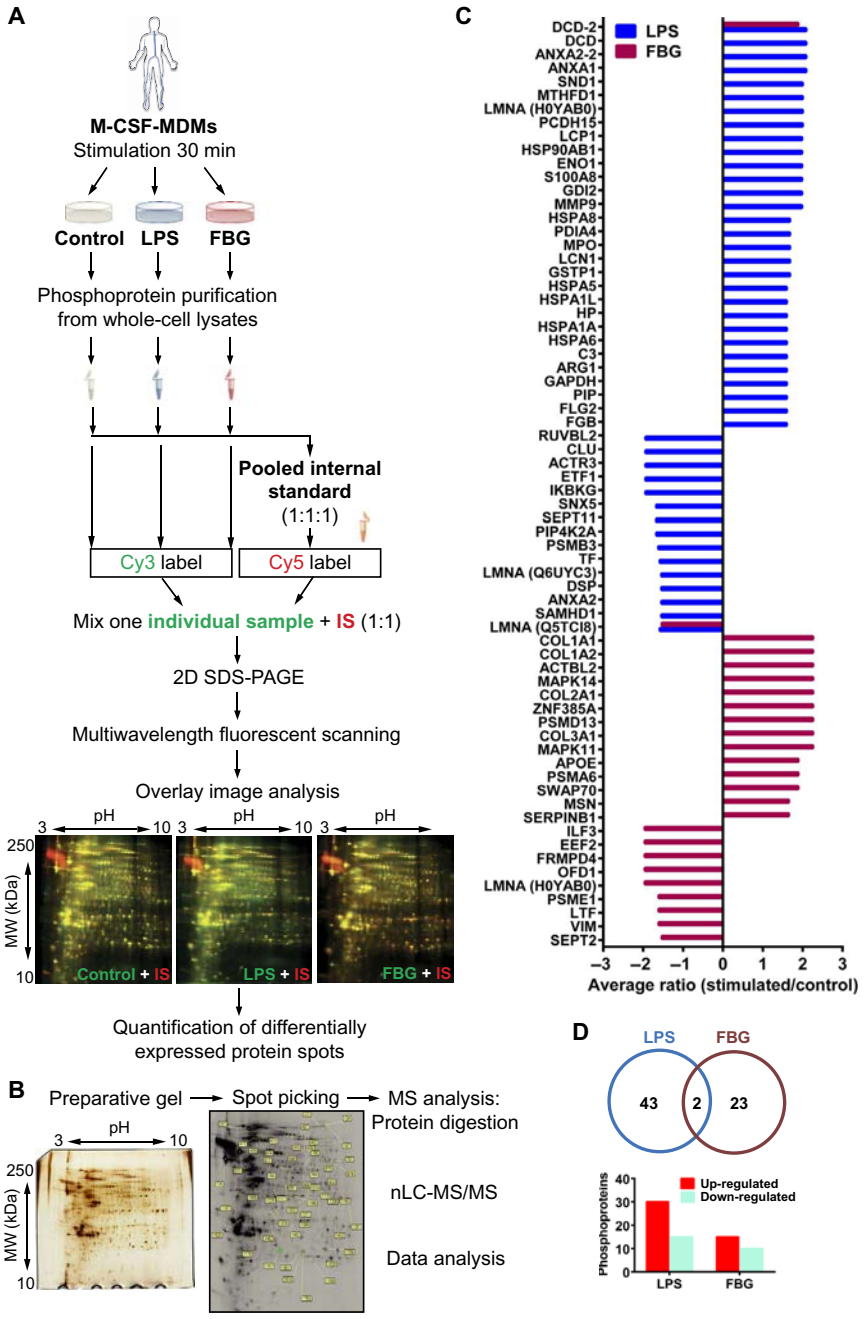

Fig. 2. Phosphoproteomic profiling of M-CSF-MDMs stimulated with LPS or FBG. (**A**) Workflow of phosphoprotein enrichment and analysis in human M-CSF-MDMs by IMAC and 2D-DIGE. Cells were left unstimulated or were stimulated with LPS (1 ng/ml) or 1 μM FBG for 30 min, and cell lysates were then subjected to IMAC to enrich phosphoproteins. Four different donors were used for each condition. Phosphoprotein-enriched fractions from individual samples and the internal standard (IS; a pool of equal amounts of each biological replicate) were labeled with CyDye DIGE Fluor Cy3 (green) and Cy5 (red) saturation dyes, respectively, which was followed by 2D-DIGE. 2D analytical gels were loaded with 5 μg of Cy3-labeled individual sample and 5 μg of Cy5-labeled IS. From each gel, two scanned images were generated at different wavelengths and overlaid. Differentially expressed protein spots were identified and quantified with DeCyder 2D Differential Analysis Software ($P < 0.05$, as determined by Student's *t* test; average ratio, ≥1.5). Representative 2D analytical gels (pH 3 to 10) from one donor. MW, molecular weight. (**B**) Workflow of protein identification from 2D-DIGE by MS analysis. Left: A preparative gel was loaded with 120 μg of total phosphoproteins [10 μg of each phosphoprotein-enriched fraction prepared from the lysates of cells treated as described in (A) and then subjected to silver staining]. This was matched to the analytical gel set with DeCyder 2D software to identify the differentially abundant protein spots that were determined by 2D-DIGE analysis. Right: The differentially abundant spots that were selected for automated spot picking before protein digestion, followed by nanoscale liquid chromatographic tandem mass spectrometry (nLC-MS/MS) analysis and Mascot database searching. (**C**) Phosphoproteins whose abundance was differentially regulated by LPS or FBG. Histogram shows increased and decreased abundance as an average ratio. This is the normalized ratio between LPS-stimulated cells and unstimulated cells and between FBG-stimulated cells and unstimulated cells. $n = 4$ independent donors per group. Phosphoproteins are shown with gene names. Data are from one experiment and are representative of four biological replicates. (**D**) Venn diagram displays phosphoproteins shared and specific to LPS- and FBG-stimulated M-CSF-MDMs. Histogram shows the numbers of phosphoproteins whose abundance was statistically significantly increased or decreased by LPS or FBG. Data are from one experiment and are representative of four biological replicates.

macrophage phenotype similar to that induced by LPS, we compared a combination of markers in LPS- and FBG-treated macrophages. We used human peripheral blood monocyte–derived macrophages cultured in macrophage colony-stimulating factor (M-CSF-MDMs) and examined macrophage markers that are increased in abundance by LPS or by alternative stimuli, such as interleukin-4 (IL-4) (*14*). Stimulation with either LPS (1 ng/ml) or 1 μM FBG domain induced comparable IL-6 secretion and *arginase-1* (*Arg1*) mRNA expression (Fig. 1A), whereas IL-23 and IL-12 secretion was induced only by LPS (Fig. 1B). At these concentrations of stimuli, FBG induced statistically significantly more IL-8 production (Fig. 1C) and less tumor necrosis factor–α (TNF-α) and IL-10 production (Fig. 1D) than did LPS. Finally, 1 μM FBG sustained the expression of the gene encoding mannose receptor, C type 1 (MRC1), whereas LPS (1 ng/ml) inhibited *MRC1* mRNA synthesis by 24 hours (Fig. 1E).

To rule out any contribution of contaminating LPS in FBG-stimulated macrophages, we pretreated FBG with polymyxin B, which neutralized

LPS-induced cytokine synthesis but not that induced by FBG (fig. S1A). To ensure that differences in cell surface marker abundance were not due to the loss of viable cells upon stimulation, we assessed cytotoxicity with an MTT assay and found that neither LPS nor FBG had any effect on cell viability (fig. S1B). Finally, to confirm that the analyzed markers were directly increased in abundance in response to TLR4 activation, we stimulated macrophages with FBG or LPS in the presence or absence of an antibody that blocks TLR4 function or of TAK-242, an inhibitor of TLR4 signal transduction. Both TLR4 inhibitors effectively abrogated LPS- and FBG-induced cytokine synthesis (Fig. 1F) and reestablished basal *MRC1* expression (Fig. 1G). Together, these results suggest that macrophages recognize FBG and LPS through TLR4 and, in response, change their activation state toward alternatively [M(IL-4)] and classically [M(LPS)] (*14*) activated phenotypes, respectively.

LPS and the FBG domain of tenascin-C generate distinct macrophage phosphoproteomic signatures

To further examine differences between LPS- and FBG-activated macrophages, we assessed protein phosphorylation as readout of signal transduction in response to cell stimulation. Fluorescent two-dimensional difference gel electrophoresis (2D-DIGE) followed by mass spectrometry (MS) analysis was used to enable an unbiased and quantitative analysis of the global macrophage phosphoproteome (Fig. 2, A and B) (*15*). Macrophages were left unstimulated or were stimulated with LPS or the FBG domain of tenascin-C, and then immobilized metal ion affinity chromatography (IMAC) was used to enrich phosphorylated proteins from macrophage lysates. Yields of enriched phosphoprotein were quantified (fig. S2A), and the efficiency of phosphoprotein enrichment was verified (fig. S2, B to D). Phosphoproteins from control and LPS- and FBG-treated cells were each labeled with the fluorescent dye Cy3, whereas an internal standard, containing a mixture of equal amounts of each experimental protein sample, was labeled with Cy5. Paired samples were separated by 2D polyacrylamide gel electrophoresis (2D-PAGE). Gels were subjected to multiwavelength fluorescent scanning to identify spots with at least 1.5-fold differences in intensity ($P \leq 0.05$) compared to the internal standard, and these spots were excised from a preparative gel for MS analysis. Sixty-eight phosphoproteins that were differentially regulated in abundance by stimulation with LPS or FBG compared to control cells were identified. LPS and FBG led to the differential regulation of 43 and 23 phosphoproteins, respectively, compared to control. Only two phosphoproteins, dermcidin isoform 2 (DCD-2) and prelamin-A/C (LMNA isoform Q5TCI8), were identified as being regulated by both stimuli (Fig. 2, C and D).

A number of proteins were selected for validation by Western blotting analysis of phosphoprotein fractions from control and LPS- and FBG-stimulated cells. These data confirmed the changes in abundance revealed by 2D-DIGE for proteasome subunit α6 (PSMA6), proteasome activator subunit 1 (PSME1), DCD, and type 1 collagen (COL1), as well as α-tubulin, which was included as a control because its abundance was not regulated by any stimulus (fig. S2E). Whereas Western blotting analysis confirmed the FBG-dependent increase in p38α [mitogen-activated protein kinase 14 (MAPK14)] phosphorylation that was observed by 2D-DIGE, it also showed that LPS stimulated the phosphorylation of p38α (fig. S2E). This signaling event was not identified in the proteomic screen but would be expected to occur based on what is known about the activation of TLR4 by LPS. Together, these data indicated that we could use the 2D-DIGE approach to identify subsets of signaling molecules activated by macrophages in response to different stimuli but do highlight that this technique will not yield an exhaustive list of all activated molecules. These data also emphasize the importance of independent validation to confirm data from this type of analysis, particularly when using primary human cells.

LPS- and FBG-stimulated protein phosphorylation drives divergent signaling pathways

To obtain insight into the types of proteins and the biological pathways in macrophages that were identified by 2D-DIGE as being regulated by LPS or FBG, we performed a number of in silico analyses. Gene ontology (GO) analysis examines the cellular location of regulated phosphoproteins, their class identity based on function and cellular compartment, and the biological systems to which they contribute. These data revealed that most of the macrophage phosphoproteins regulated by stimulation with LPS were intracellular, as expected (*16*), whereas there was an overrepresentation of extracellular phosphoproteins enriched from cells treated with FBG (fig. S3A). Chaperone, defense and immunity, and calcium-binding proteins were among the most highly populated classes of LPS-regulated phosphoproteins (fig. S3B). Accordingly, metabolic and immunological processes were well represented among the pathways associated with LPS-regulated phosphoproteins (fig. S3C). These observations are consistent with previous studies that investigated LPS-regulated protein phosphorylation in macrophages (*16*, *17*). FBG-stimulated cells had distinct enriched protein classes, including extracellular matrix proteins, kinases, nucleic acid–binding proteins, receptor transporters, and surfactants, which were not observed in LPS-treated cells, and FBG-regulated phosphoproteins were also associated with distinct biological processes, such as apoptosis (fig. S3, B and C). However, LPS and FBG led to the enrichment of many common biological processes (for example, immune system processes, cellular processes, and cellular component organization) and protein classes (for example, defense and immunity proteins, cytoskeletal proteins, transcription factors, enzyme modulators, transfer or carrier proteins, and proteases), indicating overlap in the biological outcomes that occur after the activation of macrophage TLR4 by each stimulus.

Next, we used the STRING (Search Tool for the Retrieval of Interacting Genes) database of known and predicted protein-protein interactions to identify specific pathways targeted by the phosphorylation events induced by LPS or FBG and to better understand the molecular organization and the relationships among these phosphoproteins. We first identified the top 15 statistically significantly enriched pathways downstream of LPS and FBG (Fig. 3, A and B). We next identified LPS-activated pathways that would be expected based on published data. These include MAPK signaling pathways (*16*, *17*); endocytosis (*16*); immune signaling pathways, such as antigen processing and presentation (*18*), as well as complement (*19*) and coagulation (*20*) cascades; and infection-related pathways (for example, influenza A and Epstein-Barr virus infection), which corroborate a role for TLR4 signaling in response to viral infection (*21*). We also found representation of signaling pathways that substantiate emerging observations linking TLR signaling with endoplasmic reticulum activity in macrophages (*22*), estrogen signaling (*23*), spliceosome (*24*), thyroid hormone synthesis (*25*), and the biosynthesis of amino acids (*26*) (Fig. 3A). In contrast, distinct signaling pathways emerged from the analysis of FBG-stimulated cells. Consistent with the published literature, we observed enrichment for platelet activation (*27*), extracellular matrix–receptor interactions (*28*), focal adhesions (*28*, *29*), leukocyte migration (*30*), phosphatidylinositol 3-kinase (PI3K)–Akt signaling (*31*), and vascular endothelial growth factor (VEGF) signaling (*32*) pathways. However, we also found distinct signaling pathways in immune defense, including amoebiasis, Epstein-Barr virus infection, NOD-like receptor signaling, shigellosis, and epithelial cell signaling in *Helicobacter pylori* infection. Furthermore, this analysis showed that FBG stimulation led to the phosphorylation of proteins associated with the proteasome.

We then analyzed the protein-protein interaction networks composed of phosphoproteins that were increased in abundance in response to LPS (1 ng/ml) and FBG (1 μM) (Fig. 3, C and D). We noted that 69% of LPS-responsive and 73% of FBG-responsive phosphoproteins were directly interconnected with each other in the STRING network. This high degree of connectivity

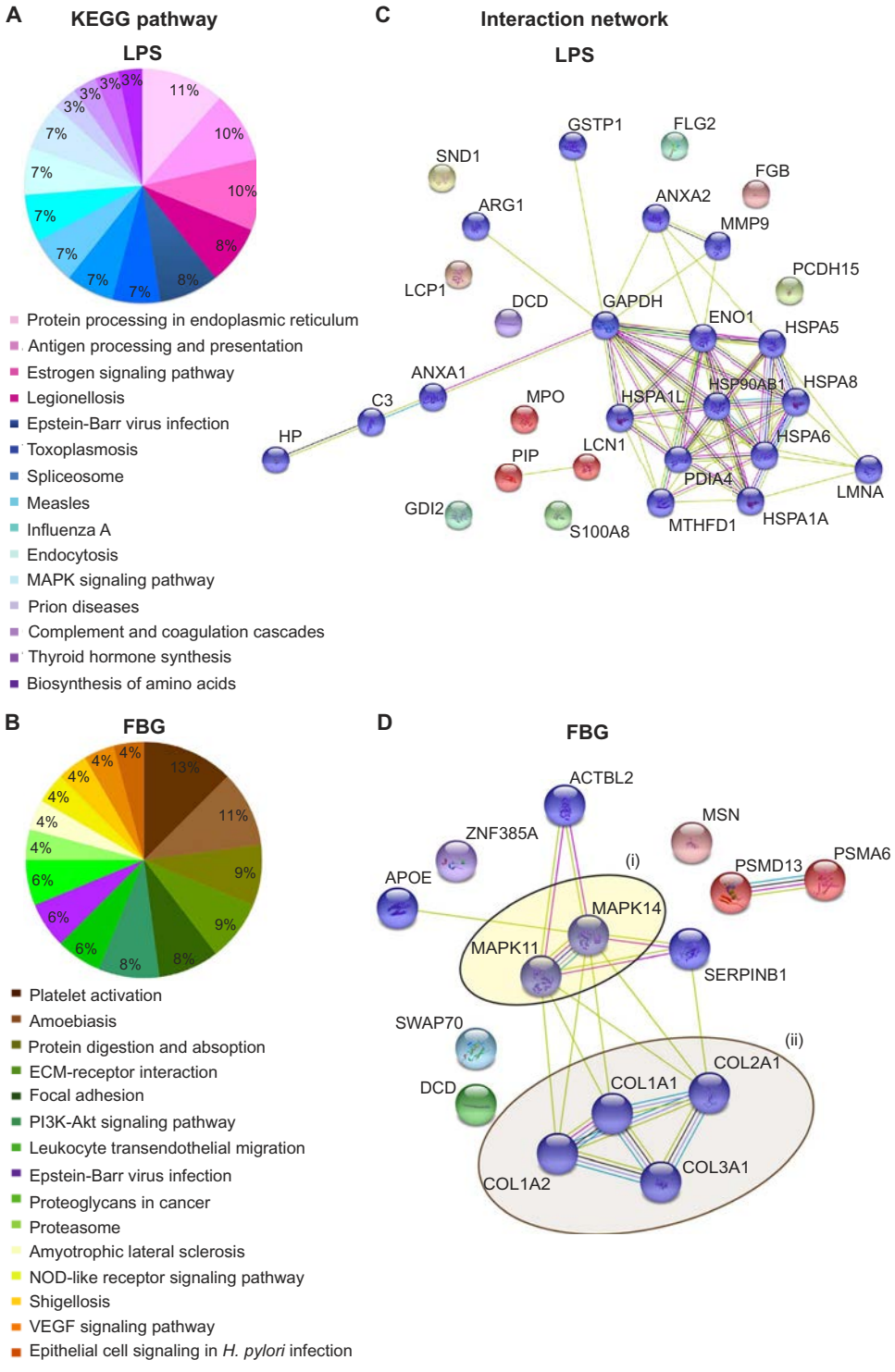

Fig. 3. Regulated pathways and protein networks in LPS-stimulated versus FBG-stimulated M-CSF-MDMs. (A and B) Pathway analysis of phosphoproteins whose abundance in M-CSF-MDMs was statistically significantly increased by stimulation for 30 min with LPS (A) or the FBG domain of tenascin-C (B). Pie charts show the top 15 statistically significantly enriched KEGG pathways ($P < 0.05$) among the regulated phosphoproteins after LPS or FBG stimulation compared to those of unstimulated cells. For each KEGG pathway, pie chart slices show the percentage of gene hits against the total number of genes. KEGG pathway enrichment was performed with STRING, and the background data set for the analysis was the *Homo sapiens* genome. ECM, extracellular matrix. (C and D) Interaction networks of phosphoproteins whose abundance in M-CSF-MDMs was statistically significantly increased by stimulation for 30 min with LPS (C) or FBG (D). The networks were constructed with STRING. Nodes (circles) represent phosphoproteins regulated by LPS (C) and FBG (D) and are labeled with gene names. Both connected and disconnected nodes are shown. Nodes were clustered and colored with the Markov Cluster algorithm according to their distance matrix. Edges (lines) indicate known and predicted protein-protein interactions and are drawn with differently colored lines according to the type of evidence: neighborhood (green), co-occurrence (dark blue), experimental (purple), text-mining (olive green), database (blue), homology (light blue), and coexpression (black). Ovals highlight proteins that belong to enriched KEGG pathways that were investigated here. Proteins in group (i) belong to the platelet activation, leukocyte transendothelial migration, Epstein-Barr virus infection, proteoglycans in cancer, amyotrophic lateral sclerosis, NOD-like receptor signaling, shigellosis, VEGF signaling, and epithelial cell signaling in *H. pylori* infection pathways. Proteins in group (ii) belong to the platelet activation, amoebiasis, protein digestion and absorption, extracellular matrix–receptor interaction, focal adhesion, and PI3K-Akt signaling pathways.

suggests that LPS and FBG regulate components of functional pathways or protein complexes, rather than cause random protein phosphorylation events in macrophages. Furthermore, upon FBG stimulation of macrophages, this analysis predicted that MAPK11 (p38β) and MAPK14 (p38α or p38 MAPK) would act as central kinases and that collagen types I, II, and III would act as preponderant extracellular matrix molecules (Fig. 3D).

Together, these bioinformatics data highlight the biological outcomes that were common in response to LPS and the FBG domain of tenascin-C, but also reveal differences in the macrophage response to these distinct microenvironmental stimuli. However, although GO, KEGG (Kyoto Encyclopedia of Genes and Genomes) pathway, and protein interaction network analyses help to explore experimental data sets and provide testable hypotheses,

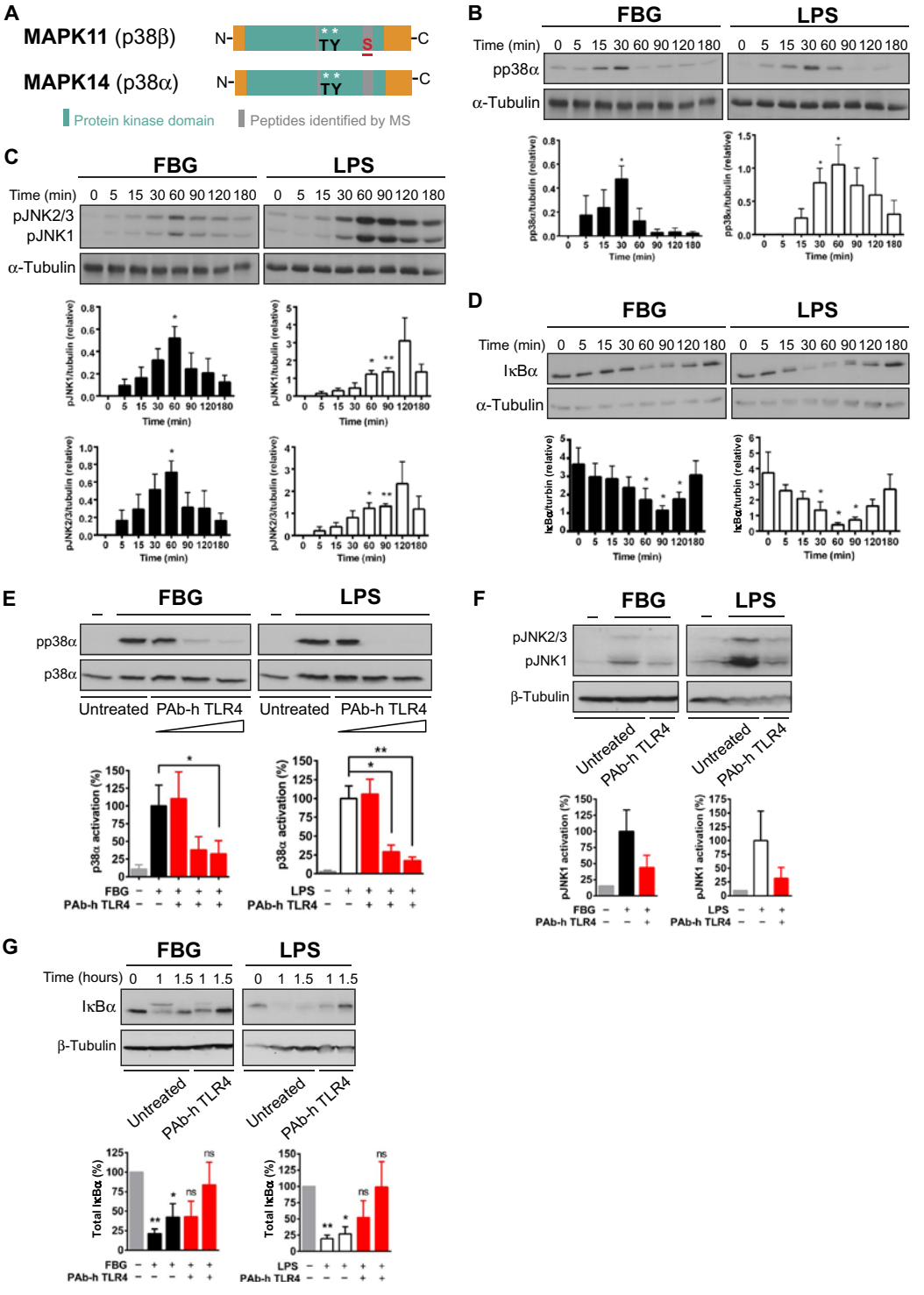

Fig. 4. The FBG domain of tenascin-C and LPS stimulate p38α, JNK, and NF-κB signaling through TLR4. (**A**) Schematic representation of MAPK11 (p38β) and MAPK14 (p38α). The protein kinase domain is shown in green, and the flanking N- and C-terminal regions are in orange. Peptide sequences that were found by MS analysis are in gray. Starred black letters indicate published phosphorylation sites, whereas underlined red letters indicate the phosphorylation site identified in this study (Ser^{272}). (**B** to **D**) Top: M-CSF-MDMs were treated for the indicated times with 1 μM FBG or LPS (1 ng/ml), and cell lysates were then subjected to Western blotting analysis with antibodies specific for pp38α (B), phosphorylated JNK1 (pJNK1) and pJNK2/3 (C), IκBα (D), and α-tubulin (B to D). Blots are representative of four independent experiments, each with a different donor. Bottom: Histograms show quantification of the abundances of pp38α (B), pJNK1 and pJNK2/3 (C), and IκBα (D) normalized to that of α-tubulin by densitometric analysis. Data are means ± SEM of four experiments. $^{*}P < 0.05$, $^{**}P < 0.01$ compared to the 0-min time point by one-way ANOVA. (**E** to **G**) Top: M-CSF-MDMs were treated for 30 min (E), 1 hour (F), or 1 and 1.5 hours (G) with 1 μM FBG or LPS (1 ng/ml) in the presence or absence of pAb-h TLR4 at dosages 1, 10, or 25 μg/ml (E) or 25 μg/ml (F and G). Cell lysates were then analyzed by Western blotting with antibodies specific for pp38α and total p38α (E), pJNK2/3 and pJNK1 (F), IκBα (G), and β-tubulin (F and G). Blots are representative of three or four independent experiments, each with a different donor. Bottom: Histograms show quantification of the abundances of pp38α (E), pJNK1 (F), and IκBα (G) normalized to the abundances of total p38 (E) and β-tubulin (F and G) by densitometric analysis. Data are expressed as a percentage of the abundance of the indicated proteins in cells stimulated in the absence of pAb-h TLR4. Data are means ± SEM of three or four independent experiments, each with a different donor. $^{*}P < 0.05$, $^{**}P < 0.01$. ns, not significant by one-way ANOVA.

independent experimental validation is required to draw any conclusions. We chose two pathways to investigate further. The first was the MAPK signaling pathway, given that FBG-mediated phosphorylation of p38 kinases has not yet been investigated in macrophages, whereas the second was the phosphorylation of collagen molecules, given that this was particular to stimulation by FBG and, to our knowledge, has not been reported in macrophages.

Both LPS and the FBG domain of tenascin-C stimulate p38, c-Jun N-terminal kinase, and nuclear factor κB signaling through TLR4 activation

LPS-mediated activation of TLR4 stimulates the phosphorylation (and activation) of the MAPKs p38 and c-Jun N-terminal kinase (JNK) and the activation of nuclear factor κB (NF-κB)–dependent gene transcription. Phosphorylation of p38α and p38β emerged as a key event after the activation of macrophages of FBG (Fig. 4A and fig. S4A); however, little is known about MAPK signaling downstream of this TLR4 stimulus.

Western blotting analysis of phosphoprotein-enriched and unphosphorylated protein fractions from FBG-stimulated macrophages with an antibody specific for phosphorylated p38α (pp38α; Thr^{180}/Tyr^{182}) confirmed

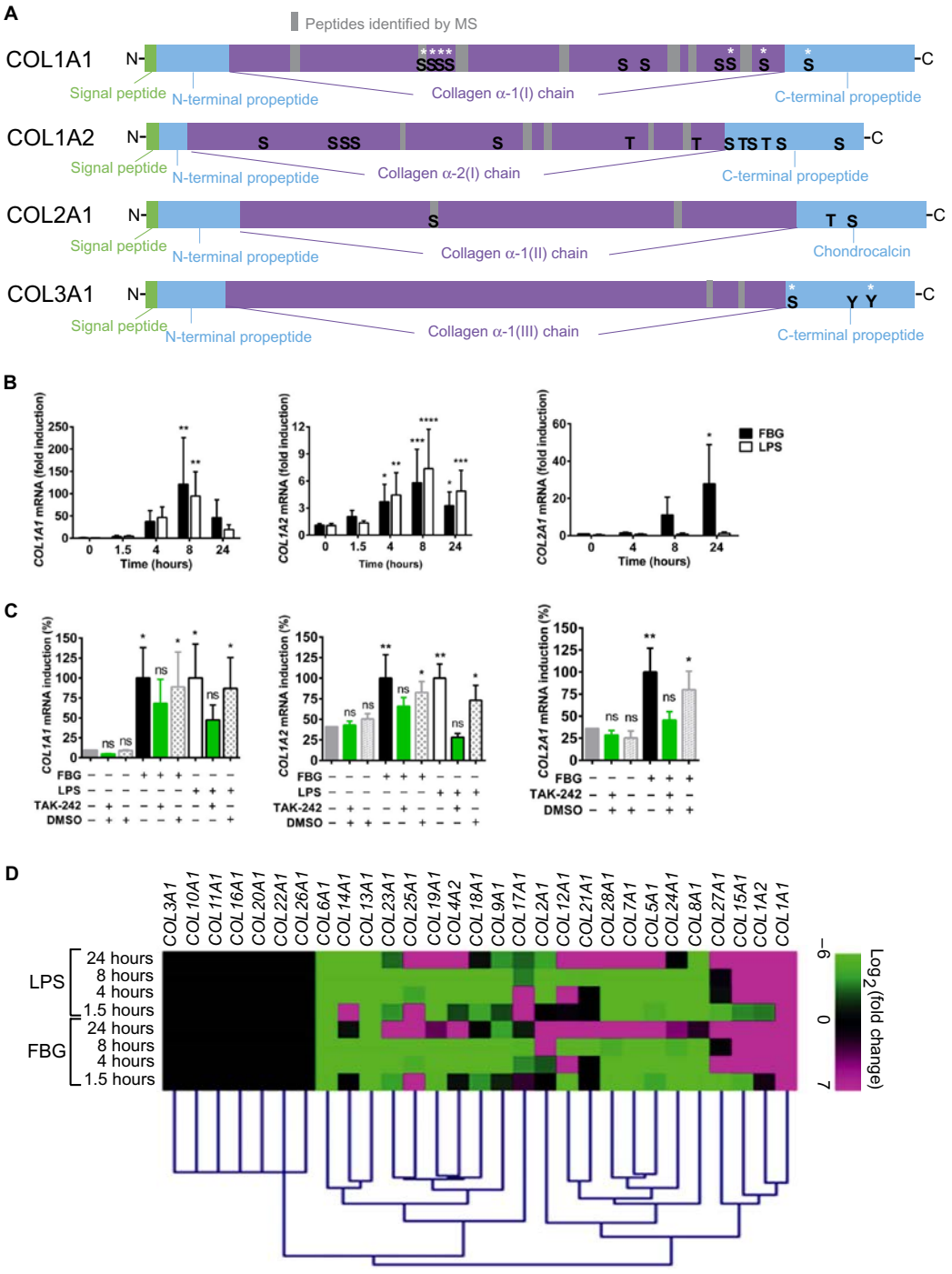

Fig. 5. Analysis of the collagen network in FBG- and LPS-activated M-CSF-MDMs. (**A**) Schematic representation of COL1A1, COL1A2, COL2A1, and COL3A1. Green, signal peptide sequences; blue, N- and C-terminal propeptide sequences; purple, collagen chain sequences; gray, peptide sequences that were found by MS analysis. Letters indicate unpublished phosphorylation sites experimentally observed by Cell Signaling Technology [PhosphoSitePlus (www.phosphosite.org/homeAction.do)], and starred letters indicate published phosphorylation sites. (**B**) M-CSF-MDMs were stimulated for the indicated times with 1 μM FBG or LPS (1 ng/ml) and then were subjected to RT-qPCR analysis of the abundances of *COL1A1*, *COL1A2*, and *COL2A1* mRNAs, which are expressed relative to their abundances in unstimulated cells. Data are means ± SEM of three to five independent experiments, each with a different donor. $*P < 0.05$, $**P < 0.01$, $***P < 0.001$, $****P < 0.0001$ by two-way ANOVA. (**C**) RT-qPCR analysis of *COL1A1*, *COL1A2*, and *COL2A1* mRNAs in M-CSF-MDMs stimulated with FBG or LPS for 8 (*COL1A1* and *COL1A2*) or 24 hours (*COL2A1*) in the presence or absence of 3 μM TAK-242 or DMSO control. Data are means ± SEM of four or five independent experiments, each with a different donor, and are presented as the percentage increase in mRNA abundance relative to that in cells stimulated in the absence of TAK-242 or DMSO. $*P < 0.05$, $**P < 0.01$ by one-way ANOVA when comparing stimulated to unstimulated cells. (**D**) RT-qPCR analysis of the abundances of the indicated collagen-encoding mRNAs in M-CSF-MDMs stimulated with FBG or LPS for the indicated times. The heat map shows suppression (green) and induction (magenta) of expression as fold change in mRNA abundance on a $\log_2$ scale relative to that in unstimulated cells. Connecting lines represent hierarchical clustering of the patterns of variation in expression of collagen-encoding genes. Data are from three independent experiments, each with a different donor.

the activation of p38α by FBG (figs. S2E and S4B). We next compared the LPS- and FBG-stimulated phosphorylation of p38α over time in experiments with macrophage donors, independent of those used in the phosphoproteomic screen. Western blotting analysis of macrophage lysates for phosphoproteins revealed that both FBG and LPS stimulated p38α phosphorylation. Whereas p38α phosphorylation induced by FBG appeared to be more transient (maximal by 30 min in macrophages from all donors), that induced by LPS was sustained for longer times (Fig. 4B). FBG increased the extent of intracellular staining of pp38α (fig. S4C) and also stimulated the phosphorylation of MAPK kinase kinase 3 (MKK3) and MKK6, specific upstream kinases that are necessary for p38α activation (fig. S4D). Stimulation of cells with FBG or LPS also induced JNK phosphorylation; however, the magnitude of activation of JNK1 and JNK2/3 was greater in cells treated with LPS than in cells treated with FBG (Fig. 4C). In addition, FBG stimulated the degradation of a substantial amount of inhibitor of NF-κB α (IκBα), with maximal degradation at 90 min (30 min later than in the case of LPS) (Fig. 4D); however, it activated an NF-κB–driven reporter gene overexpressed in monocytic cell lines to a similar extent and with similar kinetics to that of LPS (fig. S4E). FBG-dependent MAPK and NF-κB activities were inhibited by the TLR4 function–blocking antibody (Fig. 4, E to G, and fig. S4F). These results suggest that, similarly to LPS, the FBG domain of tenascin-C stimulates the p38, JNK, and NF-κB pathways through the activation of TLR4.

The FBG domain of tenascin-C stimulates macrophages to synthesize and phosphorylate collagen

Among the phosphoproteins that increased the most in abundance in FBG-activated macrophages were collagen types I (*COL1A1* and *COL1A2*), II (*COL2A1*), and III (*COL3A1*). These molecules were not phosphorylated in either unstimulated or LPS-stimulated macrophages (Figs. 2B and 3D). We confirmed these data by subjecting phosphoprotein-enriched cellular fractions to Western blotting analysis with a collagen type I–specific antibody (fig. S2G). Although collagen phosphorylation was reported previously (*33*–*38*) [Cell Signaling Technology curation sets (www.PhosphoSitePlus.org)] (Fig. 5A), the effect of collagen phosphorylation on its structure and function is unclear, and the biosynthesis of these large fibrillar extracellular matrix molecules by macrophages is not well characterized.

We examined whether the changes in the abundances of the collagens observed in our phosphoproteomic screen were regulated at the mRNA level after macrophage activation with LPS (1 ng/ml) or 1 μM FBG. *COL1A1* and *COL1A2* mRNA abundances in macrophages were similar in response to either LPS or FBG. In contrast, *COL2A1* mRNA was increased in abundance by FBG, but not by LPS, whereas *COL3A1* mRNA was undetectable (Fig. 5B). This stimulus-specific collagen production by macrophages was mediated through activation of TLR4 because the synthesis of *COL1A1, COL1A2*, and *COL2A1* mRNAs was prevented by TAK-242 (Fig. 5C). We extended this analysis to examine the expression of the genes encoding each of the 28 types of collagen in macrophages upon stimulation with LPS or FBG and compared the abundance of each collagen mRNA in macrophages with that in primary human dermal fibroblasts (DFs), one of the most prolific cellular sources of collagen. *COL10A1*, *COL11A1*, *COL16A1,* and *COL26A1* mRNAs were detected only in DFs, whereas *COL20A1* and *COL22A1* were not detected in either macrophages or DFs. With the exception of *COL17A1* mRNA, which was equally abundant in DFs and macrophages, and *COL23A1*, which was more abundant in macrophages than in DFs, macrophages had reduced amounts of collagen mRNAs compared to those in DFs, as expected (Fig. 5D and fig. S5E). The expression of *COL4A2*, *COL6A1*, *COL9A1*, *COL13A1*, *COL17A1*, *COL18A1*, *COL25A1,* and *COL27A1* in macrophages was regulated to a similar extent by both LPS and FBG. Compared to LPS, FBG was a stronger inducer of *COL8A1* expression, which is increased upon injury (*39*), and of *COL23A1* and *COL24A1*, which are found in cancer (*40*, *41*), conditions in which tenascin-C plays an established role (*42*). In contrast to FBG, LPS induced increased expression of fibril-associated collagens with interrupted triple helices (FACITs), namely, *COL7A1*, *COL12A1*, *COL15A1*, *COL19A1*, and *COL21A1*, as well as the collagenase-resistant *COL5A1* and the collagen-containing von Willebrand factor *COL28A1* (Fig. 5D and fig. S5F). Together, these data show that macrophages can substantially contribute to collagen synthesis and that pathogenic stimuli drive the synthesis of FACIT collagens that maintain the integrity of the extracellular matrix, whereas matrix-derived cues instruct macrophages to synthesize *COL2A1* and phosphorylate collagens.

LPS, but not FBG, stimulates the synthesis of macrophage collagenases

To determine whether the degradation, as well as the synthesis, of collagen by macrophages was differentially affected by the FBG domain of tenascin-C and LPS, we investigated key matrix metalloproteinases (MMPs), including MMP1 (also known as interstitial collagenase), MMP13 (also known as collagenase 3), and MMP14, a type I transmembrane MMP that breaks down collagen, gelatin, and other matrix molecules. MMP1 abundance was statistically significantly and rapidly increased in response to LPS (1 ng/ml), whereas FBG (1 μM) resulted in a modest increase in MMP1 abundance at later time points. At this concentration, FBG did not stimulate MMP13 synthesis, which was in contrast to LPS, which promptly and transiently increased MMP13 abundance. Furthermore, MMP14 synthesis was induced 24 hours after stimulation with FBG, but not LPS (Fig. 6A). This stimulus-specific MMP profile was mediated through the activation of TLR4 because the synthesis of each enzyme was completely abrogated by TAK-242 (Fig. 6B).

MMP activity is highly regulated at several levels. To determine whether the distinct expression of MMPs induced by the two TLR4 ligands resulted in functional differences, we tested the collagenolytic and gelatinolytic activities of LPS- and FBG-activated macrophages. LPS-activated macrophages efficiently degraded collagen, an activity that was reversed by the broad-spectrum MMP inhibitor GM6001, whereas FBG-activated cells showed little collagenolytic activity (Fig. 6C). These results are consistent with the collagenase expression profiles of each stimulus (*MMP1* mRNA and protein in Fig. 6A and fig. S6; *MMP13* mRNA in Fig. 6A). Macrophages constitutively degraded gelatin and continued to do so upon stimulation with FBG. Conversely, LPS-activated macrophages were unable to degrade gelatin (Fig. 6D, upper three panels). The gelatinolytic activity of macrophages did not match the changes in *MMP14* mRNA abundance (Fig. 6A), but did correlate with the cell surface abundance of MMP14 protein, which was low to undetectable in LPS-activated macrophages but largely unaltered in FBG-activated cells (Fig. 6D, lower panel), suggesting some degree of posttranscriptional regulation of MMP14 activity. Together, these data indicate that LPS, but not the FBG domain of tenascin-C, enables macrophages to degrade collagen but prevents them from degrading gelatin, thus affecting their substrate specificity.

DISCUSSION

Detection of both pathogen invasion and sterile tissue damage by the same PRRs has been recognized for over a decade; however, the specificity of the inflammatory outcomes downstream of infection and injury remains poorly understood. This study directly compared the molecular signatures induced in primary human macrophages through activation of the same TLR by distinct microenvironmental stimuli. We showed that the proinflammatory, extracellular matrix glycoprotein tenascin-C and microbial LPS activated a common set of signaling pathways, including NF-κB and

MAPK, but these stimuli also induced different signaling pathways downstream of TLR4. Although both stimuli resulted in cytokine synthesis, they differed in the cytokines that were produced. Moreover, the FBG domain of tenascin-C promoted a macrophage phenotype that exhibited matrix molecule synthesis and phosphorylation, whereas LPS promoted a macrophage phenotype characterized by an enhanced capacity to degrade matrix.

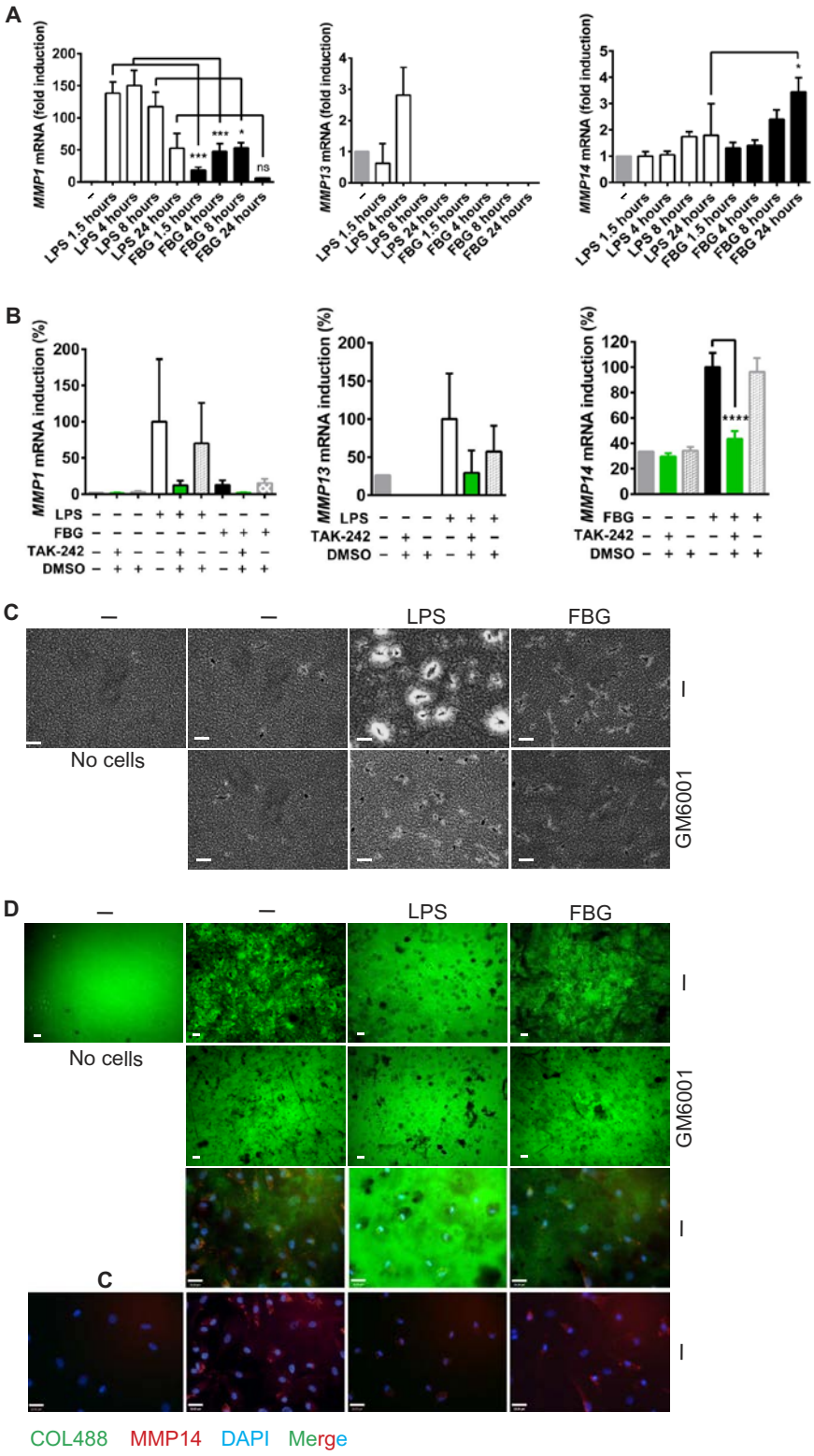

Fig. 6. MMP mRNA expression and matrix degradation by FBG- and LPS-activated M-CSF-MDMs. (**A**) RT-qPCR analysis of *MMP1*, *MMP13*, and *MMP14* mRNA abundances in M-CSF-MDMs stimulated with LPS (1 ng/ml) or 1 μM FBG for the indicated times and expressed as a percentage of the mRNA abundances of unstimulated cells. Data are means ± SEM of four or five independent experiments, each with a different donor. $^{*}P < 0.05$, $^{***}P < 0.001$ by one-way ANOVA. (**B**) RT-qPCR analysis of *MMP1*, *MMP13*, and *MMP14* mRNA abundances in M-CSF-MDMs stimulated with LPS or FBG for 4 (*MMP13*) or 24 hours (*MMP1* and *MMP14*) in the presence or absence of 3 μM TAK-242 or DMSO. Data are presented as the percentage change in mRNA abundance relative to that in cells stimulated with LPS or FBG in absence of TAK-242. Data are means ± SEM of three or four independent experiments, each with a different donor. $^{****}P < 0.0001$ by one-way ANOVA. (**C**) Collagen film degradation by M-CSF-MDMs stimulated with or without (–) LPS or FBG in the presence or absence of 10 μM GM6001 for 5 days. Digested areas of collagen are shown as white regions against a gray collagen background. Images are representative of three independent experiments, each with cells from a different donor. (**D**) Top two rows: Fluorescent gelatin film degradation by M-CSF-MDMs stimulated with or without (–) LPS or FBG in the presence or absence of 10 μM GM6001 for 64 hours. Digested areas of gelatin are shown as black regions against a green gelatin background. Bottom row: Cell surface MMP14 and DAPI (4′,6-diamidino-2-phenylindole) immunofluorescence staining are shown in red and blue, respectively. In this panel, "C" denotes cells stained in the absence of primary antibody. Third row: merged views of gelatin degradation and MMP14 immunofluorescence. Images are representative of three independent experiments, each with cells from a different donor. Scale bar, 18.00 μm.

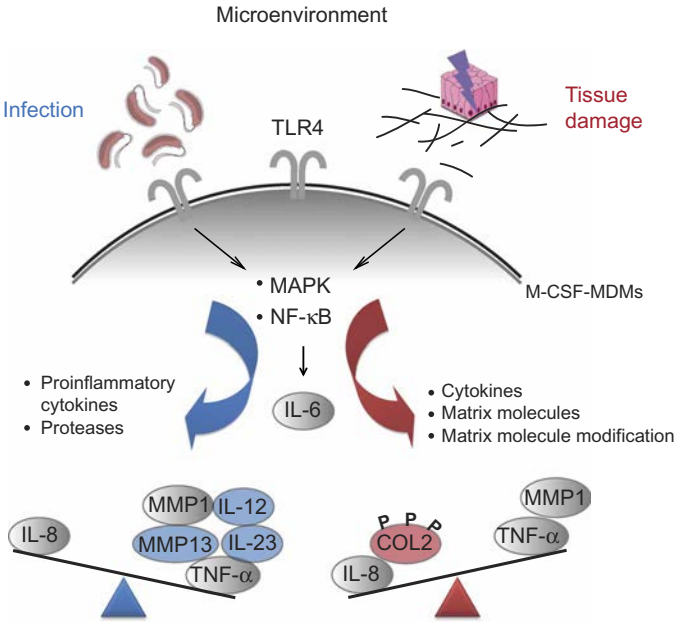

Fig. 7. Model of the microenvironmental influence on TLR4-mediated innate immune responses in macrophages. TLR4 is exposed to and activated by ligands from distinct microenvironments, including infected as well as sterile, but damaged, tissues. Both stimuli equally lead to activation of the NF-κB and MAPK signaling pathways and secretion of IL-6. However, whereas infection results in macrophages producing large amounts of proinflammatory cytokines and tissue-degrading enzymes, tissue damage promotes the synthesis and posttranslational modification of matrix molecules in addition to contributing to cytokine synthesis. Molecules whose production is stimulated exclusively by pathogens or tissue damage are shown in blue or red, respectively; those induced by both stimuli are shown in gray. P, phosphorylation.

Together, these data illustrate how the activation of TLR4 by ligands from endogenous (host-derived) and exogenous (microbe-derived) sources generates different macrophage phenotypes (Fig. 7).

Using a combination of markers of activation, we found two distinct activation phenotypes for macrophages that were exposed to either the FBG domain of tenascin-C or LPS. These data indicated that tenascin-C shifted the macrophage activation phenotype toward that induced by IL-4. Although FBG was unable to induce IL-12 or IL-23 production and induced less TNF-α production than did LPS, it sustained the expression of *MRC1*. The genes encoding IL-6 and Arg1, which are expressed throughout macrophage activation, were equally induced by both stimuli (*14*). However, although there was some overlap in the phenotypes generated by both stimuli, tenascin-C generated a type of macrophage that, in contrast to IL-4–stimulated macrophages, resulted in less IL-10 production than occurred in response to LPS. These data exemplify the diverse nature of macrophage subsets, revealing how the microenvironment is key to fine-tuning their phenotypes.

By combining phosphoprotein enrichment with 2D-DIGE and MS analysis, we captured a snapshot of tenascin-C– and LPS-induced changes in the macrophage phosphoproteome that reflected the first 30 min of receptor activation. We also used multiple bioinformatics tools to explore the experimental data set. Although there are a few phosphoproteomic analyses of the responses of different TLRs to pathogenic ligands (*16*, *17*), here, we compared the phosphoprotein signatures in response to stimulation of a specific TLR by exogenous and endogenous ligands. Overall, this analysis revealed two distinct yet overlapping phosphoproteomes. Consistent with this finding, Western blotting analysis confirmed that, whereas tenascin-C, and not LPS, stimulated PSMA6 phosphorylation and PSME1 dephosphorylation, both tenascin-C and LPS stimulated DCD phosphorylation. Bioinformatics analysis identified most of the LPS-dependent phosphoproteins as being intracellular and most of the tenascin-C–dependent proteins as being extracellular. The latter consisted of several extracellular matrix molecules, including COL1, which we validated by Western blotting, suggesting a role for the tenascin-C–mediated activation of TLR4 in changing the macrophage microenvironment. Along these lines, the KEGG pathway analysis and protein-protein interaction networks highlighted both differences and similarities among LPS- and tenascin-C–regulated phosphoproteins. On one hand, tenascin-C resulted in the enrichment of pathways that underlie an interplay between the cells and the microenvironment, including extracellular matrix–receptor interactions, focal adhesions, and leukocyte migration. Consistent with this, strong connectivity between matrix molecules emerged from the tenascin-C–dependent phosphoprotein interaction network. On the other hand, we observed an overlap in the innate immunity– and infection-related pathways that were activated by both stimuli.

As with other TLR phosphoproteomic studies (*16*, *17*, *36*), our study did not identify all of the phosphoproteins that belong to the TLR pathway, indicating that the screen does not completely recapitulate the complex effect of TLR activation in macrophages. Observational proteomic data sets are incomplete by nature because of either limited coverage of the regulated phosphoproteome or the possibility that not all pathway components are regulated by phosphorylation or have already been dephosphorylated or degraded at the time point chosen. However, the following findings strengthen the validity of our experimental data. First, we identified several phosphoproteins that are classically linked to the TLR pathway, including NF-κB [that is, NF-κB essential modulator (*43*) and clusterin (*44*)] and MAPK (that is, MAPK14 and MAPK11). Second, we detected the phosphorylation of cytoskeletal and actin-binding proteins, such as plastin-2 (*45*), septin-2, septin-11 (*46*), and vimentin (*47*), which are essential for macrophage motility and phagocytosis, as previously reported for LPS (*16*, *17*). Third, we identified pathways that are linked to tenascin-C function, such as VEGF signaling (*48*) and focal adhesions (*29*). Fourth, we found phosphoproteins that are implicated in TLR activity [for example, annexin A1, annexin A2 (*49*, *50*), and SWAP70 (*51*)] or are implicated in having a function for TLRs in glycolysis (*52*), such as α-enolase 1 and glyceraldehyde-3-phosphate dehydrogenase. Fifth, we identified kinases that are activated upon TLR4 activation, such as phosphatidylinositol-5-phosphate 4-kinase type 2α (*53*–*55*) and eukaryotic elongation factor 2 kinase (*56*). Finally, we showed the enrichment of endogenous danger signals whose expression is induced upon TLR4 activation and can themselves activate TLR4 if released (*57*), such as S100A8, fibrinogen (FGB), and several heat shock proteins, including HSP90AB1, HSPA8, HSPA5, HSPA1L, and HSPA1A.

Independent experiments to validate tenascin-C–regulated phosphoproteins and targeted Western blotting analyses confirmed the activation of p38α MAPK and revealed the activation of JNK and NF-κB signaling, pathways that were also activated by LPS. Moreover, MS analysis revealed that in addition to Thr^{180} and Tyr^{182} (residues of p38α that are phosphorylated in response to LPS), phosphorylation of the previously uncharacterized residue Ser^{272} was induced by FBG. This event may be FBG-specific and could account, at least in part, for the differences in FBG- and LPS-stimulated signaling. However, we could not validate the phosphorylation of Ser^{272} in cells because a phosphospecific antibody for this site was not available.

We found that stimulation of macrophages with tenascin-C (1 μM), but not LPS (1 ng/ml), resulted in the enrichment of phosphorylated collagen. These data suggest that tenascin-C activates the synthesis and post-translational modification of other matrix molecules by macrophages, and they place the production of phosphorylated collagen molecules in macrophages downstream of TLR signaling. Phosphorylation of extracellular matrix molecules, including collagen type I and secreted pro-α1(I) N-propeptide, by casein kinases was first reported more than 40 years ago (*58*, *59*). More recently, phosphorylation of collagen type XVII was shown to inhibit its shedding by TNF-α converting enzyme TACE (*34*), and phosphorylation of other extracellular molecules is implicated in the regulation of cell adhesion and susceptibility to proteolytic cleavage. Note that the ability of tenascin-C to regulate the phosphorylation of nonkinase proteins has been reported. Tenascin-C promotes autophosphorylation of platelet-derived growth factor receptor A, thereby enhancing its ability to cross-talk with $\alpha_V\beta_3$ integrin and, in turn, promoting the proliferation and migration of smooth muscle cells (*60*).

Hemocytes, the phagocytes of invertebrates, synthesize collagen type IV in the germline stem cell niche in *Drosophila* (*61*). In humans, a handful of studies have reported the synthesis of collagen molecules in macrophages and have suggested that these proteins may play a role in anchoring macrophages to the extracellular matrix and stabilizing atherosclerotic plaques in vivo (*62*–*64*). One study looked at collagen mRNA synthesis by monocytes and macrophages; however, it only reported whether expression was detected or not without providing any quantitative data (*64*). We therefore screened for the expression of all 28 collagen-encoding mRNAs, including those found by the proteomic study, in LPS- or tenascin-C–activated and unactivated macrophages and compared it to that of human DFs, which are established matrix producers. With the exception of collagen type XXIII, whose mRNA was more abundant in macrophages, the abundances of 21 of the 22 collagen-encoding mRNAs detected in macrophages were greater in fibroblasts as expected. Note, however, that expression of the gene encoding collagen type II was substantially induced by tenascin-C, but not LPS, through the activation of TLR4. This indicates that matrix-derived, but not pathogenic, microenvironmental cues can instruct macrophages to synthesize collagen type II and reveals different phenotypic signatures of macrophages activated by distinct stimuli that operate through the same receptor. This change in the cellular microenvironment may affect the interaction between the macrophage and the surrounding extracellular matrix, given that collagen type II interacts with integrins and proteoglycans (*65*, *66*). The increased production of collagen type II by macrophages in response to tenascin-C may be relevant in diseases, such as rheumatoid arthritis, in which, on one hand, tenascin-C abundance is increased and sustains inflammation through TLR4 (*11*) and, on the other hand, antibodies against native and citrullinated collagen type II are produced (*67*). In vivo, it is possible that the production and modification of collagen by tenascin-C–activated macrophages counterbalances the production of degradative enzymes by these cells. This is supported by our findings that, upon activation of TLR4 by LPS, macrophages produced more MMP1 than did those activated by the FBG domain and that, at these concentrations, only LPS-activated macrophages produced MMP13 and degraded collagen in vitro. Thus, whereas tenascin-C enables macrophages to shape the biochemistry of the matrix, LPS enables macrophages to degrade it.

A number of questions remain to be answered, foremost of which is why distinct gene expression profiles are generated by a matrix-derived microenvironmental cue and a pathogenic component, given that both activate NF-κB and MAPK signaling by stimulating TLR4. The answer may lie in the recruitment of distinct adaptor molecules early in the signaling cascade. This process may be regulated by receptor dimerization, which is essential for signaling by pathogenic components but may not be necessary for signaling by endogenous molecules. Alternatively, this process may be explained by the distinct co-receptor and accessory molecule requirements for pathogenic and endogenous ligands to activate TLR4. For example, LPS requires the co-receptors MD-2 and CD14 to activate TLR4, whereas tenascin-C does not (*11*). In addition, hyaluronan fragments use MD-2 and CD44, but not CD14, and induce patterns of gene expression that are distinct from that induced by LPS (*68*).

Another key question relates to how the FBG domain activates macrophage TLR4 in vivo. What are the physiologically relevant concentrations and form(s) of this region of tenascin-C? Note that this study assessed the response of macrophages to single (and different) concentration of LPS and of the FBG domain of tenascin-C at a single time point. Thus, we can only make conclusions about how cells respond under these restricted conditions. It is also difficult to know how the concentrations of the stimuli that we examined correspond to what a macrophage encounters in vivo. Although tissue concentrations of tenascin-C in the range of 0.37 to 1.2 μM have been reported (*69*, *70*), the amounts of tenascin-C are likely to be dependent on the tissue location and context. Moreover, here, we focused on a direct comparison of LPS- and FBG-mediated TLR4 signaling. It is possible that during tissue injury, tenascin-C is degraded, releasing proteolytic fragments consisting of the FBG domain, which are free to activate TLR4 in isolation from the rest of the tenascin-C molecule. FBG-containing tenascin-C fragments have been found in gingival crevicular fluid from a subset of periodontitis patients (*71*). Alternatively, macrophages could encounter intact tenascin-C that may either be soluble or incorporated into the tissue matrix. We previously showed that full-length tenascin-C induces TLR4-mediated cytokine synthesis equally as well as the FBG domain does alone (*11*). However, it will be important to examine not only how the FBG domain signals when present with other domains of tenascin-C, which may together synergistically affect macrophage activation, but also how it signals within the context of an insoluble 3D multicomponent extracellular matrix.

In conclusion, our data suggest that specific stimuli induce overlapping, yet distinct, biological outcomes upon activation of the same innate immune receptor. This study provides evidence that the innate immune system can interpret qualitatively different challenges and instruct inflammatory responses accordingly. It also highlights not only the fact that the microenvironment affects TLR function but also that TLR activation affects the microenvironment. Understanding how the cellular microenvironment regulates macrophage phenotype and behavior may help address how to manipulate inflammation in response to tissue injury and infection.

MATERIALS AND METHODS

Cell culture and stimulation

Primary human monocytes isolated from peripheral blood (London Blood Bank) were differentiated into macrophages (M-CSF-MDMs) by culturing them in RPMI 1640 containing 5% (v/v) fetal bovine serum (FBS) (Gibco), penicillin/streptomycin (100 U/ml; PAA), and recombinant human M-CSF (100 ng/ml; PeproTech) for 5 days (*72*). Adherent cells were washed, replated in RPMI 1640 containing 3% (v/v) FBS (Gibco) and penicillin/streptomycin (100 U/ml; PAA) for 24 hours before stimulation with LPS (1 ng/ml) [from *Escherichia coli* serotype EH100(Ra), TLR-grade; Enzo Life Sciences] or 1 μM FBG for 5, 15, or 30 min or for 1, 2, 3, 4, 8, or 24 hours. Recombinant human FBG was synthesized and purified as previously described (*11*) and, where stated, was preincubated with polymyxin B (10 μg/ml; Sigma). Primary human DFs were isolated from full-thickness skin samples. Tissue samples were dissected into small pieces and digested

in Dulbecco's modified Eagle's medium (DMEM) with 1% (v/v) penicillin/streptomycin, 5% (v/v) FBS (Gibco), type I collagenase (Worthington Biochemical Corporation), and deoxyribonuclease I (Roche Diagnostics) for up to 2 hours at 37°C. Cells were cultured in DMEM with 10% (v/v) FBS and 1% (v/v) penicillin/streptomycin. Cells up to passage two were used for experiments.

Inhibitors

M-CSF-MDMs were stimulated for 30 min or 1, 1.5, 2, or 24 hours with FBG or LPS in the presence or absence of DMSO, TAK-242 (3 μM; Invivogen), pAb-h TLR (1, 10, or 25 μg/ml; Invivogen), isotype control antibody (rat pAb control; 1, 10, or 25 μg/ml; Invivogen), or GM6001 (10 μM).

Cell viability

Cell viability was examined by MTT assay (Sigma-Aldrich), according to the manufacturer's instructions.

Enzyme-linked immunosorbent assay

Cell supernatants were analyzed with ELISA kits to quantify TNF-α, IL-6 and IL-8 (R&D Systems), IL-10 and IL-12 (BD Biosciences), and IL-23 (eBioscience), according to the manufacturers' instructions. Absorbance was read on a spectrophotometric ELISA plate reader, and the data were analyzed with Ascent Software (Thermo Labsystems).

Secreted embryonic alkaline phosphatase NF-κB activity assay

THP1-XBlue cells stably expressing an NF-κB–inducible and activating protein 1–inducible secreted embryonic alkaline phosphatase (SEAP) reporter gene (Invivogen) were cultured in RPMI 1640 supplemented with 10% (v/v) FBS (Gibco), penicillin (100 U/ml) and streptomycin (100 U/ml) (PAA), Normocin (100 μg/ml; Invivogen), and blasticidine-*S*-hydrochloride (10 μg/ml; Sigma). To monitor the activation of NF-κB signaling, 1×10^5 cells were stimulated with 0.5 μM FBG or LPS (0.5 ng/ml) for 1, 4, 8, or 24 hours, and the amount of secreted SEAP was measured by mixing 20 μl of the culture medium with 180 μl of QUANTI-Blue detection medium (Invivogen) and incubated for 2 hours at 37°C. Absorbance was measured at 620 nm with a FLUOstar Omega microplate reader (BMG LABTECH).

Phosphoprotein enrichment and CyDye labeling

M-CSF-MDMs (8×10^6) were treated with medium alone or with medium containing either 1 μM FBG or LPS (1 ng/ml) for 30 min before IMAC (*73*) was performed with the PhosphoProtein Purification Kit (Qiagen). Phosphoprotein-enriched fractions (5 μg) were labeled with 6 nM Cy3, whereas an internal standard, containing a mixture of equal amounts of each experimental protein sample, was labeled with 6 nM Cy5 saturation fluorescent dye, according to the manufacturer's instructions (CyDye DIGE Fluor Labeling Kit for Scarce Samples, GE Healthcare) by the proteomic services at the Cambridge Centre for Proteomics (www.bio.cam.ac.uk/proteomics). Briefly, labeling was optimized by titrating the reducing agent tris-(2-carboxyethyl)phosphine hydrochloride (TCEP) and the Cy3 and Cy5 dyes. The molar ratio of TCEP/dye was kept at 1:2 (1.5 nM TCEP and 3 nM dye; 2 nM TCEP and 4 nM dye; 2.5 nM TCEP and 5 nM dye; 3 nM TCEP and 6 nM dye; and 4 nM TCEP and 8 nM dye). The internal standard was included on each gel within the experiment. Proteins were reduced with 3 nM TCEP for 1 hour at 37°C in the dark and labeled with 6 nM Cy3 or Cy5 for 30 min at 37°C in the dark. The labeling reaction was quenched with 2× sample buffer (7 M urea, 2 M thiourea, and 4% CHAPS) containing 2% Pharmalytes and 130 mM dithiothreitol (DTT). Rehydration buffer [7 M urea, 2 M thiourea, 4% CHAPS, 1% Pharmalyte, and 13 mM DTT (broad-range pH 3 to 10)] was added before the labeled phosphoproteins were subjected to isoelectric focusing.

Two-dimensional difference gel electrophoresis

2D-DIGE was performed by the proteomic services at the Cambridge Centre for Proteomics, as previously described (*15*). Briefly, nonlinear immobilized pH gradient strips (13 cm long) (pH 3 to 10) (GE Healthcare) were rehydrated with CyDye-labeled samples at 20°C for 10 hours at 20 V with the IPGphor II apparatus (GE Healthcare), according to the manufacturer's instructions. Isoelectric focusing was performed for a total of 40,000 V·hour at 20°C at 50 mA. Before SDS-PAGE was performed, the strips were equilibrated for 15 min in 100 mM tris (pH 8.8), 30% (v/v) glycerol, 6 M urea, 2% (w/v) SDS, and 0.5% (w/v) DTT on a rocking table. The strips were loaded onto a 13-cm (1 mm thick), 12% acrylamide gel (pH 8.5) with a 1-cm, 4% stacker gel (pH 6.8). The strips were overlaid with 1% agarose in SDS running buffer containing 5 mg of bromophenol blue. The gels were run at 20 mA for 15 min and then at 40 mA at 20°C until the bromophenol blue dye front had run off the bottom of the gels. A 10× tris/glycine/SDS running buffer (Bio-Rad) was used. A total of 13 gels were run, including 12 analytical gels (10 μg of phosphoproteins/gel) representing four biological replicates and one preparative gel (170 μg of combined phosphoproteins in total).

Gel imaging and statistical analysis

After 2D-DIGE, CyDye-labeled proteins were visualized with Typhoon 9400 Imager (GE Healthcare) to generate overlaid, multichannel images for each gel. The Cy3 images were scanned with a 532-nm laser and a 580-nm band pass 30 (BP30) emission filter. Cy5 images were scanned with a 633-nm laser and a 670-nm BP30 emission filter. To ensure maximum pixel intensity for the two dyes (between 40,000 and 60,000 pixels), all gels were scanned at 100-μm pixel resolution, and the photomultiplier tube voltage was set to between 500 and 700 V. The scanned gel images were then transferred to the ImageQuant version 5.2 software package (GE Healthcare). After cropping, the images were exported to the DeCyder Batch Processor and Biological Variation Analysis module (DeCyder 2D version 5.2 Software, GE Healthcare) for statistical analysis, according to the manufacturer's recommendations. To compare protein spots across gels, a master image was picked from images of the internal standard. The statistical analysis of changes in protein abundance between different cell stimulations was performed by the DeCyder–Biological Variation Analysis version 5.2 module. Landmark spots were manually defined to improve the automated matching results. The preparative gel was scanned and matched with the master gel to assign the right correspondence for spot picking. Data were normalized for computing the fold changes in abundance. Protein spots with a statistically significant variation ($P \leq 0.05$), showing a difference in volume of 1.5-fold compared to the same spots from unstimulated cell samples, were considered to be differentially abundant and were analyzed by MS.

Protein identification by MS

The preparative gel was silver-stained for spot excision. The silver-stained image was scanned and spot-matched to the fluorescent images to ensure the accurate excision of proteins of interest. Gel spots were excised from the gels with a 10-ml pipette tip and were placed into a 96-well PCR plate. The gel spots were destained, reduced with DTT, and alkylated with iodoacetamide before being subjected to enzymatic digestion with sequencing grade trypsin (Promega) overnight at 37°C. After digestion, the reaction mixture was pipetted into a sample vial and loaded onto an autosampler for automated LC-MS/MS analysis. All LC-MS/MS experiments were

performed with the nanoACQUITY UPLC System (Waters Corporation) and an LTQ Orbitrap Velos hybrid ion trap mass spectrometer (Thermo Fisher Scientific). Separation of peptides was performed by reversed-phase chromatography with a Waters reversed-phase nanocolumn (BEH C18; 75 μm in diameter × 250 mm, 1.7-μm particle size) at a flow rate of 300 nl/min. Peptides were initially loaded onto a precolumn (Waters UPLC Trap Symmetry C18; 180 μm in diameter × 20 mm, 5-μm particle size) from the nanoACQUITY sample manager with 0.1% formic acid for 3 min at a flow rate of 10 μl/min. After this period, the column valve was switched to enable the elution of peptides from the precolumn onto the analytical column. Solvent A was water with 0.1% formic acid, and solvent B was acetonitrile with 0.1% formic acid. The linear gradient used was 5 to 40% solvent B over 60 min. The LC eluant was sprayed into the mass spectrometer by means of a New Objective nanospray source. All mass/charge ratio values of eluting ions were measured in the Orbitrap Velos mass analyzer, set at a resolution of 30,000. Data-dependent scans (top 20) were used to automatically isolate and generate fragment ions by collision-induced dissociation in the linear ion trap, resulting in the generation of MS/MS spectra. Ions with charge states of 2^+ and above were selected for fragmentation. After the run, the data were processed with Protein Discoverer (version 1.2, Thermo Fisher Scientific). Briefly, all of the MS/MS data were converted to mgf files, and these were submitted to the Mascot search algorithm (Matrix Science) and searched against the UniProt human database, using a fixed modification of carbamidomethyl, a variable modification of oxidation, and in specific cases, phosphorylation using a peptide tolerance of 20 ppm (MS) and 0.1 Da (MS/MS). Peptide identifications were accepted if they could be established at a probability greater than 95.0%.

Bioinformatics analysis

GO annotation enrichment analysis was performed with the PANTHER version 8.1 classification system (www.pantherdb.org) (*74*). The background data set for the analysis was the *H. sapiens* genome, and the binomial test ($P < 0.05$) was used for statistical overrepresentation. KEGG pathway enrichment and interaction network analyses were performed with STRING version 10.0 (http://string-db.org/) (*75*). The background data set for the analyses was the *H. sapiens* genome. Experimentally observed protein phosphorylation data mining was conducted with PhosphoSitePlus (www.phosphosite.org/homeAction.do) (*76*). Hierarchical clustering was performed with MultiExperiment Viewer version 4.9 (www.tm4.org).

Phosphoprotein gel staining

Pro-Q Diamond Phosphoprotein Gel Stain (Molecular Probes) was used to selectively stain phosphoproteins in SDS-PAGE gels, according to the manufacturer's instructions. Gels were visualized with FLA-5100 Fluorescent Image Analyzer (Fuji Photo Film Co.) using 532-nm excitation and 580-nm long pass emission filters. Gels were then stained with silver stain to detect total protein.

Western blotting analysis

Phosphoprotein-enriched fractions (eluate) and the flow-through after IMAC-based separation of macrophage proteins were resolved by SDS-PAGE and analyzed by Western blotting with rabbit antibodies against human phosphorylated extracellular signal–regulated kinases 1 and 2 (#4370), human pp38α (#9211), human phosphorylated MKK3/MKK6 (#12280), human MKK3 (#8535), human MKK6 (#8550, Cell Signaling Technology), mouse 4G10 Platinum anti-phosphotyrosine (#05-1050, Millipore), rabbit anti-human α-tubulin (ab6046), rabbit anti-human PSMA6 (ab97563), rabbit anti-human PSME1 (ab140501), rabbit anti-human HSPA6 (ab96754, Abcam), rabbit anti-human DCD (PA5-13677, Thermo Fisher Scientific), and rabbit anti-human COL1 (H-197, Santa Cruz Biotechnology) antibodies. Cell extracts were analyzed by Western blotting with goat anti-human actin (I-19, Santa Cruz Biotechnology) and rabbit anti-human pp38α (#9211, Cell Signaling Technology). Conditioned medium from LPS- and FBG-stimulated M-CSF-MDMs was analyzed by Western blotting with mouse anti-human MMP1 antibody (ab25483, Abcam). For validation experiments, 5×10^5 M-CSF-MDMs from new donors were stimulated, and cell extracts were prepared in 60 μl of lysis buffer [1% NP-40, 150 mM NaCl, and 20 mM tris (pH 7.5)] containing 10 mM EDTA, 10 mM EGTA, 1 mM Na_3VO_4, 5 mM NaF, and a protease inhibitor cocktail. Extracts were separated on 10% SDS-PAGE gels, and proteins were transferred to nitrocellulose membrane. The membranes were blocked in 5% bovine serum albumin (BSA) in tris-buffered saline (TBS) containing 0.1% Tween 20 (TBST) and were sequentially incubated with antibodies recognizing human pJNK (p46/54; #9521), human pp38α (#9211), human p38α (#8690, Cell Signaling Technology), human IκBα (C-15), human α-tubulin (B-7), human actin (I-19, Santa Cruz Biotechnology), and human β-tubulin (ab6046, Abcam). Blots were stripped of antibody between analyses with ReBlot Plus Strong Antibody Stripping Solution (Merck Millipore) and blocked again in 5% BSA-TBST. Densitometric analysis of bands was performed with Phoretix 1D Software (Totallab), and the results are presented as relative band volumes.

Immunofluorescence

M-CSF-MDMs were plated on glass coverslips and stimulated with 1 μM FBG or LPS (1 ng/ml). Cells were then fixed with 4% (v/v) paraformaldehyde (PFA) in TBS for 15 min at 4°C and permeabilized with 0.1% (v/v) Triton X-100 in TBS for 15 min at room temperature. Cells were incubated with blocking solution [5% (v/v) goat serum and 3% (w/v) BSA in TBS] for 1 hour at room temperature, which was followed by incubation for 1 hour at room temperature with anti-pp38α antibody (#9211, Cell Signaling Technology) diluted in blocking solution. After the cells were washed four times with TBS, they were incubated for 1 hour at room temperature with Alexa Fluor 568–conjugated secondary anti-rabbit immunoglobulin G (IgG) (Molecular Probes) diluted in blocking solution, and the nuclei were stained with DAPI. After the cells were washed four times in TBS, they were mounted onto glass slides with ProLong Gold Antifade Reagent (Invitrogen). Controls that were stained in the absence of primary antibody were also included. Images were captured by fluorescence microscopy (Zeiss Axio ScopeA.1 light/fluorescent microscope and AxioCam HRc camera). Multichannel images were generated with ImageJ software (http://imagej.nih.gov/ij/).

RNA extraction, quantitative real-time PCR, and RT-PCR

Total RNA was extracted from M-CSF-MDMs (1.5×10^6) with RNeasy Mini Kit (Qiagen). Complementary DNA (cDNA) was synthesized from equivalent amounts of total RNA with the High-Capacity cDNA Reverse Transcription Kit using random primers (Applied Biosystems). Quantitative real-time PCR was performed in a ViiA 7 machine (Applied Biosystems) with TaqMan primer sets for human *COL1A1* (Hs00164004_m1), *COL1A2* (Hs00164099_m1), *COL2A1* (Hs00264051_m1), *COL3A1* (Hs00943809_m1), *COL4A2* (Hs01098873_m1), *COL5A1* (Hs00609133_m1), *COL6A1* (Hs01095585_m1), *COL7A1* (Hs00164310_m1), *COL8A1* (Hs00156669_m1), *COL9A1* (Hs00932129_m1), *COL10A1* (Hs00166657_m1), *COL11A1* (Hs01097664_m1), *COL12A1* (Hs00189184_m1), *COL13A1* (Hs01103879_m1), *COL14A1* (Hs00964045_m1), *COL15A1* (Hs01557124_m1), *COL16A1*

(Hs00156876_m1), *COL17A1* (Hs00990036_m1), *COL18A1* (Hs00181017_m1), *COL19A1* (Hs00156940_m1), *COL20A1* (Hs00612130_m1), *COL21A1* (Hs00229402_m1), *COL22A1* (Hs01377192_m1), *COL23A1* (Hs00297526_m1), *COL24A1* (Hs00537698_m1), *COL25A1* (Hs00261300_m1), *COL26A1* (Hs00294957_m1), *COL27A1* (Hs00259829_m1), *COL28A1* (Hs00417144_m1), *MMP1* (Hs00899658_m1), *MMP13* (Hs00233992_m1), *MMP14* (Hs00237119_m1), *MRC1* (Hs00267207_m1), *Arg1* (Hs00968979_m1), and *HPRT1* (Hs02800695_m1). Changes in mRNA abundance in stimulated cells were calculated by the change-in-threshold ($\Delta\Delta C_T$) method with *HPRT1* as the endogenous control for gene expression and were normalized to results obtained from unstimulated cells.

Collagen film degradation assay

A collagen film degradation assay was performed as described previously (*77*). Briefly, M-CSF-MDMs were seeded on six-well culture plates coated with a thin layer of fibrillar type I bovine collagen (3 mg/ml; PureCol) in the presence or absence of LPS or FBG, and with or without GM6001. Five days later, the cells were removed by trypsinization, and the plates were fixed with 3% PFA in TBS for 20 min and stained with Coomassie Brilliant Blue R250. Images were captured with a charge-coupled device (CCD) camera–equipped microscope (Nikon TE2000-E). Degraded areas were visualized as white, unstained, and noncollagen-containing zones.

Fluorescently labeled gelatin film degradation assay

A gelatin film degradation assay was performed as described previously (*77*). Briefly, glass coverslips (18 mm in diameter) were coated with Alexa Fluor 488–conjugated gelatin. M-CSF-MDMs were seeded onto the fluorescently labeled gelatin–coated coverslips in the presence or absence of LPS or FBG, with or without GM6001, and were cultured for 64 hours. The cells were then fixed with 3% PFA in TBS for 15 min and immunostained. Cells were then incubated with blocking solution [5% (v/v) goat serum and 3% (w/v) BSA in TBS] for 1 hour at room temperature, which was followed by incubation for 2 hours at room temperature with rabbit anti-human MMP14 (ab51074, Abcam). After the cells were washed four times with TBS, they were incubated for 1 hour at room temperature with Alexa Fluor 568–conjugated secondary anti-rabbit IgG (Molecular Probes) diluted in blocking solution, and the nuclei were stained with DAPI. After the cells were washed four times with TBS, they were mounted onto glass slides with ProLong Gold Antifade Reagent (Invitrogen). Controls that were stained in the absence of primary antibody were included. Images were captured with a CCD camera–equipped microscope (Nikon TE2000-E). Degraded areas were visualized as dark, nonfluorescent zones.

Statistical analysis

Statistical analysis was performed with paired *t* test by one-way ANOVA, or by two-way ANOVA, with Sidak's multiple comparisons test, where appropriate, with Prism 6 software (GraphPad software).

SUPPLEMENTARY MATERIALS

www.sciencesignaling.org/cgi/content/full/9/443/ra86/DC1
Fig. S1. FBG-mediated activation of macrophages is not inhibited by polymyxin B.
Fig. S2. Validation of phosphoprotein enrichment.
Fig. S3. Signaling pathway analysis of macrophages activated with FBG or LPS.
Fig. S4. Comparison of LPS- and FBG-stimulated MAPK signaling in macrophages.
Fig. S5. Analysis of LPS- and FBG-stimulated collagen synthesis by macrophages.
Fig. S6. Analysis of the amount of pro-MMP1 protein in macrophages stimulated with LPS or FBG.

REFERENCES AND NOTES

1. T. A. Wynn, A. Chawla, J. W. Pollard, Macrophage biology in development, homeostasis and disease. *Nature* **496**, 445–455 (2013).
2. D. M. Mosser, J. P. Edwards, Exploring the full spectrum of macrophage activation. *Nat. Rev. Immunol.* **8**, 958–969 (2008).
3. S. Epelman, K. J. Lavine, G. J. Randolph, Origin and functions of tissue macrophages. *Immunity* **41**, 21–35 (2014).
4. Y. Lavin, D. Winter, R. Blecher-Gonen, E. David, H. Keren-Shaul, M. Merad, S. Jung, I. Amit, Tissue-resident macrophage enhancer landscapes are shaped by the local microenvironment. *Cell* **159**, 1312–1326 (2014).
5. M. Haldar, M. Kohyama, A. Y.-L. So, W. KC, X. Wu, C. G. Briseño, A. T. Satpathy, N. M. Kretzer, H. Arase, N. S. Rajasekaran, L. Wang, T. Egawa, K. Igarashi, D. Baltimore, T. L. Murphy, K. M. Murphy, Heme-mediated SPI-C induction promotes monocyte differentiation into iron-recycling macrophages. *Cell* **156**, 1223–1234 (2014).
6. Y. Okabe, R. Medzhitov, Tissue-specific signals control reversible program of localization and functional polarization of macrophages. *Cell* **157**, 832–844 (2014).
7. S. Abutbul, J. Shapiro, I. Szaingurten-Solodkin, N. Levy, Y. Carmy, R. Baron, S. Jung, A. Monsonego, TGF-β signaling through SMAD2/3 induces the quiescent microglial phenotype within the CNS environment. *Glia* **60**, 1160–1171 (2012).
8. P. R. Taylor, L. Martinez-Pomares, M. Stacey, H.-H. Lin, G. D. Brown, S. Gordon, Macrophage receptors and immune recognition. *Annu. Rev. Immunol.* **23**, 901–944 (2005).
9. C. E. Bryant, N. J. Gay, S. Heymans, S. Sacre, L. Schaefer, K. S. Midwood, Advances in Toll-like receptor biology: Modes of activation by diverse stimuli. *Crit. Rev. Biochem. Mol. Biol.* **50**, 359–379 (2015).
10. I. A. Udalova, M. Ruhmann, S. J. P. Thomson, K. S. Midwood, Expression and immune function of tenascin-C. *Crit. Rev. Immunol.* **31**, 115–145 (2011).
11. K. Midwood, S. Sacre, A. M. Piccinini, J. Inglis, A. Trebaul, E. Chan, S. Drexler, N. Sofat, M. Kashiwagi, G. Orend, F. Brennan, B. Foxwell, Tenascin-C is an endogenous activator of Toll-like receptor 4 that is essential for maintaining inflammation in arthritic joint disease. *Nat. Med.* **15**, 774–780 (2009).
12. L. Patel, W. Sun, S. S. Glasson, E. A. Morris, C. R. Flannery, P. S. Chockalingam, Tenascin-C induces inflammatory mediators and matrix degradation in osteoarthritic cartilage. *BMC Musculoskelet. Disord.* **12**, 164 (2011).
13. N. Kuriyama, S. Duarte, T. Hamada, R. W. Busuttil, A. J. Coito, Tenascin-C: A novel mediator of hepatic ischemia and reperfusion injury. *Hepatology* **54**, 2125–2136 (2011).
14. P. J. Murray, J. E. Allen, S. K. Biswas, E. A. Fisher, D. W. Gilroy, S. Goerdt, S. Gordon, J. A. Hamilton, L. B. Ivashkiv, T. Lawrence, M. Locati, A. Mantovani, F. O. Martinez, J.-L. Mege, D. M. Mosser, G. Natoli, J. P. Saeij, J. L. Schultze, K. A. Shirey, A. Sica, J. Suttles, I. Udalova, J. A. van Ginderachter, S. N. Vogel, T. A. Wynn, Macrophage activation and polarization: Nomenclature and experimental guidelines. *Immunity* **41**, 14–20 (2014).
15. K. S. Lilley, Protein profiling using two-dimensional difference gel electrophoresis (2-D DIGE). *Curr. Protoc. Protein Sci.* **22**, 1–14 (2003).
16. G. Weintz, J. V. Olsen, K. Frühauf, M. Niedzielska, I. Amit, J. Jantsch, J. Mages, C. Frech, L. Dölken, M. Mann, R. Lang, The phosphoproteome of toll-like receptor-activated macrophages. *Mol. Syst. Biol.* **6**, 371 (2010).
17. V. Sjoelund, M. Smelkinson, A. Nita-Lazar, Phosphoproteome profiling of the macrophage response to different toll-like receptor ligands identifies differences in global phosphorylation dynamics. *J. Proteome Res.* **13**, 5185–5197 (2014).
18. J. M. Blander, Coupling Toll-like receptor signaling with phagocytosis: Potentiation of antigen presentation. *Trends Immunol.* **28**, 19–25 (2007).
19. D. C. Morrison, L. F. Kline, Activation of the classical and properdin pathways of complement by bacterial lipopolysaccharides (LPS). *J. Immunol.* **118**, 362–368 (1977).
20. L. Koch, S. Hofer, M. A. Weigand, D. Frommhold, J. Poeschl, P. Ruef, Inhibition of LPS-induced activation of coagulation by p38 MAPK inhibitor. *ISRN Hematol.* **2012**, 762614 (2012).
21. K. A. Shirey, W. Lai, A. J. Scott, M. Lipsky, P. Mistry, L. M. Pletneva, C. L. Karp, J. McAlees, T. L. Gioannini, J. Weiss, W. H. Chen, R. K. Ernst, D. P. Rossignol, F. Gusovsky, J. C. G. Blanco, S. N. Vogel, The TLR4 antagonist Eritoran protects mice from lethal influenza infection. *Nature* **497**, 498–502 (2013).
22. Y. Goto, K. Ogawa, T. J. Nakamura, A. Hattori, M. Tsujimoto, TLR-mediated secretion of endoplasmic reticulum aminopeptidase 1 from macrophages. *J. Immunol.* **192**, 4443–4452 (2014).
23. B. Calippe, V. Douin-Echinard, L. Delpy, M. Laffargue, K. Lélu, A. Krust, B. Pipy, F. Bayard, J.-F. Arnal, J.-C. Guery, P. Gourdy, 17β-estradiol promotes TLR4-triggered proinflammatory mediator production through direct estrogen receptor α signaling in macrophages in vivo. *J. Immunol.* **185**, 1169–1176 (2010).
24. P. N. Shashkin, G. T. Brown, A. Ghosh, G. K. Marathe, T. M. McIntyre, Lipopolysaccharide is a direct agonist for platelet RNA splicing. *J. Immunol.* **181**, 3495–3502 (2008).
25. K. Yamazaki, K. Suzuki, E. Yamada, T. Yamada, F. Takeshita, M. Matsumoto, T. Mitsuhashi, T. Obara, K. Takano, K. Sato, Suppression of iodide uptake and thyroid hormone synthesis

with stimulation of the type I interferon system by double-stranded ribonucleic acid in cultured human thyroid follicles. *Endocrinology* **148**, 3226–3235 (2007).
26. S. Galván-Peña, L. A. J. O'Neill, Metabolic reprograming in macrophage polarization. *Front. Immunol.* **5**, 420 (2014).
27. M. Schaff, N. Receveur, C. Bourdon, V. Wurtz, C. V. Denis, G. Orend, C. Gachet, F. Lanza, P. H. Mangin, Novel function of tenascin-C, a matrix protein relevant to atherosclerosis, in platelet recruitment and activation under flow. *Arterioscler. Thromb. Vasc. Biol.* **31**, 117–124 (2011).
28. K. S. Midwood, T. Hussenet, B. Langlois, G. Orend, Advances in tenascin-C biology. *Cell. Mol. Life Sci.* **68**, 3175–3199 (2011).
29. M. A. Ghert, W. N. Qi, H. P. Erickson, J. A. Block, S. P. Scully, Tenascin-C splice variant adhesive/anti-adhesive effects on chondrosarcoma cell attachment to fibronectin. *Cell Struct. Funct.* **26**, 179–187 (2001).
30. R. A. Clark, H. P. Erickson, T. A. Springer, Tenascin supports lymphocyte rolling. *J. Cell Biol.* **137**, 755–765 (1997).
31. X.-G. Gong, Y.-F. Lv, X.-Q. Li, F.-G. Xu, Q.-Y. Ma, Gemcitabine resistance induced by interaction between alternatively spliced segment of tenascin-C and annexin A2 in pancreatic cancer cells. *Biol. Pharm. Bull.* **33**, 1261–1267 (2010).
32. T. Sumioka, N. Fujita, A. Kitano, Y. Okada, S. Saika, Impaired angiogenic response in the cornea of mice lacking tenascin C. *Invest. Ophthalmol. Vis. Sci.* **52**, 2462–2467 (2011).
33. Y. Urushizaki, S. Seifter, Phosphorylation of hydroxylysine residues in collagen synthesized by cultured aortic smooth muscle cells. *Proc. Natl. Acad. Sci. U.S.A.* **82**, 3091–3095 (1985).
34. E. P. Zimina, A. Fritsch, B. Schermer, A. Y. Bakulina, M. Bashkurov, T. Benzing, L. Bruckner-Tuderman, Extracellular phosphorylation of collagen XVII by ecto-casein kinase 2 inhibits ectodomain shedding. *J. Biol. Chem.* **282**, 22737–22746 (2007).
35. D. Olsen, J. Jiang, R. Chang, R. Duffy, M. Sakaguchi, S. Leigh, R. Lundgard, J. Ju, F. Buschman, V. Truong-Le, B. Pham, J. W. Polarek, Expression and characterization of a low molecular weight recombinant human gelatin: Development of a substitute for animal-derived gelatin with superior features. *Protein Expr. Purif.* **40**, 346–357 (2005).
36. K. Sharma, R. C. J. D'Souza, S. Tyanova, C. Schaab, J. R. Wisniewski, J. Cox, M. Mann, Ultradeep human phosphoproteome reveals a distinct regulatory nature of Tyr and Ser/Thr-based signaling. *Cell Rep.* **8**, 1583–1594 (2014).
37. S. A. Beausoleil, J. Villén, S. A. Gerber, J. Rush, S. P. Gygi, A probability-based approach for high-throughput protein phosphorylation analysis and site localization. *Nat. Biotechnol.* **24**, 1285–1292 (2006).
38. H. Molina, D. M. Horn, N. Tang, S. Mathivanan, A. Pandey, Global proteomic profiling of phosphopeptides using electron transfer dissociation tandem mass spectrometry. *Proc. Natl. Acad. Sci. U.S.A.* **104**, 2199–2204 (2007).
39. E. Adiguzel, G. Hou, D. Mulholland, U. Hopfer, N. Fukai, B. Olsen, M. Bendeck, Migration and growth are attenuated in vascular smooth muscle cells with type VIII collagen-null alleles. *Arterioscler. Thromb. Vasc. Biol.* **26**, 56–61 (2006).
40. J. Banyard, L. Bao, B. R. Zetter, Type XXIII collagen, a new transmembrane collagen identified in metastatic tumor cells. *J. Biol. Chem.* **278**, 20989–20994 (2003).
41. K. Misawa, T. Kanazawa, A. Imai, S. Endo, D. Mochizuki, H. Fukushima, Y. Misawa, H. Mineta, Prognostic value of type XXII and XXIV collagen mRNA expression in head and neck cancer patients. *Mol. Clin. Oncol.* **2**, 285–291 (2014).
42. K. S. Midwood, G. Orend, The role of tenascin-C in tissue injury and tumorigenesis. *J. Cell Commun. Signal.* **3**, 287–310 (2009).
43. D. M. Rothwarf, E. Zandi, G. Natoli, M. Karin, IKK-γ is an essential regulatory subunit of the IκB kinase complex. *Nature* **395**, 297–300 (1998).
44. P. Bartuzi, M. H. Hofker, B. van de Sluis, Tuning NF-κB activity: A touch of COMMD proteins. *Biochim. Biophys. Acta* **1832**, 2315–2321 (2013).
45. B. Janji, A. Giganti, V. De Corte, M. Catillon, E. Bruyneel, D. Lentz, J. Plastino, J. Gettemans, E. Friederich, Phosphorylation on Ser5 increases the F-actin-binding activity of L-plastin and promotes its targeting to sites of actin assembly in cells. *J. Cell Sci.* **119**, 1947–1960 (2006).
46. S. Mostowy, P. Cossart, Septins: The fourth component of the cytoskeleton. *Nat. Rev. Mol. Cell Biol.* **13**, 183–194 (2012).
47. T. Katsumoto, A. Mitsushima, T. Kurimura, The role of the vimentin intermediate filaments in rat 3Y1 cells elucidated by immunoelectron microscopy and computer-graphic reconstruction. *Biol. Cell* **68**, 139–146 (1990).
48. K. Tanaka, N. Hiraiwa, H. Hashimoto, Y. Yamazaki, M. Kusakabe, Tenascin-C regulates angiogenesis in tumor through the regulation of vascular endothelial growth factor expression. *Int. J. Cancer* **108**, 31–40 (2004).
49. P. Bist, S. Shu, H. Lee, S. Arora, S. Nair, J. Y. Lim, J. Dayalan, S. Gasser, S. K. Biswas, A.-M. Fairhurst, L. H. K. Lim, Annexin-A1 regulates TLR-mediated IFN-β production through an interaction with TANK-binding kinase 1. *J. Immunol.* **191**, 4375–4382 (2013).
50. J. F. A. Swisher, N. Burton, S. M. Bacot, S. N. Vogel, G. M. Feldman, Annexin A2 tetramer activates human and murine macrophages through TLR4. *Blood* **115**, 549–558 (2010).
51. M. Chopin, C. A. Chacón-Martínez, R. Jessberger, Fine tuning of IRF-4 expression by SWAP-70 controls the initiation of plasma cell development. *Eur. J. Immunol.* **41**, 3063–3074 (2011).
52. B. Kelly, L. A. J. O'Neill, Metabolic reprogramming in macrophages and dendritic cells in innate immunity. *Cell Res.* **25**, 771–784 (2015).
53. T. T. N. Nguyen, Y. M. Kim, T. D. Kim, O. T. T. Le, J. J. Kim, H. C. Kang, H. Hasegawa, Y. Kanaho, I. Jou, S. Y. Lee, Phosphatidylinositol 4-phosphate 5-kinase α facilitates Toll-like receptor 4-mediated microglial inflammation through regulation of the Toll/interleukin-1 receptor domain-containing adaptor protein (TIRAP) location. *J. Biol. Chem.* **288**, 5645–5659 (2013).
54. O. T. Le, T. T. Nguyen, S. Y. Lee, Phosphoinositide turnover in Toll-like receptor signaling and trafficking. *BMB Rep.* **47**, 361–368 (2014).
55. C.-Y. Chiang, V. Veckman, K. Limmer, M. David, Phospholipase Cγ-2 and intracellular calcium are required for lipopolysaccharide-induced Toll-like receptor 4 (TLR4) endocytosis and interferon regulatory factor 3 (IRF3) activation. *J. Biol. Chem.* **287**, 3704–3709 (2012).
56. S. Carpenter, E. P. Ricci, B. C. Mercier, M. J. Moore, K. A. Fitzgerald, Post-transcriptional regulation of gene expression in innate immunity. *Nat. Rev. Immunol.* **14**, 361–376 (2014).
57. A. M. Piccinini, K. S. Midwood, DAMPening inflammation by modulating TLR signalling. *Mediators Inflamm.* **2010**, 672395 (2010).
58. A. Veis, C. Sfeir, C. B. Wu, Phosphorylation of the proteins of the extracellular matrix of mineralized tissues by casein kinase-like activity. *Crit. Rev. Oral Biol. Med.* **8**, 360–379 (1997).
59. D. Volpin, A. Veis, Cyanogen bromide peptides from insoluble skin and dentin bovine collagens. *Biochemistry* **12**, 1452–1464 (1973).
60. T. Ishigaki, K. Imanaka-Yoshida, N. Shimojo, S. Matsushima, W. Taki, T. Yoshida, Tenascin-C enhances crosstalk signaling of integrin αvβ3/PDGFR-β complex by SRC recruitment promoting PDGF-induced proliferation and migration in smooth muscle cells. *J. Cell. Physiol.* **226**, 2617–2624 (2011).
61. V. Van De Bor, G. Zimniak, L. Papone, D. Cerezo, M. Malbouyres, T. Juan, F. Ruggiero, S. Noselli, Companion blood cells control ovarian stem cell niche microenvironment and homeostasis. *Cell Rep.* **13**, 546–560 (2015).
62. J. Vaage, W. J. Lindblad, Production of collagen type I by mouse peritoneal macrophages. *J. Leukoc. Biol.* **48**, 274–280 (1990).
63. B. Weitkamp, P. Cullen, G. Plenz, H. Robenek, J. Rauterberg, Human macrophages synthesize type VIII collagen in vitro and in the atherosclerotic plaque. *FASEB J.* **13**, 1445–1457 (1999).
64. M. Schnoor, P. Cullen, J. Lorkowski, K. Stolle, H. Robenek, D. Troyer, J. Rauterberg, S. Lorkowski, Production of type VI collagen by human macrophages: A new dimension in macrophage functional heterogeneity. *J. Immunol.* **180**, 5707–5719 (2008).
65. B. Leitinger, E. Hohenester, Mammalian collagen receptors. *Matrix Biol.* **26**, 146–155 (2007).
66. J. E. Scott, Extracellular matrix, supramolecular organisation and shape. *J. Anat.* **187** (Pt. 2), 259–269 (1995).
67. M. J. Rowley, K. S. Nandakumar, R. Holmdahl, The role of collagen antibodies in mediating arthritis. *Mod. Rheumatol.* **18**, 429–441 (2008).
68. K. R. Taylor, K. Yamasaki, K. A. Radek, A. Di Nardo, H. Goodarzi, D. Golenbock, B. Beutler, R. L. Gallo, Recognition of hyaluronan released in sterile injury involves a unique receptor complex dependent on Toll-like receptor 4, CD44, and MD-2. *J. Biol. Chem.* **282**, 18265–18275 (2007).
69. V. A. Lightner, C. A. Slemp, H. P. Erickson, Localization and quantitation of hexabrachion (tenascin) in skin, embryonic brain, tumors, and plasma. *Ann. N. Y. Acad. Sci.* **580**, 260–275 (1990).
70. J. B. Ventimiglia, C. J. Wikstrand, L. E. Ostrowski, M. A. Bourdon, V. A. Lightner, D. D. Bigner, Tenascin expression in human glioma cell lines and normal tissues. *J. Neuroimmunol.* **36**, 41–55 (1992).
71. S. Ruggiero, R. Cosgarea, J. Potempa, B. Potempa, S. Eick, M. Chiquet, Cleavage of extracellular matrix in periodontitis: Gingipains differentially affect cell adhesion activities of fibronectin and tenascin-C. *Biochim. Biophys. Acta* **1832**, 517–526 (2013).
72. F. G. Goh, A. M. Piccinini, T. Krausgruber, I. A. Udalova, K. S. Midwood, Transcriptional regulation of the endogenous danger signal tenascin-C: A novel autocrine loop in inflammation. *J. Immunol.* **184**, 2655–2662 (2010).
73. M. Machida, H. Kosako, K. Shirakabe, M. Kobayashi, M. Ushiyama, J. Inagawa, J. Hirano, T. Nakano, Y. Bando, E. Nishida, S. Hattori, Purification of phosphoproteins by immobilized metal affinity chromatography and its application to phosphoproteome analysis. *FEBS J.* **274**, 1576–1587 (2007).
74. H. Mi, A. Muruganujan, J. T. Casagrande, P. D. Thomas, Large-scale gene function analysis with the PANTHER classification system. *Nat. Protoc.* **8**, 1551–1566 (2013).
75. D. Szklarczyk, A. Franceschini, S. Wyder, K. Forslund, D. Heller, J. Huerta-Cepas, M. Simonovic, A. Roth, A. Santos, K. P. Tsafou, M. Kuhn, P. Bork, L. J. Jensen, C. von Mering, STRING v10: Protein–protein interaction networks, integrated over the tree of life. *Nucleic Acids Res.* **43**, D447–D452 (2015).
76. P. V. Hornbeck, B. Zhang, B. Murray, J. M. Kornhauser, V. Latham, E. Skrzypek, PhosphoSitePlus, 2014: Mutations, PTMs and recalibrations. *Nucleic Acids Res.* **43**, D512–D520 (2015).

77. A. M. Woskowicz, S. A. Weaver, Y. Shitomi, N. Ito, Y. Itoh, MT-LOOP-dependent localization of membrane type I matrix metalloproteinase (MT1-MMP) to the cell adhesion complexes promotes cancer cell invasion. *J. Biol. Chem.* **288**, 35126–35137 (2013).

Acknowledgments: We thank Y. Shitomi and K. Yamamoto for advice on collagen and gelatin film degradation assays and MMP1 protein detection, S. Giblin for providing RNA extracted from human DFs, L. Thompson for critically reading the manuscript, and A. Judge for confirming our use of appropriate statistical analyses. **Funding:** This work was supported by the Medical Research Council, Arthritis Research U.K., and the Kennedy Trust for Rheumatology Research. **Author contributions:** A.M.P., L.Z., and J.M.P.L. performed the experiments. A.M.P. and K.S.M. designed the experiments, analyzed the data, and wrote the paper. **Competing interests:** The authors declare that they have no competing interests. **Data and materials availability:** MS data from this study have been deposited in the PeptideAtlas repository with the identifier PASS00922.

Submitted 29 January 2016
Accepted 15 August 2016
Final Publication 30 August 2016
10.1126/scisignal.aaf3596
Citation: A. M. Piccinini, L. Zuliani-Alvarez, J. M. P. Lim, K. S. Midwood, Distinct microenvironmental cues stimulate divergent TLR4-mediated signaling pathways in macrophages. *Sci. Signal.* **9**, ra86 (2016).

CANCER IMMUNOLOGY

Bypassing STAT3-mediated inhibition of the transcriptional regulator ID2 improves the antitumor efficacy of dendritic cells

Haiyan S. Li *et al.* (Stephanie S. Watowich)

Citation
Sci. Signal. 27 Sep 2016:
Vol. 9, Issue 447, ra94

10.1126/scisignal.aaf3957

Despite the potent ability of dendritic cells (DCs) to stimulate lymphocyte responses and host immunity, granulocyte-macrophage colony-stimulating factor–derived DCs (GM-DCs) used as antitumor vaccines have demonstrated relatively modest success in cancer immunotherapy. We found that injecting GM-DCs into melanoma tumors in mice, or culturing GM-DCs with melanoma-secreted cytokines or melanoma-conditioned medium, rapidly suppressed DC-intrinsic expression of the gene encoding inhibitor of differentiation 2 (ID2), a transcriptional regulator. Melanoma-associated cytokines repressed *Id2* transcription in murine DCs through the activation of signal transducer and activator of transcription 3 (STAT3). Enforced expression of ID2 in GM-DCs (ID2–GM-DCs) suppressed their production of the proinflammatory cytokine tumor necrosis factor–α (TNF-α). Vaccination with ID2–GM-DCs slowed the progression of melanoma tumors and enhanced animal survival, which was associated with an increased abundance of tumor-infiltrating interferon-γ–positive $CD4^+$ effector and $CD8^+$ cytotoxic T cells and a decreased number of tumor-infiltrating regulatory $CD4^+$ T cells. The efficacy of the ID2–GM-DC vaccine was improved by combinatorial treatment with a blocking antibody to programmed cell death protein–1 (PD-1), a current immunotherapy that overcomes suppressive immune checkpoint signaling. Collectively, our data reveal a previously unrecognized STAT3-mediated immunosuppressive mechanism in DCs and indicate that DC-intrinsic ID2 promotes tumor immunity by modulating tumor-associated $CD4^+$ T cell responses. Thus, inhibiting STAT3 or overexpressing ID2 selectively in DCs may improve the efficiency of DC vaccines in cancer therapy.

OXIDATIVE STRESS

Reactive oxygen species induce virus-independent MAVS oligomerization in systemic lupus erythematosus

Iwona A. Buskiewicz *et al.* (Andreas Koenig)

Citation
Sci. Signal. 29 Nov 2016:
Vol. 9, Issue 456, ra115

10.1126/scisignal.aaf1933

The increased expression of genes induced by type I interferon (IFN) is characteristic of viral infections and systemic lupus erythematosus (SLE). We showed that mitochondrial antiviral signaling (MAVS) protein, which normally forms a complex with retinoic acid gene I (RIG-I)–like helicases during viral infection, was activated by oxidative stress independently of RIG-I helicases. We found that chemically generated oxidative stress stimulated the formation of MAVS oligomers, which led to mitochondrial hyperpolarization and decreased adenosine triphosphate production and spare respiratory capacity, responses that were not observed in similarly treated cells lacking MAVS. Peripheral blood lymphocytes of SLE patients also showed spontaneous MAVS oligomerization that correlated with the increased secretion of type I IFN and mitochondrial oxidative stress. Furthermore, inhibition of mitochondrial reactive oxygen species (ROS) by the mitochondria-targeted antioxidant MitoQ prevented MAVS oligomerization and type I IFN production. ROS-dependent MAVS oligomerization and type I IFN production were reduced in cells expressing the MAVS-C79F variant, which occurs in 30% of sub-Saharan Africans and is linked with reduced type I IFN secretion and milder disease in SLE patients. Patients expressing the MAVS-C79F variant also had reduced amounts of oligomerized MAVS in their plasma compared to healthy controls. Together, our findings suggest that oxidative stress–induced MAVS oligomerization in SLE patients may contribute to the type I IFN signature that is characteristic of this syndrome.

Science Translational Medicine

CANCER

Cytokine-induced memory-like natural killer cells exhibit enhanced responses against myeloid leukemia

Rizwan Romee,[1]* Maximillian Rosario,[1,2]* Melissa M. Berrien-Elliott,[1]* Julia A. Wagner,[1] Brea A. Jewell,[1] Timothy Schappe,[1] Jeffrey W. Leong,[1] Sara Abdel-Latif,[1] Stephanie E. Schneider,[1] Sarah Willey,[1] Carly C. Neal,[1] Liyang Yu,[3] Stephen T. Oh,[3] Yi-Shan Lee,[2] Arend Mulder,[4] Frans Claas,[4] Megan A. Cooper,[5] Todd A. Fehniger[1]†

Natural killer (NK) cells are an emerging cellular immunotherapy for patients with acute myeloid leukemia (AML); however, the best approach to maximize NK cell antileukemia potential is unclear. Cytokine-induced memory-like NK cells differentiate after a brief preactivation with interleukin-12 (IL-12), IL-15, and IL-18 and exhibit enhanced responses to cytokine or activating receptor restimulation for weeks to months after preactivation. We hypothesized that memory-like NK cells exhibit enhanced antileukemia functionality. We demonstrated that human memory-like NK cells have enhanced interferon-γ production and cytotoxicity against leukemia cell lines or primary human AML blasts in vitro. Using mass cytometry, we found that memory-like NK cell functional responses were triggered against primary AML blasts, regardless of killer cell immunoglobulin-like receptor (KIR) to KIR-ligand interactions. In addition, multidimensional analyses identified distinct phenotypes of control and memory-like NK cells from the same individuals. Human memory-like NK cells xenografted into mice substantially reduced AML burden in vivo and improved overall survival. In the context of a first-in-human phase 1 clinical trial, adoptively transferred memory-like NK cells proliferated and expanded in AML patients and demonstrated robust responses against leukemia targets. Clinical responses were observed in five of nine evaluable patients, including four complete remissions. Thus, harnessing cytokine-induced memory-like NK cell responses represents a promising translational immunotherapy approach for patients with AML.

INTRODUCTION

Acute myeloid leukemia (AML) is a hematologic malignancy primarily of older individuals that remains a substantial clinical challenge (*1*). Currently, less than 30% of AML patients are cured with standard therapies, and relapsed/refractory (rel/ref) AML patients who are not candidates for hematopoietic cell transplantation (HCT) have a poor prognosis and no curative treatment options (*2*, *3*). Cellular immunotherapy mediated by alloreactive T and NK cells administered in the context of an allogeneic HCT is an effective treatment for AML; however, most AML patients are not candidates for this procedure because it is associated with substantial treatment-related morbidity and mortality (*4*, *5*). An alternative approach that provides the immunotherapeutic benefits of allogeneic HCT without severe toxicity is the adoptive transfer of allogeneic lymphocytes that mediate the "graft versus leukemia" effect. This strategy may expand the option of cellular immunotherapy to most AML patients.

Natural killer (NK) cells are innate lymphoid cells that are important for host defense against pathogens and mediate antitumor immune responses (*6*, *7*). Major histocompatibility complex (MHC)–haploidentical NK cells exhibit antileukemia responses without causing "graft versus host disease" (GVHD) after HCT (*8*), providing evidence of their utility as a cellular effector for leukemia patients. Allogeneic NK cell adoptive transfer is safe and can induce remissions in patients with leukemia (*9*–*12*); however, these studies have been limited by inadequate persistence, expansion, and in vivo antileukemia activity of the adoptively transferred NK cells. Thus, one key barrier in the field is the need for biology-driven approaches to enhance NK cell antitumor functionality before adoptive transfer.

Although NK cells have traditionally been considered members of the innate immune system, paradigm-shifting studies in mice have identified memory-like properties after hapten exposure, virus infection, or combined interleukin-12 (IL-12), IL-15, and IL-18 cytokine preactivation (*13*, *14*). Cytokine-induced memory-like NK cells were defined by briefly preactivating murine NK cells with IL-12, IL-15, and IL-18, followed by adoptive transfer into syngeneic mice. Weeks to months later, memory-like NK cells had proliferated and exhibited enhanced restimulation responses to cytokines or triggering via activating receptors (*15*, *16*). This preactivation approach also resulted in antitumor responses to murine NK cell–sensitive cell lines after adoptive transfer in mice (*17*). The potential translation of these findings as immunotherapy was established by the identification of human IL-12, IL-15, and IL-18–induced memory-like NK cells (*18*). Key properties of human memory-like NK cells include enhanced proliferation, expression of the high-affinity IL-2 receptor αβγ (IL-2Rαβγ), and increased interferon-γ (IFN-γ) production after restimulation with cytokines or via activating receptors (*19*, *20*). However, the ability of human memory-like NK cells to respond to cancer target cells has not been extensively reported. We hypothesized that human cytokine-induced memory-like NK cells exhibit enhanced antileukemia properties. This was tested in vitro against primary AML blasts and in vivo in nonobese diabetic (NOD)/severe combined immunodeficient (SCID)/common gamma chain$^{-/-}$ ($\gamma c^{-/-}$) (NSG) mouse xenograft models and in AML patients

[1]Division of Oncology, Department of Medicine, Washington University School of Medicine, St. Louis, MO 63110, USA. [2]Department of Pathology, Washington University School of Medicine, St. Louis, MO 63110, USA. [3]Division of Hematology, Department of Medicine, Washington University School of Medicine, St. Louis, MO 63110, USA. [4]Department of Immunohematology and Blood Transfusion, Leiden University Medical Center, 2333 ZC Leiden, Netherlands. [5]Division of Rheumatology, Department of Pediatrics, Washington University School of Medicine, St. Louis, MO 63110, USA.
*These authors contributed equally to this work.
†Corresponding author. Email: tfehnige@wustl.edu

who were administered memory-like NK cells as part of a first-in-human clinical trial. Our results demonstrate that combined preactivation with IL-12, IL-15, and IL-18 differentiates cytokine-induced memory-like NK cells that have potent antileukemia functionality in vitro and in vivo and thus represent a promising immunotherapy strategy for AML patients.

RESULTS

Memory-like NK cells exhibit enhanced functional responses against leukemia target cells

Although the enhanced recall response of human IL-12, IL-15, and IL-18–induced memory-like NK cells was well established after cytokine receptor restimulation (*18*), their response to leukemia target cells, including primary AML blasts, was not extensively studied. To address this issue, we preactivated human NK cells with IL-12, IL-15, and IL-18 or control conditions (low-dose IL-15 only) overnight and then differentiated memory-like or control NK cells from the same individual for 7 days (Fig. 1A). Memory-like NK cells exhibited enhanced IFN-γ production in response to restimulation with both K562 leukemia cells (Fig. 1, A and B) and primary AML blasts (Fig. 1, A and C). In addition, memory-like NK cells demonstrated significantly higher cytotoxicity compared to control NK cells from the same donors, which was dependent on NKG2D and DNAM-1 ($P = 0.02$; Fig. 1D and fig. S1). Consistent with augmented cytotoxicity, we observed increased expression of the cytotoxic effector protein granzyme B (Fig. 1, E and F). To further define the differences between memory-like and control NK cells, we established a mass cytometry panel that included functionally relevant proteins to deeply immunophenotype NK cells.

Mass cytometry defines the differences between memory-like and control NK cells

Mass cytometry allows for high-throughput analysis of a large number of parameters on single cells, and it has been used to deeply immunophenotype and track the diversity of human NK cells (*21*, *22*). We developed custom mass cytometry panels that include NK cell lineage, maturation, receptor repertoire, and functional capacity (tables S1 and S2), and using the viSNE clustering and visualization strategy (*23*), we identified the differences between control and memory-like NK cells (Fig. 2, A and B, and figs. S2 and S3). Control and memory-like NK cells were localized within separate areas of the viSNE map, indicative of distinct cellular islands (Fig. 2A). We confirmed significant differences in the expression of a number of markers that were previously reported (*18*, *19*), including CD94 ($P = 0.002$),

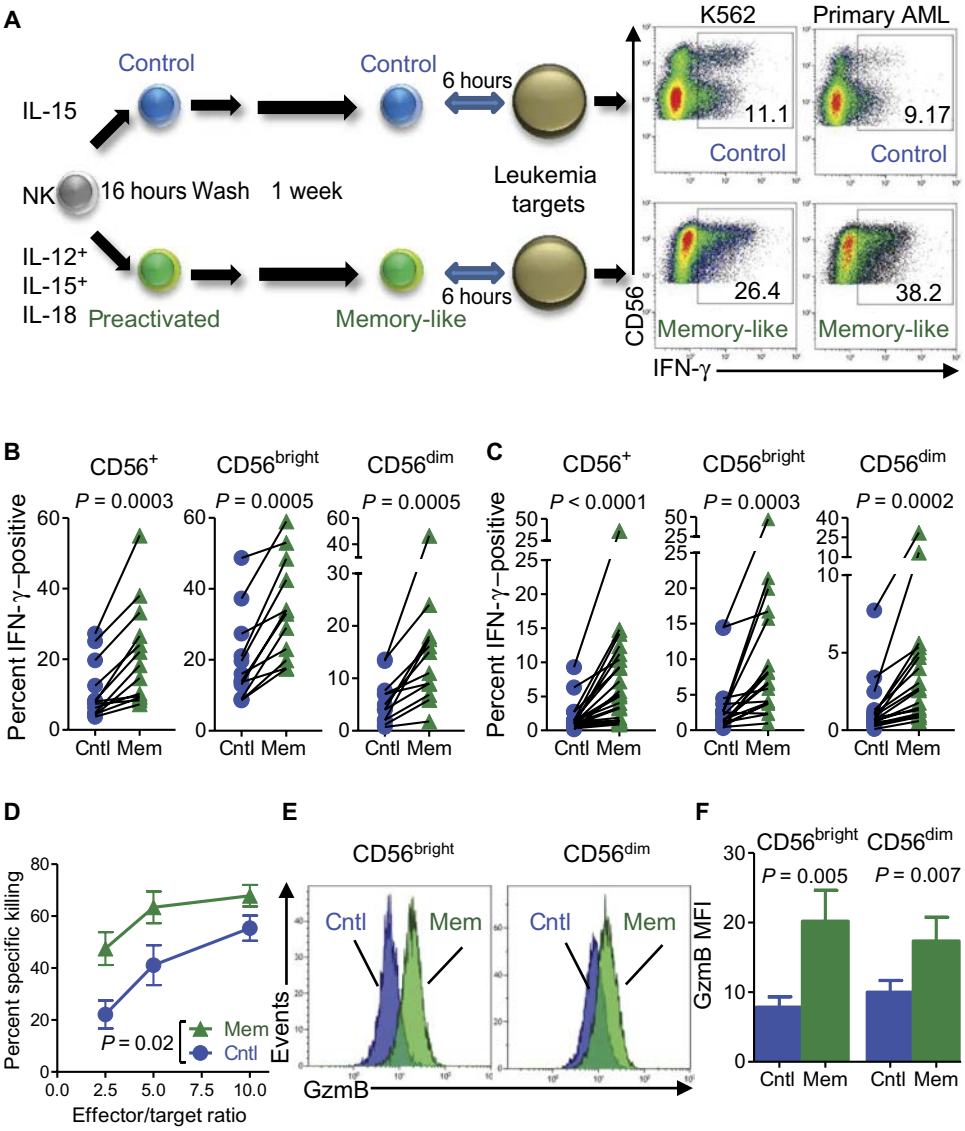

Fig. 1. Memory-like NK cells exhibit enhanced functional responses against leukemia targets. Purified NK cells were preactivated with IL-12, IL-15, and IL-18 or control (cntl; IL-15) for 16 hours, washed, and then rested in low concentrations of IL-15 to allow for differentiation. (**A**) Schema of memory-like (mem) NK cell in vitro experiments and representative flow plots showing enhanced IFN-γ production by NK cells after K562 (left) and primary AML (right) triggering. Inset numbers are the percentages of IFN-γ–positive NK cells within the indicated regions. (**B** and **C**) Summary of data showing enhanced IFN-γ production by all memory-like NK cells ($CD56^+$) as well as each of the two major human NK cell subsets ($CD56^{dim}$ and $CD56^{bright}$) restimulated with K562 (B) or primary allogeneic AML blasts (C). (**D**) Increased killing of K562 leukemia target cells by purified memory-like NK cells as compared to control NK cells from the same individuals. (**E**) Representative flow cytometry data showing increased granzyme B (GzmB) protein in memory-like compared to in control NK cells. (**F**) Summary of data from (E) showing granzyme B median fluorescence intensity (MFI). Data represent two to six independent experiments and were compared using Wilcoxon signed-rank test with means ± SEM displayed in all graphs.

NKG2A ($P = 0.004$), NKp46 ($P = 0.04$), and CD25 ($P = 0.03$) on the viSNE gated control and memory-like populations. Leveraging mass cytometry's expanded view of NK cell proteins, we observed increases in NKp30, NKp44, CD62L, CD27, and TRAIL and in the cytotoxic molecules perforin and granzyme B and also decreases in NKp80, compared to controls (Fig. 2B and fig. S3). Thus, memory-like and control NK cells were identifiable as distinct populations when tracked with high NK cell marker dimensionality by mass cytometry. In addition, mass cytometry confirmed flow cytometry

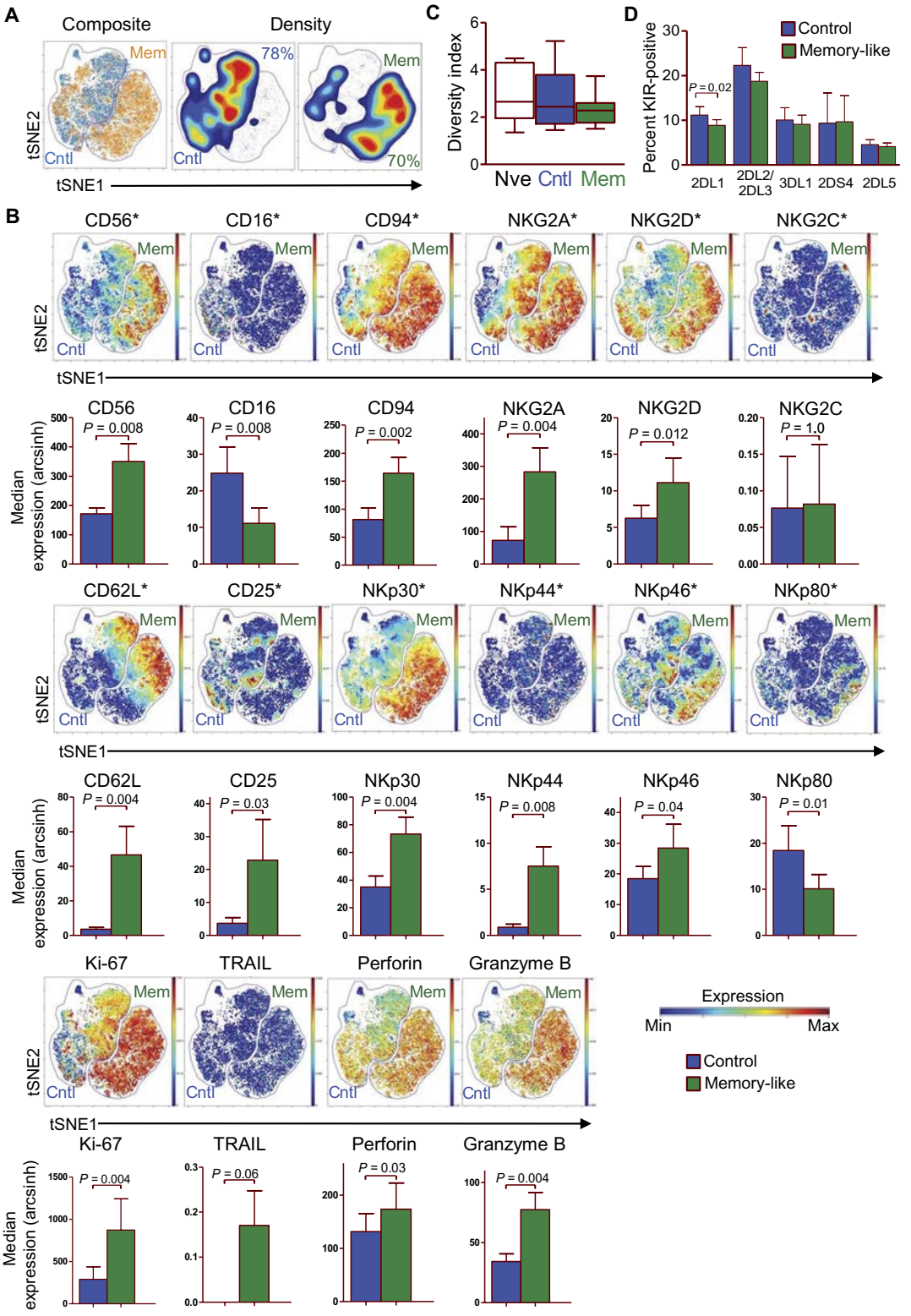

Fig. 2. Multidimensional analyses define the differences between memory-like and control NK cells. NK cells were assessed at baseline or after in vitro control and memory-like differentiation at day 7 (Fig. 1A) for the expression of 36 markers using mass cytometry. (**A** and **B**) Comparison of control and memory-like NK cells from a representative healthy individual using viSNE, clustered on 21 NK cell phenotypic markers. (A) Memory-like (orange) and control NK cell (blue) events overlaid in the tSNE1/tSNE2 fields (left) show their differential localization within the viSNE map. Density plots of control and memory-like NK cells in the tSNE1/tSNE2 fields (right). Inset values indicate the frequency of cells that fall within the control or memory-like gate. (B) The composite of the control and memory-like populations from (A), displaying the median expression of the indicated markers. Data are representative of nine individuals. Color scale indicates the intensity of expression of each marker signal. Minimum (min) and maximum (max) correspond to the 2nd and the 98th percentile values for each indicated marker, respectively. For additional summary data and statistical comparisons, see fig. S3. (**C**) Inhibitory KIR receptor inverse Simpson diversity index of baseline [naïve (nve)], control, and memory-like NK cells from nine individuals; box with whiskers displaying minimum to maximum. (**D**) Summary of data showing the percent positive of each indicated KIR for control and memory-like NK cells. All summary graphs display means ± SEM, unless otherwise indicated. Comparisons were made using Wilcoxon signed-rank test.

findings of increased cytotoxic effector proteins, which likely contribute to the enhanced cytotoxicity of memory-like NK cells against leukemia targets.

Memory-like NK cells respond to AML regardless of inhibitory KIR to KIR-ligand interactions

Because allogeneic NK cell responses to AML blasts are influenced by the interaction of the inhibitory killer cell immunoglobulin-like receptors (KIRs) with their cognate human leukocyte antigen (HLA) ligands (*24*–*26*), we next examined whether memory-like differentiation altered KIR diversity. We used mass cytometry to examine NK cells at baseline (naïve) and after control or memory-like differentiation in vitro at day 7 (table S1 and Fig. 1A). The inverse Simpson diversity index of KIR expressed by naïve, control (day 7), and memory-like (day 7) NK cells was unaltered (Fig. 2C) (*21*, *27*), demonstrating that inhibitory KIR phenotypes present at baseline were stable in vitro. Consistent with this, the percent of KIR-positive NK cells was similar at day 7 between control and memory-like NK cell populations (Fig. 2D).

In the setting of allogeneic HCT, donor KIR repertoire affects patient prognosis, highlighting the importance of the KIR to KIR-ligand mismatch for conventional NK cell anti-AML activity (*24*–*26*, *28*). To experimentally identify NK cell subsets that preferentially respond to primary AML blasts, we restimulated control and memory-like NK cells for 6 hours with primary AML blasts and assessed the expression of 36 parameters via mass cytometry (tables S2 to S4). Memory-like NK cells again produced more IFN-γ when triggered with primary AML blasts compared to controls (Fig. 3, A and B). We used spanning-tree progression analysis of density-normalized events (SPADE) to cluster the NK cells according to the expression of core NK cell markers and assessed each node (representing a distinct NK cell specificity) for IFN-γ expression (Fig. 3C) (*29*, *30*). The KIR-ligand interaction status of each node was defined to investigate their impact on memory-like and control NK cell responses. For a representative individual, we assigned the SPADE nodes as matched if they expressed KIR2DL2/KIR2DL3, which recognizes HLA-C1 present on the AML blasts. KIR2DL1 and KIR3DL1 did not have ligands present, and nodes that lacked KIR2DL2/KIR2DL3 were categorized as mismatched. Based on this approach, we observed the expected increased response in KIR-mismatched versus KIR-matched node in IFN-γ production in the control cells when triggered with AML blasts (Fig. 3, D to F). However, memory-like NK cells produced increased IFN-γ compared to control cells in both the KIR-ligand–matched and KIR-ligand–mismatched situations. Moreover, the IFN-γ production by memory-like NK cells was similar in the KIR-matched and KIR-mismatched setting (Fig. 3, D and E), which was reproducible across the seven individuals tested (Fig. 3E). Furthermore, when we expanded our analysis to four different primary AML blasts, we observed a consistent increase in IFN-γ production in KIR-matched memory-like NK cells compared to KIR-mismatched control-treated cells (Fig. 3F). Because most memory-like NK cells express NKG2A, we assessed IFN-γ production by $NKG2A^-$ or $NKG2A^+$ KIR-ligand–matched or KIR-ligand–mismatched NK cells and observed increased IFN-γ production by memory-like NK cells compared to controls in both subpopulations (figs. S4, A to C). Cell surface CD107a, tumor necrosis factor, and macrophage inflammatory protein-1α were also increased on memory-like NK cells in these assays, compared to controls (fig. S4D). Thus, memory-like differentiation enhances IFN-γ production in response to primary AML, regardless of whether memory-like NK cells expressed inhibitory KIR with a ligand present on the target AML blast.

Memory-like NK cells exhibit potent antileukemia functionality after transfer into NSG mice

To assess whether human memory-like NK cells maintain memory-like function in vivo, we used an adoptive transfer model with NSG mice (Fig. 4A). After 7 days, memory-like NK cells were found to localize in key hematopoietic tissues, including bone marrow (BM), spleen, and blood (Fig. 4B), and were found in similar numbers compared to control NK cells (Fig. 4C). The expression of selected chemokine receptors was minimally changed after IL-12, IL-15, and IL-18 pre-activation, with the exception of reduced expression of CX3CR1 (fig. S7). Memory-like NK cells also maintained their enhanced functionality as evidenced by increased IFN-γ production in response to ex vivo restimulation with K562 leukemia cells after 7 days in NSG mice (Fig. 4, D and E).

To test the ability of human memory-like NK cells to control leukemia in vivo, we engrafted K562-luc (luciferase-expressing) leukemia cells in NSG mice and adoptively transferred human IL-12, IL-15, and IL-18–preactivated or control NK cells into groups of NSG mice on day 4 (Fig. 4F). Memory-like NK cells were significantly more effective in controlling K562 tumor cell growth in vivo using whole-body bioluminescence imaging (BLI) ($P < 0.001$; Fig. 4, G and H). The enhanced leukemia control afforded by a single injection of human memory-like NK cells also resulted in improved survival of these mice (Fig. 4I).

Donor memory-like NK cells proliferate and expand after adoptive transfer into patients with AML

On the basis of these preclinical findings with human memory-like NK cells and those from mouse models evaluating NK cell–sensitive tumor cell line challenge (*17*), we initiated a first-in-human phase 1 clinical trial of allogeneic, HLA-haploidentical, IL-12, IL-15, and IL-18–preactivated NK cells in patients with rel/ref AML (fig. S5). Here, we report memory-like NK cell biology and antileukemia activity within the first nine evaluable patients treated at three different dose levels (Table 1). Donor NK cells were purified by CD3 depletion followed by CD56-positive selection (*10*), preactivated for 12 to 16 hours with rhIL-12, rhIL-15, and rhIL-18 in a good manufacturing practice (GMP) laboratory, washed, and infused into AML patients who were preconditioned with fludarabine/cyclophosphamide (*9*) on day 0. After adoptive transfer, low-dose rhIL-2 was administered to support memory-like NK cells through their induced high-affinity IL-2Rαβγ (*19*).

Three patients at dose level 1 (0.5×10^6/kg), three patients at dose level 2 (1.0×10^6/kg), and three patients at dose level 3 (all NK cells generated, capped at 10×10^6/kg) were evaluable. Donor memory-like NK cells were tracked in the blood of all patients with informative HLA [using donor- or patient-specific anti-HLA monoclonal antibodies (mAbs)], peaked in frequency at 7 to 14 days after infusion and, as expected (*9*), decreased in number after recipient T cell recovery (Fig. 5, A to C). Memory-like NK cells comprised >90% of blood NK cells at day 7 (Fig. 5, A and B), with an average of 419 ± 166–fold increase (range, 39 to 1270) comparing day 1 and day 7 counts (Fig. 5C). Donor memory-like NK cells had increased proliferation ($Ki\text{-}67^+$) at days 3 and 7 (Fig. 5, D and E). Similarly, assessments of the BM at day 8 after infusion revealed large percentages and absolute numbers of donor memory-like NK cells (Fig. 5, F to H), although there was heterogeneity between donor and recipient pairs, especially between NK cell dose levels (fig. S6).

Donor memory-like NK cells exhibit enhanced functionality after adoptive transfer into patients with AML

We next assessed donor and recipient blood NK cell IFN-γ production from these patients after a short-term ex vivo restimulation triggered by

K562 leukemia cells (Fig. 6, A to D). These analyses revealed an increased frequency of IFN-γ–positive donor, compared to recipient, NK cells (Fig. 6A). More strikingly, these experiments revealed that the absolute number of donor IFN-γ–producing NK cells was markedly increased, compared to the recipient NK cells in these samples (Fig. 6, B to D). Similarly, the number of IFN-γ–positive donor memory-like NK cells was greater than recipient NK cells in BM, although fewer patients had BM samples with adequate cell numbers for functional analyses (Fig. 6, E to G).

Complete remissions were observed after IL-12, IL-15, and IL-18–preactivated donor NK cell infusion in patients with rel/ref AML

Performing a phase 1 study of memory-like NK cell adoptive immunotherapy in older patients with active rel/ref AML is a clinical challenge, but it does permit investigation of anti-AML responses. Thirteen patients who had progressed after multiple previous treatments were administered with memory-like NK cells at dose levels 1, 2, and 3. Four

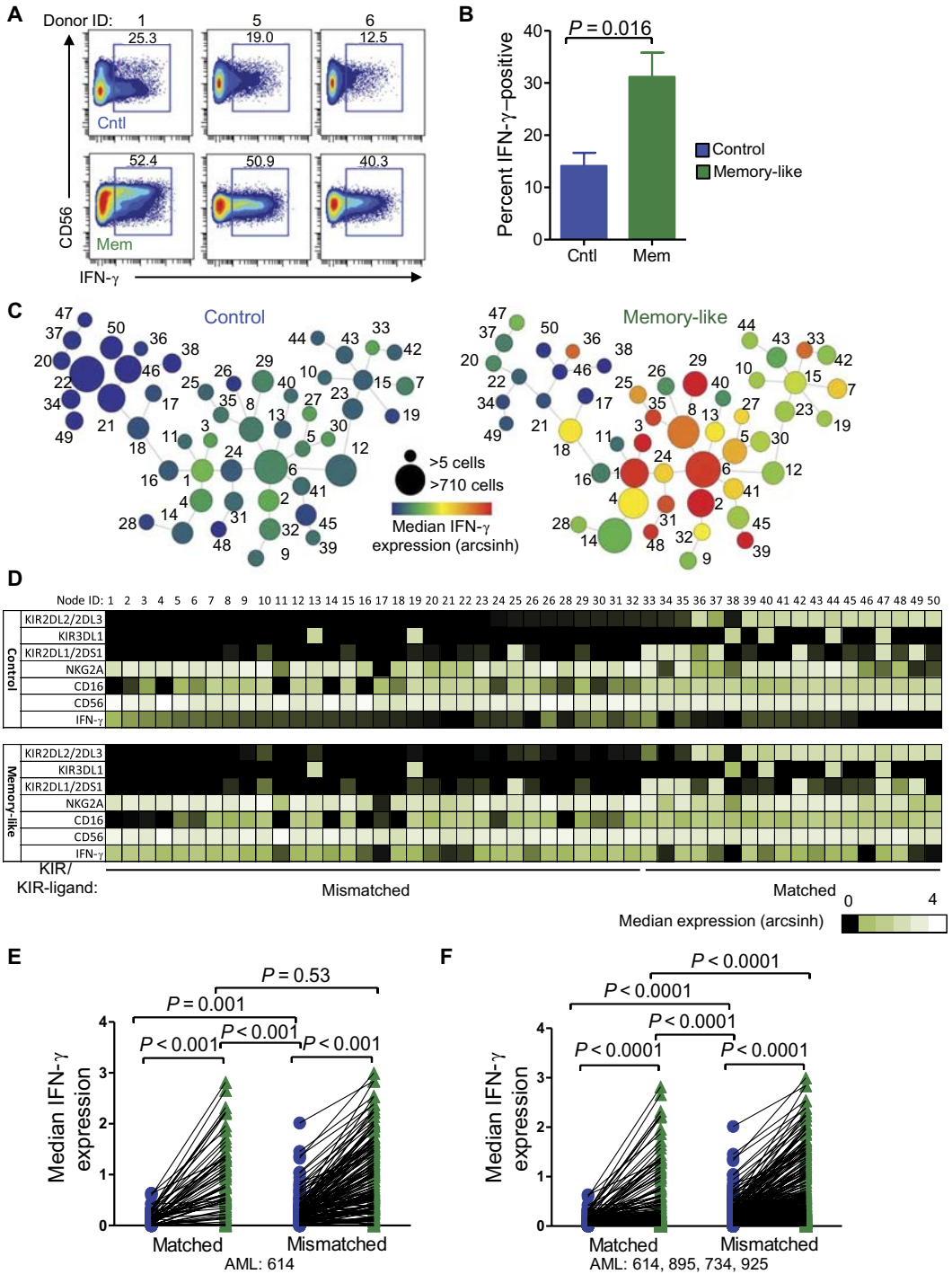

Fig. 3. Response of memory-like NK cells to primary AML blasts is enhanced regardless of KIR-ligand interactions. Control and memory-like NK cells were stimulated with primary AML blasts for 6 hours and assessed for the expression of 36 markers using mass cytometry. (**A**) Representative bivariate mass cytometry plots of IFN-γ production by control and memory-like NK cells stimulated at the bulk population level. Numbers depict percentages of cells within the indicated regions. (**B**) Summary of data (means ± SEM) from seven individuals showing percentages of IFN-γ–positive NK cells. (**C** to **E**) NK cells were further analyzed on 21 clustering parameters using SPADE. (C) Representative SPADE diagram of in vitro–differentiated control and memory-like NK cells from a healthy individual. Node size depicts relative number of cells per node, and color indicates median IFN-γ expression for each node. Numbers next to each node represent the node ID. (D) Heat map of the nodes from (C). KIR to KIR-ligand matched and mismatched status was assigned on the basis of the presence or absence of KIR2DL2/KIR2DL3, which recognizes HLA-C1 expressed by the primary AML. (E) Summary of data from seven individuals analyzed as in (C). (**F**) Summary of data from four to seven different individuals stimulated with four different AML blasts showing reproducibility of these findings. Control and memory-like data were compared using the Wilcoxon signed-rank test. Matched and mismatched data were compared using the Mann-Whitney test.

patients were not evaluable because of inadequate donor cell collection caused by apheresis technical failure ($n = 1$) or death resulting from bacteremia with septic shock before day 14 ($n = 1$) or before day 35 ($n = 2$). Of the nine evaluable patients (Table 1), there were four CR/CRi and one MLFS by the IWG response criteria (*31*), yielding an overall response rate of 55% and a CR/CRi rate of 45%. The changes in leukemia

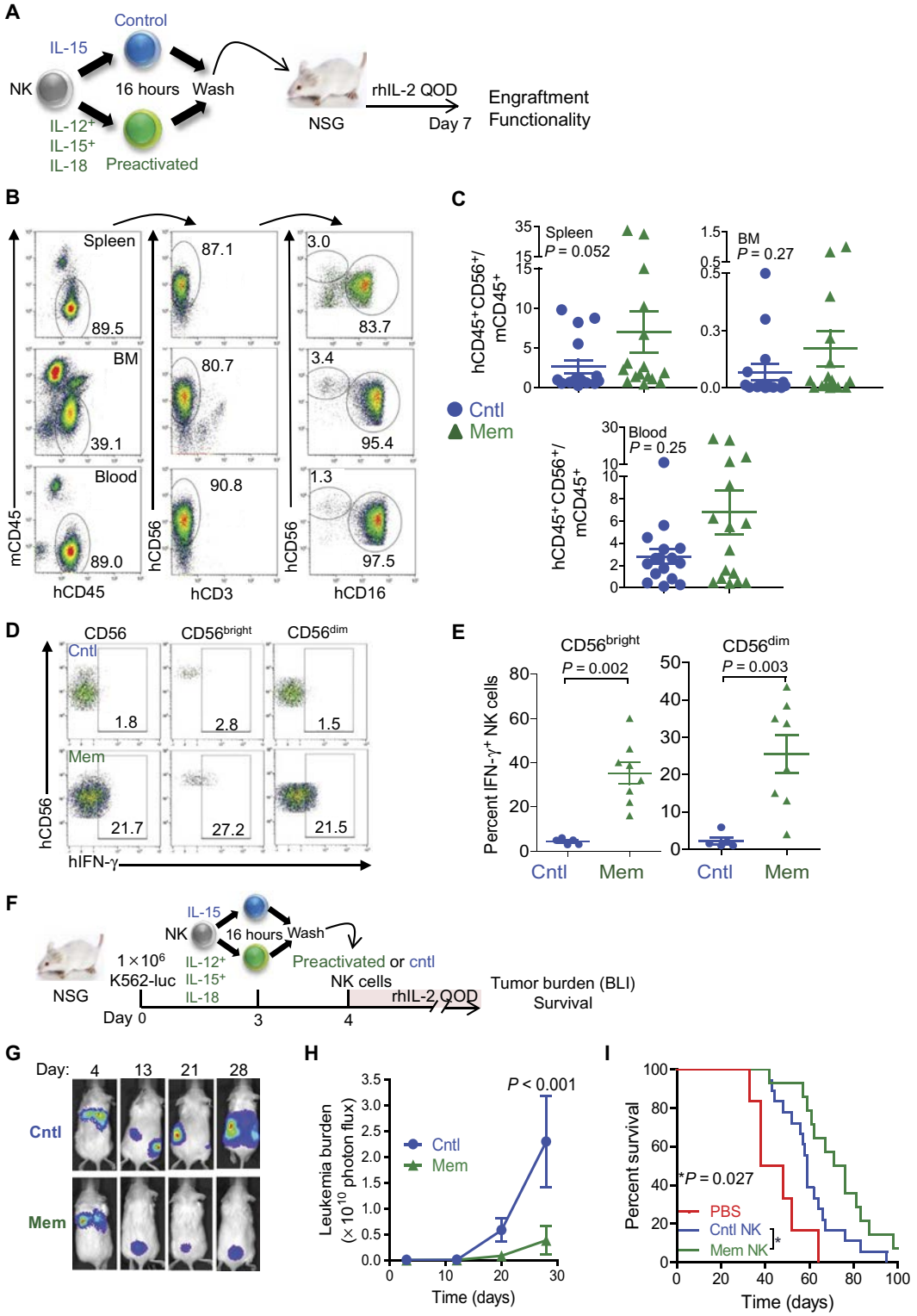

Fig. 4. Human memory-like NK cells control human leukemia in an NSG xenograft model. (**A**) Experimental design for (B) to (E). rhIL-2, recombinant human IL-2; QOD, every other day. (**B** to **E**) NSG mice received human NK cell adoptive transfers as indicated in (A). Representative flow cytometry at day 7 after transfer shows engraftment of human memory-like NK cells in the indicated tissues from a representative donor. Both $CD56^{bright}$ and $CD56^{dim}$ subsets are detectable. (C) Summary of data from (B) demonstrating the engraftment of control and memory-like NK cells, with abundance identified as the ratio to murine $CD45^{+}$ mononuclear cells. (D) Control or memory-like NK cells were administered to NSG mice as in (A). After 7 days, splenocytes were isolated and restimulated with K562 for 6 hours, followed by assessment of human NK cells for IFN-γ production. Numbers depict the percentages of cells within the indicated regions. (E) Summary of data from (D) showing the means ± SD of percent IFN-γ–positive NK cells from the indicated NK cell subsets. Statistical analysis was performed with Mann-Whitney test. (**F**) Experimental design for (G) to (I). (**G** to **I**) K562-luc was injected intravenously into NSG mice. After 4 days, BLI was performed to ensure leukemia engraftment, and control or memory-like NK cells were administered to the mice. The mice were treated with rhIL-2 every other day and monitored for tumor burden (BLI) and survival. (G) Representative BLI of recipient mice engrafted with K562-luc on the indicated day after tumor administration. (H) Summary of serial BLI measurements that show reduced tumor burden in mice receiving memory-like NK cells compared to control NK cells. Differences were determined using analysis of variance (ANOVA). (I) Mice were treated as in (F), monitored for survival, and analyzed using the log-rank test. PBS, phosphate-buffered saline. Summary of data are from two to three experiments with $n = 12$ to 24 mice per group represented as means ± SEM.

blast percentages in the BM of responding and nonresponding patients are shown in fig. S6. There was no detectable correlation between pretherapy BM blast percentage, donor KIR haplotype, the presence of predicted KIR-ligand mismatch, and the frequency of donor NK cells in the blood or BM and clinical response, but the number of patients was small. A complete set of clinical vignettes describing each patient and his or her clinical course is included in the Supplementary Materials and Methods. Additional parameters of relevant NK cell receptor biology are shown in table S5. Thus, allogeneic human IL-12, IL-15, and IL-18–induced memory-like NK cells proliferate, expand, and exhibit antileukemia function after adoptive transfer into rel/ref AML patients with active disease.

DISCUSSION

Motivated by the need to develop innovative treatment options for AML patients (*4*, *5*), we investigated the ability of a recently defined functional class of NK cells, cytokine-induced memory-like NK cells, to mediate antileukemia responses (*20*). Here, we demonstrated that primary human NK cells, differentiated in vitro into memory-like NK cells via brief preactivation with IL-12, IL-15, and IL-18, exhibit potent antileukemia responses in the form of IFN-γ production and cytotoxicity. Using mass cytometry and multidimensional analyses to assess a large number of NK cell relevant proteins simultaneously, we found that memory-like NK cells were clearly distinguishable from control NK cells from the same individual. Despite stable inhibitory KIR receptor expression, memory-like NK cells responded more robustly to primary AML blasts, regardless of KIR-ligand interactions. Moreover, human memory-like NK cells were superior, in terms of both controlling leukemia burden and prolonging survival, in an in vivo NSG xenograft model. Translating this to the clinic, we examined the biology of the MHC-haploidentical donor IL-12, IL-15, and IL-18–preactivated NK cells administered to patients with active rel/ref AML in the context of a first-in-human NK cell trial. After transfer, memory-like NK cells were detectable in the blood and BM of patients for weeks, proliferated extensively, and expanded in vivo. Further, memory-like NK cells that differentiated in patients in vivo exhibited enhanced functionality against leukemia target cells. Notably, five of the nine evaluable AML patients receiving IL-12, IL-15, and IL-18–preactivated NK cells had clinical responses, suggesting preliminary evidence of in vivo antileukemia activity. Thus, preactivation of NK cells with IL-12, IL-15, and IL-18 that results in memory-like NK cell differentiation represents a promising approach to enhancing adoptive allogeneic NK cell therapy.

Published studies have identified comparable IL-12, IL-15, and IL-18–induced memory-like NK cell biology in mice and humans (*15*–*19*). In mouse models, preactivation with IL-12, IL-15, and IL-18 has been shown to improve NK cell responses to lymphoma and melanoma cell lines in vivo, which required T cell–derived IL-2 (*17*). Although some phenotypic differences have been identified (*18*), a clear approach to distinguishing memory-like from conventional NK cells from the same donor was lacking. Through mass cytometry and multidimensional data reduction algorithms, control and memory-like NK cells were identified in separate areas of viSNE maps, indicating a distinct phenotype and providing an approach to tracking memory-like NK cells in vivo. Currently, memory-like NK cells that emerge after IL-12, IL-15, and IL-18 preactivation are thought to result from a differentiation process that yields a long-term alteration of functional capacity; however, the molecular mechanisms that control this process are yet to be defined. This concept of differentiation is consistent with the distinct phenotype tracked by multidimensional analyses, and the observations that enhanced memory-like NK cell responses to restimulation are retained after extensive cell division and persisted for weeks to months after the initial preactivation (*15*, *18*). The phenotypic changes observed after IL-12, IL-15, and IL-18 preactivation include increased expression of inhibitory, activating, and cytokine receptors (CD94/NKG2A, NKp30, NKp44, NKp46, NKG2D, CD62L, and CD25), whereas other receptors appear unchanged (KIR, CD57, NKG2C, DNAM-1, CD137, and CD11b) or decreased (NKp80). Such dynamic changes in activating, inhibitory, cytokine, and adhesion receptors are also consistent with differentiation. Further, prolonged IL-12, IL-15, and IL-18 activation (for 5 days) resulted in reduced methylation of the IFN-γ conserved

Table 1. Summary of clinical characteristics of evaluable patients treated with cytokine-induced memory-like NK cells. All patients were Caucasian. KIR-ligand mismatch is reported in the NK cell donor versus patient vector. Patient 012 was reenrolled at a higher dose level as patient 019. UPN, universal patient number; WHO, World Health Organization; DLT, dose-limiting toxicity; M, male; F, female; IWG, International Working Group; TF-PD, treatment failure due to progressive disease; CR, complete remission; MLFS, morphologic leukemia-free state; CRi, CR with incomplete blood count recovery; MDS, myelodysplastic syndrome.

UPN	Dose level	Gender	Age (years)	WHO diagnosis	Number of previous therapies	Pretreatment BM blast (%)	KIR-ligand mismatch	IWG response	DLT	GVHD
001	1	M	73	M2	2	16	Yes	TF-PD	No	No
006	1	M	70	M0	3	28	Yes	TF-PD	No	No
007	1	M	77	M0	1	47	Yes	CR	No	No
008	2	M	76	t-AML	3	17	Yes	TF-PD	No	No
009	2	F	73	M1	3	80	No	MLFS	No	No
012	2	F	71	M5	3	15	Yes	CR	No	No
017	3	M	64	t-AML	3	69	Yes	TF-PD	No	No
019	3	F	71	M5	4	15	Yes	CR	No	No
020	3	M	60	MDS-AML	1	13	Yes	CRi	No	No

noncoding sequence 1 locus in human NK cells, indicating that cytokines can affect epigenetic control mechanisms (*32*). One alternative hypothesis to the differentiation theory is that IL-12, IL-15, and IL-18–preactivated NK cells exist at an enhanced activation state without a fundamental change in their molecular programs. Although most published data are consistent with the idea of differentiation rather than

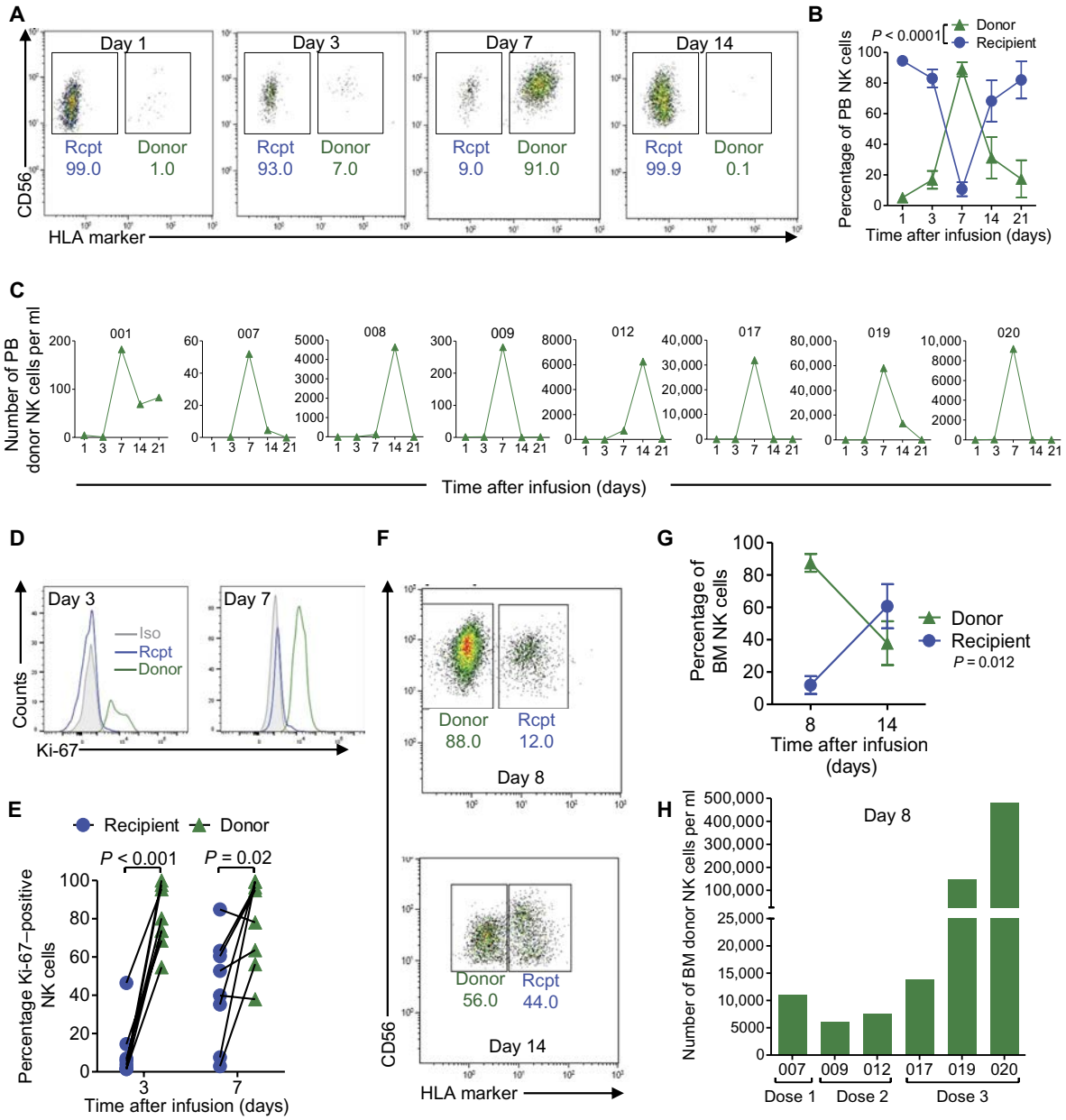

Fig. 5. Donor memory-like NK cells expand and proliferate in vivo in AML patients. (**A**) Representative flow cytometry data of donor (HLA$^+$) versus recipient (rcpt) (HLA$^-$) NK cells on the indicated day after infusion. (**B**) Percentages of the peripheral blood (PB) NK cell compartment composed of donor versus recipient NK cells at the indicated time points after infusion, summarizing the eight patients with informative HLA mAbs available for all time points. (**C**) Absolute numbers of donor NK cells per milliliter of peripheral blood at the indicated times after infusion for each patient (UPN above individual graphs). Absolute numbers were calculated by multiplying the number of mononuclear cells obtained per milliliter of blood by the fraction of CD45$^+$ cells that consisted of donor NK cells. (**D**) Representative flow cytometry data showing Ki-67 staining in donor and recipient NK cells from the peripheral blood on the indicated day after infusion. Isotype control (iso) staining for Ki-67 is indicated by the gray histogram. (**E**) Summary of data of the percentages of Ki-67–positive donor versus recipient peripheral blood NK cells at days 3 and 7 after infusion. (**F**) Representative flow cytometry data of donor (HLA$^-$) versus recipient (HLA$^+$) NK cells on the indicated day after infusion. (**G**) Percentages of the BM NK cell compartment that were donor versus recipient NK cells at the indicated time point after infusion, summarizing the seven patients with informative HLA mAbs available for all time points. (**H**) Absolute numbers of donor and recipient NK cells per milliliter of BM at day 8 after infusion. Absolute numbers were obtained as in (C). Statistical comparison was performed by two-way ANOVA. In representative bivariate flow plots (A and F), numbers indicate the frequency of cells within the indicated gate.

activation, elucidation of molecular mechanisms controlling cytokine-induced memory would provide additional clarification of this issue.

Earlier work has set the stage for the use of allogeneic NK cells as adoptive immunotherapy for AML patients (*9*–*12*), harnessing the leukemia-targeting potential of NK cell allorecognition of MHC-mismatched AML first identified after HCT (*8*). Initial pioneering adoptive NK cell therapy clinical trials identified that an available lymphoid niche was essential for donor NK cell engraftment and expansion; however, clinical responses occurred in a minority of patients with limited duration (*9*). This modest effect is consistent with the concept that combined modulatory approaches will be required to fully optimize NK cell adoptive immunotherapy for cancer patients, including (i) enhancement of NK cell targeting of cancer cells, (ii) augmentation of NK cell functional capacity, and (iii) elimination of inhibitory checkpoints or cellular negative regulators (33*S*). In the context of AML, NK cell allorecognition of MHC-haploidentical blasts has provided an established mode of targeting NK cells to myeloid leukemia via inhibitory receptor mismatch and activating receptor ligation. We discovered that IL-12, IL-15, and IL-18–induced memory-like NK cells exhibit enhanced triggering against AML regardless of KIR to KIR-ligand interactions, resulting in an expanded NK cell pool of AML-reactive effector cells. Because NKG2A is expressed on most memory-like NK cells, the interaction with HLA-E on AML blasts or bystander cells in the microenvironment remains a potentially important inhibitory pathway for memory-like NK cells. The functionality of memory-like NK cells is also enhanced in terms of cytotoxicity and IFN-γ production. Thus, through brief combined cytokine stimulation, two aspects of the NK cell antitumor response have been improved.

Most adoptive NK cell therapy studies to date use IL-2 or IL-15 to activate NK cells overnight before transfer. This strategy results in a short-term priming signal that increases NK cell functional capacity (*33*), but the effect is rapidly lost after removal from the in vitro cytokine milieu and transfer into the patient. Here, we reasoned that the longer-lasting increase in functional capacity afforded by memory-like NK cell differentiation, combined with improved AML recognition, would enhance in vivo expansion and antileukemia responses, resulting in a several week "window of opportunity" to attack AML blasts. Donor memory-like NK cells consistently expanded to become >90% of blood NK cells, as well as most BM NK cells. Because of concerns for cytokine-release syndrome, our phase 1 study was intentionally initiated with a starting NK cell dose of $^{1}/_{10}$ to $^{1}/_{20}$ of the typical adoptive NK cell dose (*9*–*12*). Considering the relatively low doses of highly purified IL-12, IL-15, and IL-18–preactivated NK cells administered to patients, the donor NK cell frequencies and numbers observed here in the blood and BM are remarkable. Two published studies have transferred doses of $CD56^{+}CD3^{-}$-purified NK cells similar to our dose level 3 as adoptive immunotherapy for patients with active AML (*11*, *12*). The overall response rate of 55% (5 of 9) and CR/CRi rate of 45% (4 of 9) in our study compare favorably to 7% (1 of 15) observed within cohort 2 of Bachanova *et al.* (0 of 10) (*12*) and patients with active AML on the work of Curti *et al.* (1 of 5) (*11*). Because our sample size was limited, this finding is hypothesis-generating and will need to be studied in more patients treated with IL-12, IL-15, and IL-18–preactivated NK cells. In our small sample set treated to date, these responses did not segregate with any KIR-based rules for NK cell allorecognition, although most patients studied had a KIR to KIR-ligand mismatch in the donor versus recipient direction.

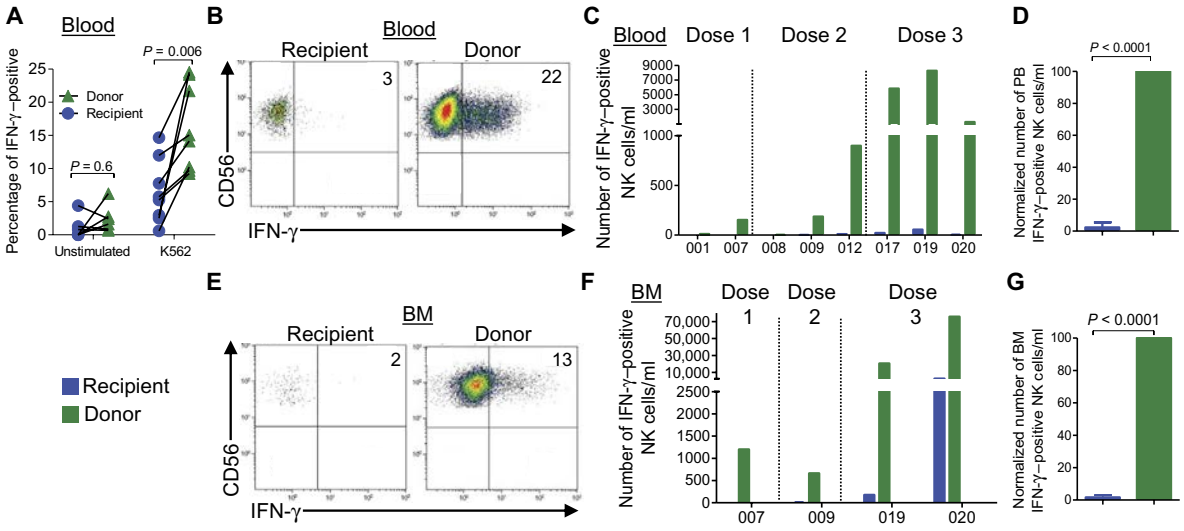

Fig. 6. Donor memory-like NK cells display enhanced antileukemia responses at 1 week after adoptive transfer. Freshly isolated peripheral blood mononuclear cells (PBMCs) from patient blood or BM were stimulated with K562 leukemia cells at an effector/target ratio of 10:1 for 6 hours and assessed for IFN-γ production by flow cytometry. (**A**) Percentage of IFN-γ–positive donor versus recipient NK cells in the peripheral blood for all patients. Data were compared using paired *t* test. (**B**) Representative flow cytometric data showing donor and recipient NK cell IFN-γ responses from the peripheral blood. (**C**) Absolute numbers of recipient (blue) and donor (green) NK cells producing IFN-γ in the blood. (**D**) Summary of data from (C) depicting relative IFN-γ production by recipient and donor NK cells from the blood; the data were normalized to donor IFN-γ–positive NK cells, which were set to 100%. (**E**) Representative flow cytometry data showing donor and recipient NK cell IFN-γ responses from the BM. (**F**) Absolute numbers of recipient and donor NK cells producing IFN-γ in the BM. (**G**) Summary of data from (F) depicting relative IFN-γ production by recipient and donor NK cells from the BM; the data were normalized to donor IFN-γ–positive NK cells, which were set to 100%. Normalized control NK cell responses were tested against 100% (donor) using a one-sample *t* test. Numbers represent percentage of cells within the indicated quadrant. All summary data depict means ± SEM.

Similarly, there were no associations with NK cell number or IFN-γ production measurements, which had substantial variability within patients who received different doses of NK cells. Thus, this report provides proof of concept that human IL-12, IL-15, and IL-18–preactivated NK cells may be translated into the cancer immunotherapy clinic, with consistent memory-like NK cell biology in vitro, in xenograft models in vivo and in AML patients in vivo.

MATERIALS AND METHODS

Study design

Patients treated on an open-label, nonrandomized, first-in-human phase 1 dose escalation trial (NCT01898793) are included in this study. The primary objective of the clinical trial was to identify the maximum tolerated or tested dose of memory-like NK cells administered to patients with rel/ref AML. Sample size was based on a standard 3 + 3 dose escalation design. Patients with rel/ref AML who were not candidates for immediate HCT were eligible to participate. Patients were treated with fludarabine/cyclophosphamide between days −7 and −2 for immunosuppression, followed on day 0 by allogeneic donor IL-12, IL-15, and IL-18–preactivated NK cells in escalating doses: 0.5×10^6/kg (dose level 1), 1.0×10^6/kg (dose level 2), and all NK cells that could be generated from a single leukapheresis capped at 10×10^6/kg (dose level 3). After donor NK cell adoptive transfer, patients received low-dose rhIL-2 (1×10^6 IU/m^2) subcutaneously every other day for a total of six doses. Donor NK cell products were generated by purifying NK cells from a nonmobilized leukapheresis product using CD3 depletion followed by CD56-positive selection on a CliniMACS device (>90% $CD56^+CD3^-$). Purified NK cells were preactivated with IL-12 (10 ng/ml), IL-15 (50 ng/ml), and IL-18 (50 ng/ml) for 12 to 16 hours under current GMP conditions. Samples were obtained from the peripheral blood (before treatment and at days 1, 3, 7, 8, 14, 21, 30, 60, and 100) and BM (before treatment and at days 8, 14, 30, 60, and 100) after the NK cell infusions. Clinical responses were defined by the revised IWG criteria for AML (*31*). If cell numbers were limiting, analyses of NK cell number and phenotype were prioritized. All patients provided informed consent before participating and were treated at the Washington University Institutional Review Board (IRB)–approved clinical trial (Human Research Protection Office #201401085).

Reagents, mice, and cell lines

Antihuman mAbs were used for flow and mass cytometry (tables S1, S2, and S6), including previously reported anti-HLA mAbs (*34*). Endotoxin-free, recombinant human cytokines are described in the Supplementary Materials and Methods. NOD.Cg-Prkdc^{scid} Il2rg^{tm1Wjl}/SzJ mice (4 to 8 weeks old) were obtained from The Jackson Laboratory, maintained under specific pathogen–free conditions, and used in accordance with our animal protocol approved by the Washington University Animal Studies Committee. K562 cells [American Type Culture Collection (ATCC), CCL-243] were obtained in 2008, viably cryopreserved and stored in liquid nitrogen, thawed for use in these studies, and maintained for <2 months at a time in continuous culture according to ATCC instructions. K562 cells were authenticated in 2015 using single-nucleotide polymorphism analysis and were found to be exactly matched to the K562 cells from the Japanese Collection of Research Bioresources, German Collection of Microorganisms and Cell Cultures (DSMZ), and ATCC databases (2015, Genetic Resources Core Facility at Johns Hopkins University).

NK cell purification and cell culture

Normal donor PBMCs were obtained from anonymous healthy platelet donors and isolated by Ficoll centrifugation (*18*, *19*, *35*). NK cells were purified using RosetteSep (STEMCELL Technologies; routinely ≥95% $CD56^+CD3^-$). KIR genotyping of donor PBMC was performed by Kashi Clinical Laboratories. Memory-like and control NK cells were generated as previously described (see the Supplementary Materials and Methods for more details) (*18*).

Patient samples

Patients with newly diagnosed AML provided informed consent under the Washington University IRB-approved protocol (2010-11766) and were the source of primary AML blasts for in vitro resimulation experiments (table S4). After informed consent, patient samples were also obtained from the first-in-human phase 1 clinical study of allogeneic donor memory-like NK cells in rel/ref AML (fig. S5). Patient peripheral blood or BM aspirate was obtained at the indicated time point after NK cell infusion, and PBMCs were isolated by Ficoll centrifugation and immediately used in experiments.

Functional assays to assess cytokine production

Control and memory-like NK cells were harvested after a rest period of 7 days to mimic transfer into a patient and to allow memory-like NK cell differentiation to occur. Cells were then restimulated in a standard functional assay (*18*, *19*, *35*). Cells were stimulated with K562 leukemia targets or freshly thawed primary AML blasts (effector/target ratio of 5:1, unless otherwise indicated). Further details are provided in the Supplementary Materials and Methods.

Flow-based killing assay

Flow-based killing assays were performed by co-incubating memory-like or control NK cells with carboxyfluorescein diacetate succinimidyl ester–labeled K562 cells for 4 hours and assaying 7-aminoactinomycin D uptake as described (*18*, *19*, *35*).

Adoptive transfer of human memory-like NK cells into NSG mice

Purified control (5×10^6; ≥95% $CD56^+CD3^-$) or IL-12, IL-15, and IL-18–preactivated NK cells were injected retro-orbitally into NSG mice. Mice received rhIL-2 (50,000 IU) through intraperitoneal injection every other day to support the adoptively transferred NK cells. After 7 days, the mice were sacrificed, and organs (spleen, blood, and BM) were assessed for the presence of transferred cells. NSG splenocytes were also examined for intracellular IFN-γ production after restimulation with K562 leukemia targets.

In vivo BLI

For BLI experiments, mice were treated as described in the Supplementary Materials and Methods. For imaging, mice were injected intraperitoneally with D-luciferin (150 μg/g) (Biosynth) in PBS and imaged using the IVIS 100 (Caliper). BLI was performed at the indicated time points.

Flow cytometric analysis

Cell staining was performed as described (*18*, *19*, *35*), and data were acquired on a Gallios flow cytometer (Beckman Coulter) and analyzed using Kaluza (Beckman Coulter) or FlowJo (Tree Star) software.

Mass cytometry

All mass cytometry data were collected on a CyTOF2 mass cytometer (Fluidigm) and analyzed using Cytobank (*36*). Mass cytometry data

were analyzed using previously described methods (*37*). For detailed information, refer to the Supplementary Materials and Methods. Diversity was assessed on eight individual donors at baseline (freshly thawed PBMCs or thawed pure NK cells), after control treatment or memory-like differentiation (described above) using the Boolean gating strategy described in fig. S2 (*21*, *22*). Event counts were used to generate inverse Simpson index for KIR2DL1, KIR2DL1/KIR2DL2, KIR3DL1, KIR2DS4, and KIR2DL5 expression.

Statistical analysis

Before statistical analyses, all data were tested for normal distribution (D'Agostino-Pearson omnibus normality test). If data were not normally distributed, the appropriate nonparametric tests were used (GraphPad Prism v5.0), with all statistical comparisons indicated in the figure legends. Uncertainty is represented in the figures as SEM, except as indicated in the figure legends. All comparisons used a two-sided α of 0.05 for significance testing.

SUPPLEMENTARY MATERIALS

www.sciencetranslationalmedicine.org/cgi/content/full/8/357/357ra123/DC1
Materials and Methods
Clinical vignettes
Fig. S1. Reduction of memory-like NK cell cytotoxicity against K562 leukemia cells by blockade of NKG2D or DNAM-1.
Fig. S2. Mass cytometry gating strategies.
Fig. S3. Phenotypic marker expression on viSNE gated control and memory-like NK cells.
Fig. S4. Enhanced effector responses of memory-like NK cells compared to control-treated NK cells.
Fig. S5. Schema of allogeneic memory-like NK cell phase 1 clinical trial (NCT01898793).
Fig. S6. Distribution of BM blast percentages and donor NK cell numbers sorted by clinical outcomes.
Fig. S7. Chemokine receptor expression on control versus IL-12, IL-15, and IL-18–preactivated human NK cells.
Table S1. NK cell phenotypic mass cytometry panel design, reagents, and clustering usage.
Table S2. NK cell functional mass cytometry panel design, reagents, and clustering usage.
Table S3. Characteristics of normal donors used in mass cytometry functional experiments.
Table S4. Characteristics of AML samples used for in vitro NK cell functional assays.
Table S5. Patient HLA and donor KIR characteristics for evaluable donor-patient pairs treated in the phase 1 clinical trial.
Table S6. Flow cytometry mAbs.
Reference (*38*)

REFERENCES AND NOTES

1. G. Juliusson, P. Antunovic, Å. Derolf, S. Lehmann, L. Möllgård, D. Stockelberg, U. Tidefelt, A. Wahlin, M. Höglund, Age and acute myeloid leukemia: Real world data on decision to treat and outcomes from the Swedish Acute Leukemia Registry. *Blood* **113**, 4179–4187 (2009).
2. E. Estey, H. Döhner, Acute myeloid leukaemia. *Lancet* **368**, 1894–1907 (2006).
3. J. M. Rowe, M. S. Tallman, How I treat acute myeloid leukemia. *Blood* **116**, 3147–3156 (2010).
4. H. Döhner, E. Estey, S. Amadori, F. R. Appelbaum, T. Büchner, A. K. Burnett, H. Dombret, P. Fenaux, D. Grimwade, R. A. Larson, F. Lo-Coco, T. Naoe, D. Niederwieser, G. J. Ossenkoppele, M. A. Sanz, J. Sierra, M. S. Tallman, B. Löwenberg, C. D. Bloomfield, Diagnosis and management of acute myeloid leukemia in adults: Recommendations from an international expert panel, on behalf of the European LeukemiaNet. *Blood* **115**, 453–474 (2010).
5. K. Mrózek, G. Marcucci, D. Nicolet, K. S. Maharry, H. Becker, S. P. Whitman, K. H. Metzeler, S. Schwind, Y.-Z. Wu, J. Kohlschmidt, M. J. Pettenati, N. A. Heerema, A. W. Block, S. R. Patil, M. R. Baer, J. E. Kolitz, J. O. Moore, A. J. Carroll, R. M. Stone, R. A. Larson, C. D. Bloomfield, Prognostic significance of the European LeukemiaNet standardized system for reporting cytogenetic and molecular alterations in adults with acute myeloid leukemia. *J. Clin. Oncol.* **30**, 4515–4523 (2012).
6. M. A. Caligiuri, Human natural killer cells. *Blood* **112**, 461–469 (2008).
7. J. Pahl, A. Cerwenka, Tricking the balance: NK cells in anti-cancer immunity. *Immunobiology* S0171-2985(15)30031-0 (2015).
8. L. Ruggeri, M. Capanni, E. Urbani, K. Perruccio, W. D. Shlomchik, A. Tosti, S. Posati, D. Rogaia, F. Frassoni, F. Aversa, M. F. Martelli, A. Velardi, Effectiveness of donor natural killer cell alloreactivity in mismatched hematopoietic transplants. *Science* **295**, 2097–2100 (2002).
9. J. S. Miller, Y. Soignier, A. Panoskaltsis-Mortari, S. A. McNearney, G. H. Yun, S. K. Fautsch, D. McKenna, C. Le, T. E. Defor, L. J. Burns, P. J. Orchard, B. R. Blazar, J. E. Wagner, A. Slungaard, D. J. Weisdorf, I. J. Okazaki, P. B. McGlave, Successful adoptive transfer and in vivo expansion of human haploidentical NK cells in patients with cancer. *Blood* **105**, 3051–3057 (2005).
10. J. E. Rubnitz, H. Inaba, R. C. Ribeiro, S. Pounds, B. Rooney, T. Bell, C.-H. Pui, W. Leung, NKAML: A pilot study to determine the safety and feasibility of haploidentical natural killer cell transplantation in childhood acute myeloid leukemia. *J. Clin. Oncol.* **28**, 955–959 (2010).
11. A. Curti, L. Ruggeri, A. D'Addio, A. Bontadini, E. Dan, M. R. Motta, S. Trabanelli, V. Giudice, E. Urbani, G. Martinelli, S. Paolini, F. Fruet, A. Isidori, S. Parisi, G. Bandini, M. Baccarani, A. Velardi, R. M. Lemoli, Successful transfer of alloreactive haploidentical KIR ligand-mismatched natural killer cells after infusion in elderly high-risk acute myeloid leukemia patients. *Blood* **118**, 3273–3279 (2011).
12. V. Bachanova, S. Cooley, T. E. Defor, M. R. Verneris, B. Zhang, D. H. McKenna, J. Curtsinger, A. Panoskaltsis-Mortari, D. Lewis, K. Hippen, P. McGlave, D. J. Weisdorf, B. R. Blazar, J. S. Miller, Clearance of acute myeloid leukemia by haploidentical natural killer cells is improved using IL-2 diphtheria toxin fusion protein. *Blood* **123**, 3855–3863 (2014).
13. G. Min-Oo, Y. Kamimura, D. W. Hendricks, T. Nabekura, L. L. Lanier, Natural killer cells: Walking three paths down memory lane. *Trends Immunol.* **34**, 251–258 (2013).
14. A. Rölle, J. Pollmann, A. Cerwenka, Memory of infections: An emerging role for natural killer cells. *PLOS Pathog.* **9**, e1003548 (2013).
15. M. A. Cooper, J. M. Elliott, P. A. Keyel, L. Yang, J. A. Carrero, W. M. Yokoyama, Cytokine-induced memory-like natural killer cells. *Proc. Natl. Acad. Sci. U.S.A.* **106**, 1915–1919 (2009).
16. M. P. Keppel, L. Yang, M. A. Cooper, Murine NK cell intrinsic cytokine-induced memory-like responses are maintained following homeostatic proliferation. *J. Immunol.* **190**, 4754–4762 (2013).
17. J. Ni, M. Miller, A. Stojanovic, N. Garbi, A. Cerwenka, Sustained effector function of IL-12/15/18–preactivated NK cells against established tumors. *J. Exp. Med.* **209**, 2351–2365 (2012).
18. R. Romee, S. E. Schneider, J. W. Leong, J. M. Chase, C. R. Keppel, R. P. Sullivan, M. A. Cooper, T. A. Fehniger, Cytokine activation induces human memory-like NK cells. *Blood* **120**, 4751–4760 (2012).
19. J. W. Leong, J. M. Chase, R. Romee, S. E. Schneider, R. P. Sullivan, M. A. Cooper, T. A. Fehniger, Preactivation with IL-12, IL-15, and IL-18 induces CD25 and a functional high-affinity IL-2 receptor on human cytokine-induced memory-like natural killer cells. *Biol. Blood Marrow Transplant.* **20**, 463–473 (2014).
20. M. M. Berrien-Elliott, J. A. Wagner, T. A. Fehniger, Human cytokine-induced memory-like natural killer cells. *J. Innate Immun.* **7**, 563–571 (2015).
21. A. Horowitz, D. M. Strauss-Albee, M. Leipold, J. Kubo, N. Nemat-Gorgani, O. C. Dogan, C. L. Dekker, S. Mackey, H. Maecker, G. E. Swan, M. M. Davis, P. J. Norman, L. A. Guethlein, M. Desai, P. Parham, C. A. Blish, Genetic and environmental determinants of human NK cell diversity revealed by mass cytometry. *Sci. Transl. Med.* **5**, 208ra145 (2013).
22. D. M. Strauss-Albee, J. Fukuyama, E. C. Liang, Y. Yao, J. A. Jarrell, A. L. Drake, J. Kinuthia, R. R. Montgomery, G. John-Stewart, S. Holmes, C. A. Blish, Human NK cell repertoire diversity reflects immune experience and correlates with viral susceptibility. *Sci. Transl. Med.* **7**, 297ra115 (2015).
23. E.-a. D. Amir, K. L. Davis, M. D. Tadmor, E. F. Simonds, J. H. Levine, S. C. Bendall, D. K. Shenfeld, S. Krishnaswamy, G. P. Nolan, D. Pe'er, viSNE enables visualization of high dimensional single-cell data and reveals phenotypic heterogeneity of leukemia. *Nat. Biotechnol.* **31**, 545–552 (2013).
24. S. Cooley, D. J. Weisdorf, L. A. Guethlein, J. P. Klein, T. Wang, C. T. Le, S. G. E. Marsh, D. Geraghty, S. Spellman, M. D. Haagenson, M. Ladner, E. Trachtenberg, P. Parham, J. S. Miller, Donor selection for natural killer cell receptor genes leads to superior survival after unrelated transplantation for acute myelogenous leukemia. *Blood* **116**, 2411–2419 (2010).
25. S. Cooley, E. Trachtenberg, T. L. Bergemann, K. Saeteurn, J. Klein, C. T. Le, S. G. E. Marsh, L. A. Guethlein, P. Parham, J. S. Miller, D. J. Weisdorf, Donors with group B KIR haplotypes improve relapse–free survival after unrelated hematopoietic cell transplantation for acute myelogenous leukemia. *Blood* **113**, 726–732 (2009).
26. J. M. Venstrom, G. Pittari, T. A. Gooley, J. H. Chewning, S. Spellman, M. Haagenson, M. M. Gallagher, M. Malkki, E. Petersdorf, B. Dupont, K. C. Hsu, *HLA-C*–dependent prevention of leukemia relapse by donor activating *KIR2DS1*. *N. Engl. J. Med.* **367**, 805–816 (2012).
27. D. M. Strauss-Albee, A. Horowitz, P. Parham, C. A. Blish, Coordinated regulation of NK receptor expression in the maturing human immune system. *J. Immunol.* **193**, 4871–4879 (2014).
28. L. L. Lanier, NK cell recognition. *Annu. Rev. Immunol.* **23**, 225–274 (2005).
29. S. C. Bendall, E. F. Simonds, P. Qiu, E.-a. D. Amir, P. O. Krutzik, R. Finck, R. V. Bruggner, R. Melamed, A. Trejo, O. I. Ornatsky, R. S. Balderas, S. K. Plevritis, K. Sachs, D. Pe'er, S. D. Tanner,

G. P. Nolan, Single-cell mass cytometry of differential immune and drug responses across a human hematopoietic continuum. *Science* **332**, 687–696 (2011).
30. P. Qiu, E. F. Simonds, S. C. Bendall, K. D. Gibbs Jr., R. V. Bruggner, M. D. Linderman, K. Sachs, G. P. Nolan, S. K. Plevritis, Extracting a cellular hierarchy from high-dimensional cytometry data with SPADE. *Nat. Biotechnol.* **29**, 886–891 (2011).
31. B. D. Cheson, J. M. Bennett, K. J. Kopecky, T. Büchner, C. L. Willman, E. H. Estey, C. A. Schiffer, H. Doehner, M. S. Tallman, T. A. Lister, F. Lo-Coco, R. Willemze, A. Biondi, W. Hiddemann, R. A. Larson, B. Löwenberg, M. A. Sanz, D. R. Head, R. Ohno, C. D. Bloomfield, Revised recommendations of the international working group for diagnosis, standardization of response criteria, treatment outcomes, and reporting standards for therapeutic trials in acute myeloid leukemia. *J. Clin. Oncol.* **21**, 4642–4649 (2003).
32. M. Luetke-Eversloh, Q. Hammer, P. Durek, K. Nordström, G. Gasparoni, M. Pink, A. Hamann, J. Walter, H.-D. Chang, J. Dong, C. Romagnani, Human cytomegalovirus drives epigenetic imprinting of the *IFNG* locus in NKG2C^{hi} natural killer cells. *PLOS Pathog.* **10**, e1004441 (2014).
33. R. Romee, J. W. Leong, T. A. Fehniger, Utilizing cytokines to function-enable human NK cells for the immunotherapy of cancer. *Scientifica* **2014**, 205796 (2014).
34. A. Mulder, M. J. Kardol, J. S. Arn, C. Eijsink, M. E. I. Franke, G. M. T. Schreuder, G. W. Haasnoot, I. I. N. Doxiadis, D. H. Sachs, D. M. Smith, F. H. J. Claas, Human monoclonal HLA antibodies reveal interspecies crossreactive swine MHC class I epitopes relevant for xenotransplantation. *Mol. Immunol.* **47**, 809–815 (2010).
35. M. Rosario, B. Liu, L. Kong, L. I. Collins, S. E. Schneider, X. Chen, K. Han, E. K. Jeng, P. R. Rhode, J. W. Leong, T. Schappe, B. A. Jewell, C. R. Keppel, K. Shah, B. Hess, R. Romee, D. R. Piwnica-Worms, A. F. Cashen, N. L. Bartlett, H. C. Wong, T. A. Fehniger, The IL-15-based ALT-803 complex enhances FcγRIIIa-triggered NK cell responses and in vivo clearance of B cell lymphomas. *Clin. Cancer Res.* **22**, 596–608 (2016).
36. N. Kotecha, P. O. Krutzik, J. M. Irish, Web-based analysis and publication of flow cytometry experiments. *Curr. Protoc. Cytom.* **Chapter 10**, Unit10.17 (2010).
37. K. E. Diggins, P. B. Ferrell Jr., J. M. Irish, Methods for discovery and characterization of cell subsets in high dimensional mass cytometry data. *Methods* **82**, 55–63 (2015).
38. E. R. Zunder, R. Finck, G. K. Behbehani, E.-a. D. Amir, S. Krishnaswamy, V. D. Gonzalez, C. G. Lorang, Z. Bjornson, M. H. Spitzer, B. Bodenmiller, W. J. Fantl, D. Pe'er, G. P. Nolan, Palladium-based mass tag cell barcoding with a doublet-filtering scheme and single-cell deconvolution algorithm. *Nat. Protoc.* **10**, 316–333 (2015).

Acknowledgments: We would like to thank W. Yokoyama, A. French, T. Ley, P. Westervelt, and J. DiPersio for insightful discussion. We thank C. Keppel, K. Shah, and A. Ireland for technical assistance. We also thank our patient volunteers and the BM transplant/leukemia physician and nurse coordinator teams at the Washington University School of Medicine (WUSM). **Funding:** This work was supported by the American Society of Hematology Foundation, the Conquer Cancer Foundation of the American Society of Clinical Oncology, the WUSM Siteman Cancer Center Developmental Research Award and Team Science Award, the WUSM Institute of Clinical and Translational Research Award, the Leukemia Specialized Program of Research Excellence (P50 CA171963) Development Research Award, the Howard Hughes Medical Institute Medical Fellow Award, the Translational TL1 program, NIH/National Cancer Institute (NCI) grant F32 CA200253, the V Foundation for Cancer Research, and the Gabrielle's Angel Foundation for Cancer Research. Technical support was provided by the Immunomonitoring Laboratory (also supported by the Center for Human Immunology and Immunotherapy Programs), the Biological Therapy Core, and the Small Animal Cancer Imaging Core (also supported by P50 CA94056), which are supported by the NCI Cancer Center Support grant P30CA91842. We acknowledge the use of the Protein Production and Purification Facility for CyTOF mAb conjugation (P30 AR048335). **Author contributions:** R.R., M.R., M.M.B.-E., S.T.O., M.A.C., and T.A.F. conceived and designed the study; R.R., M.R., M.M.B.-E., J.A.W., B.A.J., T.S., S.A.-L., S.E.S., S.W., L.Y., Y.-S.L., and C.C.N. collected, analyzed, and assembled the data; A.M. and F.C. provided critical reagents; R.R., M.R., M.M.B.-E., J.W.L., M.A.C., and T.A.F. wrote the manuscript; and all authors reviewed the data and edited and approved the final version of the manuscript. **Competing interests:** The authors declare that they have no competing interests.

Submitted 22 February 2016
Accepted 4 August 2016
Published 21 September 2016
10.1126/scitranslmed.aaf2341

Citation: R. Romee, M. Rosario, M. M. Berrien-Elliott, J. A. Wagner, B. A. Jewell, T. Schappe, J. W. Leong, S. Abdel-Latif, S. E. Schneider, S. Willey, C. C. Neal, L. Yu, S. T. Oh, Y.-S. Lee, A. Mulder, F. Claas, M. A. Cooper, T. A. Fehniger, Cytokine-induced memory-like natural killer cells exhibit enhanced responses against myeloid leukemia. *Sci. Transl. Med.* **8**, 357ra123 (2016).

HIV

Nonprogressing HIV-infected children share fundamental immunological features of nonpathogenic SIV infection

Maximilian Muenchhoff *et al.* (Philip Goulder)

Citation
Sci. Transl. Med. 28 Sep 2016: Vol. 8, Issue 358, 358ra125

10.1126/scitranslmed.aag1048

Disease-free infection in HIV-infected adults is associated with human leukocyte antigen–mediated suppression of viremia, whereas in the sooty mangabey and other healthy natural hosts of simian immunodeficiency virus (SIV), viral replication continues unabated. To better understand factors preventing HIV disease, we investigated pediatric infection, where AIDS typically develops more rapidly than in adults. Among 170 nonprogressing antiretroviral therapy–naïve children aged >5 years maintaining normal-for-age CD4 T cell counts, immune activation levels were low despite high viremia (median, 26,000 copies/ml). Potent, broadly neutralizing antibody responses in most of the subjects and strong virus-specific T cell activity were present but did not drive pediatric nonprogression. However, reduced CCR5 expression and low HIV infection in long-lived central memory CD4 T cells were observed in pediatric nonprogressors. These children therefore express two cardinal immunological features of nonpathogenic SIV infection in sooty mangabeys—low immune activation despite high viremia and low CCR5 expression on long-lived central memory CD4 T cells—suggesting closer similarities with nonpathogenetic mechanisms evolved over thousands of years in natural SIV hosts than those operating in HIV-infected adults.

AUTOIMMUNITY

A divergent population of autoantigen-responsive CD4+T cells in infants prior to β cell autoimmunity

Anne-Kristin Heninger *et al.* (Ezio Bonifacio)

Citation
Sci. Transl. Med. 22 Feb 2017: Vol. 9, Issue 378, eaaf8848

10.1126/scitranslmed.aaf8848

Autoimmune diabetes is marked by sensitization to β cell self-antigens in childhood. We longitudinally followed at-risk children from infancy and performed single-cell gene expression in β cell antigen–responsive $CD4^+$ T cells through pre- and established autoimmune phases. A striking divergence in the gene signature of β cell antigen–responsive naïve $CD4^+$ T cells from children who developed β cell autoimmunity was found in infancy, well before the appearance of β cell antigen–specific memory T cells or autoantibodies. The signature resembled a pre–T helper 1 (T_H1)/T_H17/T follicular helper cell response with expression of *CCR6*, *IL21*, *TBX21*, *TNF*, *RORC*, *EGR2*, *TGFB1*, and *ICOS*, in the absence of *FOXP3*, *IL17*, and other cytokines. The cells transitioned to an IFNG-T_H1 memory phenotype with the emergence of autoantibodies. We suggest that the divergent naïve T cell response is a consequence of genetic or environmental priming during unfavorable perinatal exposures and that the signature will guide future efforts to detect and prevent β cell autoimmunity.

Recombinant Proteins

FOR YOUR RESEARCH

- Specific and Potent Biological Activity
- In-house Manufactured
- Bioassay Tested
- Exceptional Pricing

View 600+ Functional Proteins:
biolegend.com/recombinant_proteins

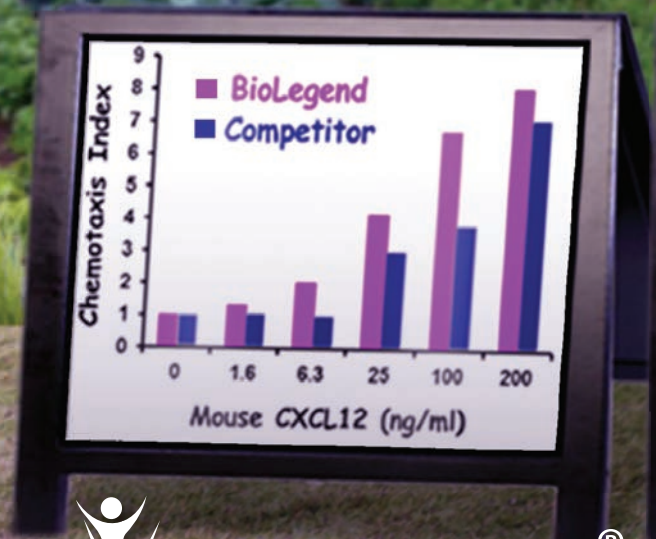

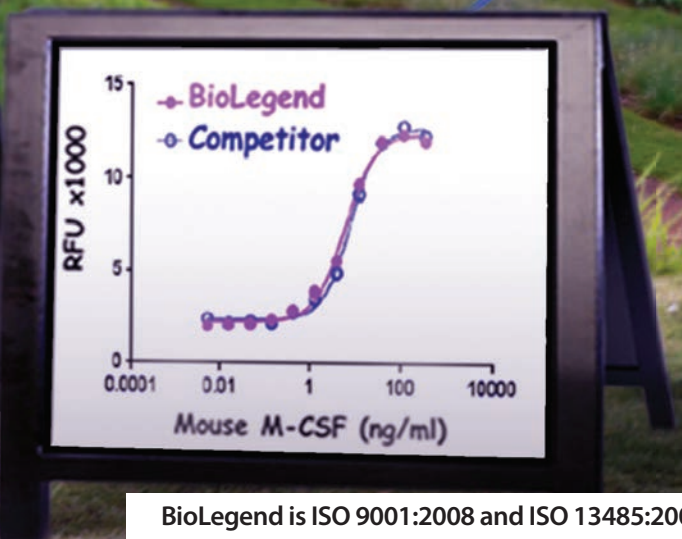

BioLegend®

BioLegend is ISO 9001:2008 and ISO 13485:2003 Certified

Toll-Free Tel: (US & Canada): 1.877.BIOLEGEND (246.5343)
Tel: 858.768.5800
biolegend.com
08-0065-01

World-Class Quality | Superior Customer Support | Outstanding Value